Semi Annual Report

(December 31 — June 30, 2002)

Contract Number NAS5—31363

OCEAN OBSERVATIONS WITH EOS/MODIS:

Algorithm Development and Post Launch Studies

Howard R. Gordon, PI
University of Miami
Department of Physics
Coral Gables, FL 33124

(Submitted July 15, 2002)

Preamble

This document describes our progress thus far toward completion of our research plans regarding two MODIS Ocean-related algorithms.

A. Retrieval of the Normalized Water-Leaving Radiance (Atmospheric Correction).
B. Retrieval of the Detached Coccolith/Calcite Concentration

In addition, , we break our effort into two broad components for each algorithm:

- Algorithm Improvement/Enhancement;
- Validation of MODIS Algorithms and Products.

These components will overlap in some instances.

RETREIVAL OF NORMALIZED WATER-LEAVING RADIANCE (ATMOSPHERIC CORRECTION)

Algorithm Improvement/Enhancement

1. Evaluation/Tuning of Algorithm Performance

Task Progress:

As indicated in our last Semiannual Report, considerable effort has been expended by R. Evans and co-workers toward removing the instrumental artifacts from Terra/MODIS ocean imagery. Examples of such artifacts are severe striping, mirror side differences, effects of the variation of the instruments response as a function of scan angle, and the influence of instrumental polarization sensitivity. Sufficient progress has been made along these lines that MODAPS has begun the first retrospective reprocessing of Terra/MODIS ocean data.

We have continued the improvement of Terra/MODIS imagery: we have

- helped refine calibration of MODIS in NIR and then visible,
- added a routine to include estimate of the water-leaving radiance in the NIR to improve the atmospheric correction in high-chlorophyll waters, and
- began an adjustment of the calibration of the fluorescence bands using an ocean-atmosphere model in the red and NIR.

In addition, we now believe there is a significantly larger fresnel-surface-reflection contribution in the case of MODIS compared to SeaWiFS. Part of this is the difference in equator crossing time that influences the sun-viewing geometry; however, we believe the effects are much larger than those caused by geometry alone. Although we have developed no conclusive answer yet, one possibility that we are investigating is the stabilization of the unstable morning atmosphere as the day progresses. In some cases the atmosphere may be unstable at the time of SeaWiFS overpass, but stable for the MODIS overpass. Atmospheric stability influences the sea surface roughness, which in turn influences its reflectance.

Anticipated Future Actions:

Although we will continue to work on Terra, our main effort under this task is to work with R. Evans in readying Aqua data for ocean processing. In addition, we will

compare Aqua and Terra in regard to the sea surface roughness effects. If our hypothesis is correct, the effects should be significantly smaller in Aqua than in Terra.

2. and 3. Algorithm Enhancements

There are two important issues we are examining for inclusion into the MODIS algorithm: effecting atmospheric correction in the presence of strongly absorbing aerosols and/or Case 2 waters; and including the influence of the subsurface upwelling BRDF on water-leaving radiance.

Strongly Absorbing Aerosols/Case 2 waters

The first of the two enhancements we have been considering concerns absorbing aerosols. It also concerns Case 2 (coastal) waters, as strongly absorbing aerosols can be expected near the coasts due to urban pollution. Although success with SeaWiFS has shown that the MODIS algorithm performs well in ~ 90% of Case 1 water situations, it does not perform adequately everywhere; most notably in atmospheres containing strongly absorbing aerosols, or in turbid coastal waters that have high concentrations of all optically active constituents. Two important situations in which absorbing aerosols make an impact are desert dust and urban pollution carried over the oceans by the winds. In the case of urban pollution the aerosol contains black carbon and usually exhibits absorption that is nonselective, i.e., the imaginary part of the refractive index (the absorption index) is independent of wavelength. In contrast, desert dust absorbs more in the blue than the red, i.e., the absorption index decreases with wavelength. Generally, analysis of imagery contaminated by strongly absorbing aerosols require that atmospheric correction and water-constituent retrieval be carried out simultaneously. The same is true for Case 2 coastal waters. Because of the similarity of the algorithm requirements, we treat absorbing aerosols and Case 2 waters together.

Task Progress:

Previously, we applied (and validated) the spectral optimization algorithm [R.M. Chomko and H.R. Gordon, Atmospheric correction of ocean color imagery: Test of the spectral optimization algorithm with SeaWiFS, *Applied Optics*, **40**, 2973—2984, 2001] with the Garver and Siegel reflectance model ["Inherent optical property inversion of ocean color spectra and its biogeochemical interpretation: 1 time series from the Sargasso Sea," *Geophys. Res.*, **102C**, 18607—18625, 1997] in Case 1 waters (See **Appendix I**). We have now applied of the spectral optimization algorithm to Case 2 waters using SeaWiFS data, and are in the process of debugging the code with MODIS imagery. Unlike Case 1 waters, in which phytoplankton and their immediate detritus control the optical properties, in Case 2 waters phytoplankton play a lesser role. For example, in coastal regions resuspended sediments from the bottom and/or sediments and dissolved organic material can be carried to the coasts by rivers, etc., may control the water's optical properties. These Case 2 waters are difficult to atmospherically correct because the water-leaving reflectance in the NIR is often not negligible. The effect of this is to

increase the top-of-atmosphere radiance at 750 nm compared to 869 nm. This is interpreted by the standard algorithm as an increase in the spectral variation of the aerosol optical thickness. In addition, high concentrations of dissolved organic material renders the top-of-atmosphere radiance similar to that expected for strongly-absorbing aerosols.

Thus, one modification that we made to the spectral optimization algorithm was to remove the simplifying assumption of negligible marine reflectance in the NIR. This was relatively straightforward to accomplish. First, we evoke the assumption of negligible marine reflectance in the NIR and operate the algorithm as in Case 1 waters. Next, we use the retrieved constituent concentrations to provide a new (non negligible) estimate the water-leaving radiance in the NIR. Finally, we subtract the newly estimated water-leaving radiances in the NIR from the total and operate the Case 1 algorithm again, etc. Such a modification enables use of the spectral optimization algorithm in waters with moderate sediment concentrations.

An example of the performance is provided in Figure 1. Here, ν is the Junge power-law size distribution parameter (spectral variation of the aerosol optical thickness is $\propto \lambda^{\nu-2}$), and ω_0 is the aerosol single scattering albedo. The image is from SeaWiFS October 6, 1997 over the Pamlico Sound. With the Case 1 processing, ν in the Sound increases over the open ocean value, while ω_0 decreases, i.e., the water properties are clearly influencing the retrieved aerosol properties. One would expect that the aerosol would have similar properties both over the Sound and over the open water to the east. When the algorithm is operated in the Case 2 mode as described in the last paragraph, the retrieved ν and ω_0 show far better continuity between the Sound and the open ocean, suggesting more accurate aerosol parameters were retrieved over the Sound with the Case 2 modification. This implies a much better atmospheric correction.

We have also replaced the Gordon et al. [A Semi-Analytic Radiance Model of Ocean Color, *Jour. Geophys. Res.*, **93D**, 10909-10924 (1988)] reflectance model with the Garver and Siegel (1997) model in our spectral matching algorithm for operation in wind-blown dust [C. Moulin, H.R. Gordon, R.M. Chomko, V.F. Banzon, and R.H. Evans, Atmospheric correction of ocean color imagery through thick layers of Saharan dust, *Geophys. Res. Lett.*, **28**, 5-8, 2001]. We tested it on a dusty image off West Africa with encouraging results, however, we continue to have problems if the candidate aerosol models include both dust and non-dust models. We are now in the process of debugging a version of the code for MODIS.

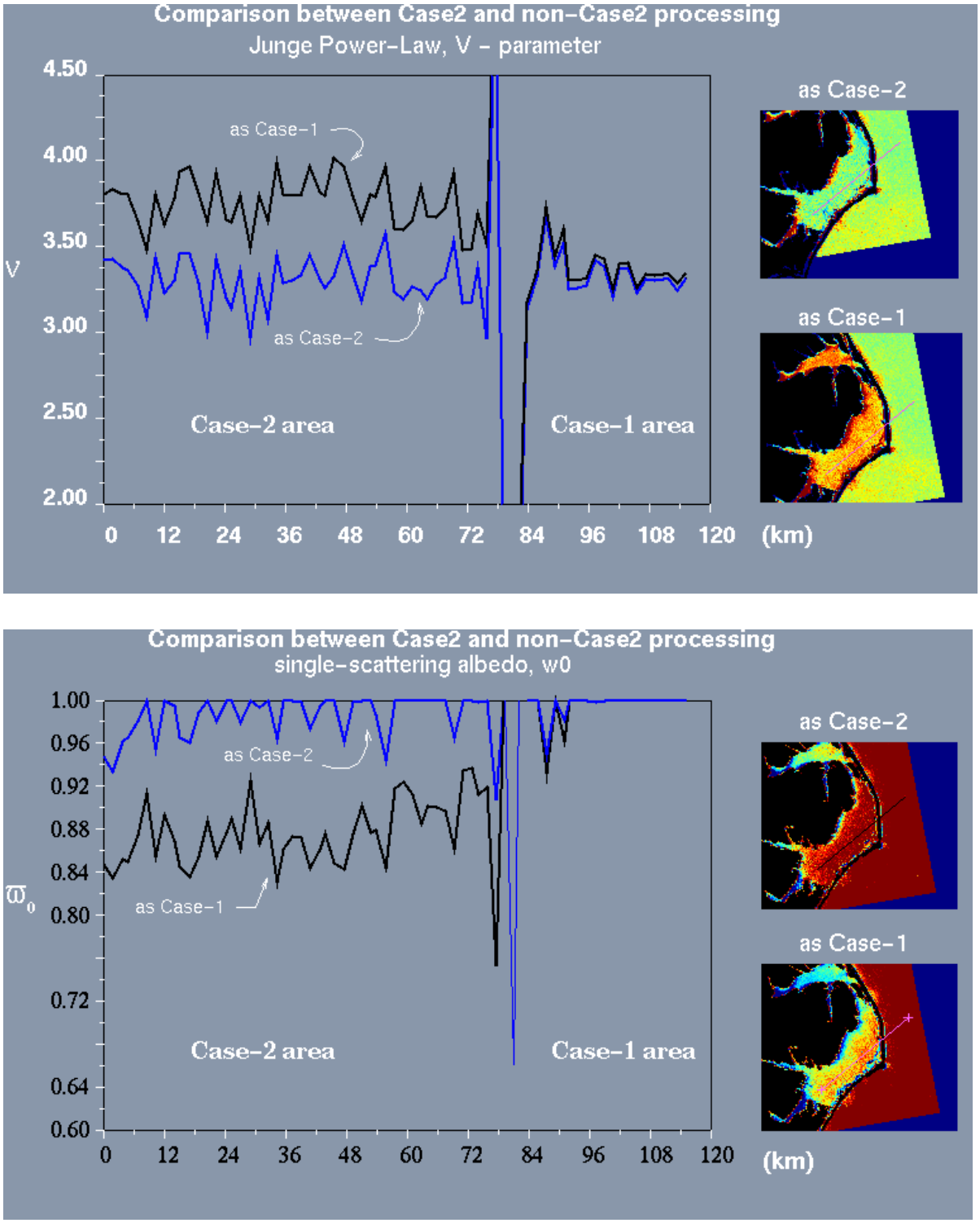

Figure 1: Junge power-law size distribution parameter ν (upper) and aerosol single scattering albedo ω_0 retrieved from a SeaWiFS image over Pamlico Sound comparing Case 1 and Case 2 processing. Graphs provide the retrieved values on the line drawn over the image.

Anticipated Future Actions:

We will continue to implement the absorbing aerosol algorithms into the MODIS processing code, as we believe they are the most versatile. In the case of the spectral matching algorithm we will examine its efficacy for atmospheric correction through African dust in the Arabian Sea. In the case of the spectral optimization algorithm for use in Case 2 waters, we will provide MODAPS with code for routinely processing a subsetted coastal region in a research mode. Although the code is very slow, application to a small region is feasible. Our goal for the next reporting period is to provide a demonstration of the value of MODIS imagery in Case 2 waters, as well as to provide users with the methodology and software tools for processing MODIS imagery in such waters. We are looking for coastal regions where algorithms of the Garver-Seigel type have been tuned to specific Case 2 waters. Likely candidates are the Chesapeake Bay and/or the Gulf of Maine. Thus, our longer-term goals are

- to provide MODIS code for Case 2 coastal waters, and
- to continue to evaluate MODIS retrieval in dust.

Both of these require coupled ocean and atmosphere retrievals.

The subsurface upwelling BRDF

The subsurface BRDF issue involves relating measurements of the upwelled spectral radiance (used for bio-optical algorithm development, sensor calibration and product validation of all ocean color sensors) that are predominately made in the nadir-viewing direction (including MOBY data), with the water-leaving radiance at the remote sensor. The remote sensing viewing geometry is rarely nadir, thus an understanding of the difference of these two geometries is required, i.e., we need to understand the BRDF of the subsurface radiance distribution to reconcile these measurements. Our approach is to directly measure the BRDF as a function of the chlorophyll concentration and to develop a model that can be used for MODIS. In addition we are working on a specific algorithm for correcting the MOBY buoy data to address the BRDF effects at this location.

Task progress:

During this period the majority of our effort on this task was spent on characterizing and calibrating the new NuRADS radiance distribution camera system. During the last period we had constructed the instrument and performed our first field test (in December). There were several areas we needed to work on to optimize the system. These included increasing the spectral blocking in the images, putting in extra stops to improve the imaging of the optical system, increasing the rigidity of the optical system, improving the heat flow in the system, and performing a complete characterization/calibration of the system. We also changed operating systems for the

onboard computer to improve stability. These steps were all done in preparation for a cruise/field experiment in May in Hawaii.

This cruise was timed to take place during the period when the sun achieves its maximum solar elevation in Hawaii. By taking data during cloud free periods of the day we get a complete set of clear water radiance distributions for all sun angles. To allow us to stay on a single station all day we used the small vessel in Hawaii, the R/V Klaus Wyrtki. Data were taken on several days from early in the morning until the sky became too cloudy. Along with the radiance distribution; sky irradiance, absorption and beam attenuation were measured continuously. Periodic casts were performed of the water upwelling radiance and irradiance along with water temperature to document the water column properties.

The modifications we had made were successful, and with these modifications we were able to operate the instrument during long continuous periods (5 hours or more) acquiring complete spectral radiance distribution sets every 2 minutes. There is a cruise report detailing the preliminary statistics of the cruise attached as **Appendix II**. In summary, we were able to acquire over 4900 spectral radiance distribution measurements (6 Gbytes of data) over the entire range of relevant solar zenith angles. We have completed the post cruise calibrations of the system and are just starting the data reduction process.

Anticipated Future Actions:

Our first step in the next reporting period will be to reduce the measurements acquired during the May cruise. As this is over 6 Gbytes of data it will take a significant portion of our time. In addition, we will be preparing manuscripts based on our recent BRDF measurements. By the end of this period we expect to have a model for the BRDF that will be applicable to the MOBY buoy. We will also be working on a model for the BRDF for use in general MODIS data, and will compare our data with an updated model by Morel of the BRDF.

Validation of MODIS Algorithms and Products

4. Participate in MODIS Initialization/Validation Campaigns

This task refers to our participation in actual Terra/MODIS validation/initialization exercises.

Task Progress:

While most of our effort the last six months has been directed towards the new radiance distribution camera system (NuRADS), we continued to maintain our CIMEL station in the Dry Tortugas during this period. This station will be used to help validate the MODIS derived aerosol optical depth (AOD), and aid in investigating the calibration of the near infrared (NIR) spectral bands of MODIS.

Last spring one of our graduate students operated a micro-pulse lidar (with his travel support coming from another project) during the ACE-Asia cruise fieldwork. One of the critical aspects of atmospheric correction is how to deal with vertical structure for absorbing aerosols. Previous fieldwork, during INDOEX and Aerosols99, gave us a general picture of the vertical structure of aerosols over the Atlantic and Indian Ocean, including regions of Saharan Dust and pollution events from the Indian sub-continent. ACE-Asia gave us vertical profiles of Asian Dust over the Pacific. We have been investigating different inversion methods to improve the accuracy of our vertical structure retrievals. We anticipate finishing the data reduction from this cruise during this next period.

Two of the instruments we operate during the larger MOCE cruises are the sky radiance distribution camera and the aureole camera system. Both of these camera systems are nearly 10 years old, and both failed in the period since the last MOCE cruise. We are currently replacing the cameras in both of these systems, and rebuilding the portions of the systems that require replacing.

Anticipated future efforts:

We will finish rebuilding the sky radiance camera system and the aureole camera system. In addition we are investigating various methods of calibration for these systems with the aim to improve our calibration accuracy.

We will participate in the next MODIS ship campaign when it occurs. The present schedule is for a cruise in October, which will be the post-launch cruise for Aqua, we will make measurements of the sky radiance distribution (large-angle and aureole), the in-water radiance distribution, AOD, and whitecap radiance during this cruise.

5. Complete Analysis of SeaWiFS Validation Campaign Data

Task Progress:

We have completed the reduction of the MOCE-5 BRDF data and have started to look at Andre Morel's model for the ocean BRDF, proposed for use in other ocean color sensors. We have been investigating the inversion of the sky radiance data acquired during the MOCE-5 cruise. We want to obtain the aerosol scattering phase function using this data. Unfortunately this has not worked well to date. We are currently examining possible reasons for the failure of the inversion technique.

Anticipated future efforts:

We will continue our effort to model the MOCE-5 BRDF data as a function of the chlorophyll concentration and will use this data to test the Morel model. We are also investigating reflectance-based field methods of calibrating the sky radiometers to improve the accuracy of the instrument calibration and hence the ability to perform inversions. Since the sky cameras have been very stable, if a constant offset can be found between the reflectance-based calibrations obtained in the field and the in-lab calibrations

we will be able to correct our previous calibrations and invert the sky data from the MOCE-5 cruise.

RETRIEVAL OF DETACHED COCCOLITH/CALCITE CONCENTRATION MOD 23

William M. Balch
Bigelow Laboratory for Ocean Sciences
POB 475
McKown Point
W. Boothbay Harbor, ME 04575

This last half year of work has focussed on several areas: 1) processing of 2001 Gulf of Maine PIC data 2) work-up of chalk-ex results, 3) acquisition of 2002 samples for MODIS validation, 4) completion of a manuscript on optics and hydrography of the Gulf of Maine (which includes material on acid-labile backscattering due to PIC), submittal of a manuscript on the scattering properties of suspended opal, as it might affect the PIC algorithm, 5) presentation of MODIS results at several international meetings.

Algorithm Evaluation/Improvement

Task Progress:

Algorithm evaluation for MOD 23 has required waiting for the new processing of the MODIS radiance data with version 3.4 of the code, to correct for instrumental artifacts such striping, mirror side differences, effects of the variation of the instrument's response as a function of scan angle, and the influence of instrument polarization sensitivity. R. Evans and his group at the University of Miami have admirably completed these corrections during the spring, and much of the historical imagery now has been re-processed with new software. We have since verified the particulate inorganic carbon (PIC) algorithm output as produced by Miami and MODAPS and confirmed consistent calculations. Moreover, as a separate, independent check, we have independently implemented the PIC algorithm at Bigelow using the MODIS nLw's as input and confirmed the correct code implementation.

Validation of MODIS Algorithms and Products

As coccoliths and suspended PIC (particulate inorganic carbon or calcium carbonate) are new products, and as Terra was only launched in December 1999, there are relatively few data sets available for validation, particularly for the coccolith and suspended calcite products. This is because coccolith concentration (PIC) is not frequently measured at sea, while chlorophyll concentration is. In conjunction with NASA SIMBIOS activities, much of our validation estimates come from the Gulf of

Maine, the site of frequent blooms of coccolithophores, and a region readily accessible from our laboratory.

Validation of regional PIC

During 2001, we acquired 103 new PIC samples from our Gulf of Maine ferry studies. These were processed during this last half year, and data have been processed and entered into spreadsheets. Coccolith samples were taken at the same 103 stations, and those tedious microscope counts are ongoing. Parallel PIC samples and coccolith counts are taken in order to check the coccolith-to-carbon conversion which is implicit in the MODIS two band algorithm.

Chalk-Ex

Another 96 PIC samples were taken during our recent Chalk-Ex cruise. These were processed during the last half year, the results recently were returned from the Scripps Analytical Facility and entered into spreadsheets for comparison to MODIS re-processed satellite results. The Chalk-Ex and 2000-2001 Gulf of Maine PIC results are being combined into one validation data set and the results will be presented at the upcoming July '02 MODIS meeting in Greenbelt, MD.

New validation data

Gulf of Maine cruises began on the M/S *Scotia Prince* ferry in early May of 2002. To date, four cruises have been performed, all under sunny skies with good Terra (and now Aqua!) overpasses. Eight more cruises will be completed in the next half year.

Checks of global data set

As a means to cross-check the PIC algorithm, we have estimated total global PIC using the 36km monthly averaged data, and compared it to POC estimates based on the algorithm of Morel (1991). For our last semi-annual report, we reported this analysis for 5 months of processed data; here we report results for 14 months. The data represent the first estimate of the annual cycle of PIC in surface waters of the globe. These estimates are quite reasonable compared to empirical and modeled estimates that can be deduced from budgets of Milliman (1993; 1999).

<u>Validation of global PIC and coccolithophore pigment data</u>

Cautions When Using coccolith/PIC data products

The coccolithophore data products should be treated as "preliminary," until we have completed the validation of the product using Version 3.4 code, and data are re-checked against shipboard validation samples. Note, it is expected that if east-west problems indeed are resolved, we will have many more samples to include in the validation. Moreover, given the polarization and response versus scan angle problems inherent with Versions 3.2 and 3.3 of the processing code, we do not recommend using these MODIS coccolithophore data products from this code unless they are from the western third of the MODIS swath. We also caution using these data from shallow ocean regions, particularly near carbonate banks (e.g. Grand Bahamas), where bottom

reflectance will appear as a high-reflectance coccolithophore bloom (presumably such pixels would be flagged due to their shallowness). Moreover, near river mouths and in shallow waters, resuspended sediments (of non-calcite origin) may appear as high suspended calcite concentrations. Only use these data if the waters are sufficiently deep to not have such bottom resuspension or direct river impact. Beware that MODIS-derived coccolith concentrations assume that the coccoliths are from the prymnesiophyte, *E. huxleyi*. If this is not true, then inaccuracies will increase although the errors are not expected to be large. Even when using the data in units of mg m^{-3}, they nevertheless assume a constant backscattering cross-section for *E. huxleyi*, which is known to vary with the size of the calcite particle.

Anticipated future efforts:

Our efforts in the coming 6 months will be on:

a) Continued sampling for PIC validation using the M/S Scotia Prince ferry

> We have 8 more trips scheduled for 2002 which will be finished by November. These trips involve significant numbers of PIC samples and are planned for clear days to maximize satellite coverage.

b) Further write-up of our Gulf of Maine results and PIC algorithm results

> We have a total of three papers in preparation on the Gulf of Maine results. The first is close to submission. Work on the other two papers will proceed then. We will also begin work on the PIC algorithm and its performance.

c) Preparing for the third Chalk-Ex experiment in '03

> Our last chalk experiment is slated for June '03, but we will begin preparations by the Fall. We also continue work-up of the ship radiance data for comparison to the MODIS data.

Web Links to Relevant Information

The algorithm theoretical basis document for the coccolithophore products can be found at: http://modis.gsfc.nasa.gov/MODIS/ATBD/atbd_mod23.pdf

More information about the algorithm and inputs can be found in:

Esaias, W., et al., 1998, Overview of MODIS Capabilities for Ocean Science Observations, *IEEE Transactions on Geoscience and Remote Sensing*, **36**, 1250—1265.

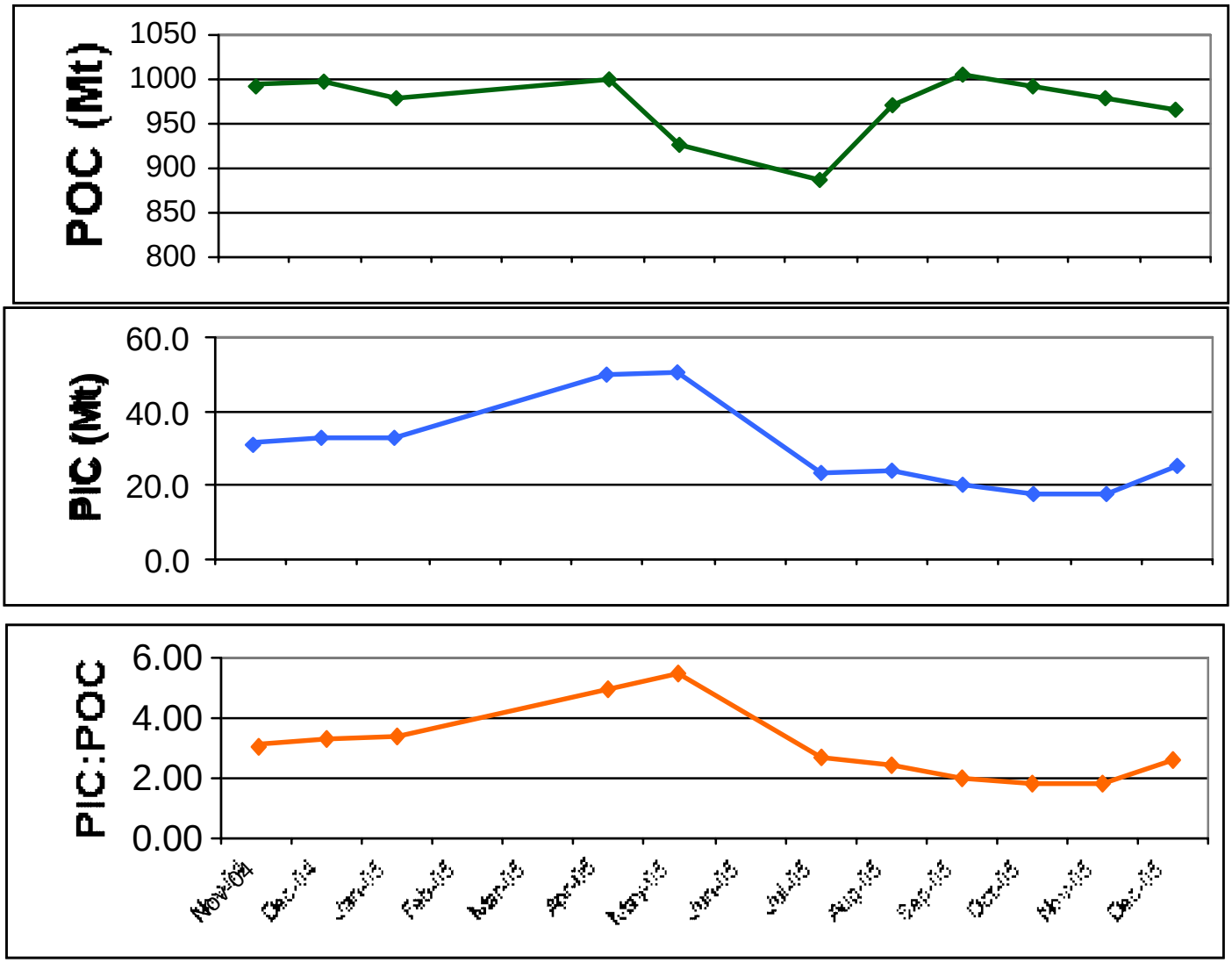

Figure 2. Global euphotic estimates of PIC (Mt), POC (Mt) and PIC:POC ratio based on 14 months of 36 km MODIS data between November '00 to December '01. PIC determined using two-band algorithm. POC estimates based on algorithm of Morel (1991) which relates chlorophyll to POC. Both PIC and POC integrated to base of euphotic zone using estimates of Kpar (also based on Morel (1991) chlorophyll vs. Kpar relationship). This figure provides the first view of the annual global changes in PIC. The results suggest that global PIC:POC of surface particulate matter varies by a factor of 2.5 over the year.

Referencing Data in Journal Articles

Results derived from this algorithm should cite the paper of Gordon et al.(Gordon et al., 1988) for the original discussion, and (Balch et al., 1999; Balch et al., 1996) for field data on the backscattering cross-section of calcite.

Citations

Balch, W.M., Drapeau, D.T., Cucci, T.L., Vaillancourt, R.D., Kilpatrick, K.A. and Fritz, J.J., 1999. Optical backscattering by calcifying algae--Separating the contribution by particulate inorganic and organic carbon fractions. Journal of Geophysical Research 104, 1541-1558.

Balch, W.M., Kilpatrick, K., Holligan, P.M., Harbour, D. and Fernandez, E., 1996. The 1991 coccolithophore bloom in the central north Atlantic. II. Relating optics to coccolith concentration. Limnology and Oceanography 41, 1684-1696.

Gordon, H.R., Brown, O.B., Evans, R.H., Brown, J.W., Smith, R.C., Baker, K.S. and Clark, D.K., 1988. A semianalytic radiance model of ocean color. Journal of Geophysical Research 93, 10909-10924.

Milliman, J., 1993. Production and accumulation of calcium carbonate in the ocean: Budget of a nonsteady state. Global Biogeochemical Cycles 7, 927-957.

Milliman, J., Troy, P.J., Balch, W., Adams, A.K., Li, Y.-H. and MacKenzie, F.T., 1999. Biologically-mediated dissolution of calcium carbonate above the chemical lysocline? Deep-Sea Research 46, 1653-1669.

Morel, A., 1991. Light and marine photosynthesis: A spectral model with geochemical and climatological implications. Progress in Oceanography 26, 263-306.

ADDITIONAL DEVELOPMENTS

Presentations(2002)

(NAS5-31363 Personnel bold highlighted)

Balch, W. M. 2002. New observations of coccoliths from satellites, ferries, towed vehicles and balloons. Keynote talk. Coccolithophores- from molecular processes to global impact. Conference at Centro Stefano Franscini, Monte Verita, Ascona, Switzerland, 10-15 February 2002.

Balch, W.M., Bowler, B., Drapeau, D., **Gordon, H**., Scally, E., Ashe, A. 2002. Quantitative, space-based measurements of oceanic suspended ocean calcium carbonate with MODIS and SeaWiFS. AGU/ASLO Ocean Sciences Meeting, Honolulu, Hawaii. February 2002.

Drapeau, D. T., **W.M. Balch**, B.C. Bowler, E. Scally, J. Goes, A. Ashe. 2002. A multi-year record of bio-optical properties in the Gulf of Maine. AGU/ASLO Ocean Sciences Meeting, Honolulu, Hawaii. February 2002.

Publications (2002):

(NAS5-31363 Personnel bold highlighted)

Campbell, J., D. Antoine, R. Armstrong, **W. Balch**, R. Barber, and others. 2002. Comparison of algorithms for estimating primary productivity from surface chlorophyll temperature and irradiance. *Global Biogeochem. Cycles*.(In press).

Cattrall, C., K.L. Carder, K.T. Thome, **H.R. Gordon**, Solar-reflectance-based calibration of spectral radiometers, *Geophys. Res. Lett.*, (In Press).

Chomko, R.M., **H. R. Gordon**, S. Maritorena, and D.A. Siegel, Simultaneous retrieval of oceanic and atmospheric parameters for ocean color imagery by spectral optimization: A validation, *Remote Sensing of Environment* (In Press).

Quinn, P. K. , D.J. Coffman, T.S. Bates, T.L. Miller, J.E. Johnson, **E.J. Welton**, C. Neusüss, M. Miller, and P. J. Sheridan, Aerosol Optical Properties during INDOEX 1999: Means, Variability, and Controlling Factors, *Journal of Geophysical Research* (In Press).

Wang,M., **and H.R. Gordon**, Calibration of ocean color scanners:How much error is acceptable in the near infrared?, *Remote Sensing of Environment* (In Press).

Welton, E. J., P. J. Flatau, **K. J. Voss**, **H. R. Gordon**, K. Markowicz, J. R. Campbell, and J. D. Spinhirne, Micro-pulse Lidar Measurements of Aerosols and Clouds During INDOEX 1999, *Journal of Geophysical Research* (In Press).

Other Works Submitted or in Preparation

Broerse, A.T.C., Tyrrell, T., Young, J. R., Poulton, A. J., Merico, A. and **W. M. Balch**. The cause of bright waters in the Bering Sea in winter. 2002 Submitted to *Cont. and Shelf Research*

Balch, W. M., D. Drapeau, B. Bowler, E. Booth, J. Goes, A. Ashe, and J. Frye. A multi-year record of optical properties in the Gulf of Maine: I. Spatial and temporal variability. to be submitted to *Progress in Oceanography*.

Balch, W. M., D. Drapeau, B. Bowler, E. Booth, J. Goes, A. Ashe, and J. Frye. A multi-year record of optical properties in the Gulf of Maine: II. Connections between optics and hydrography. to be submitted to *Journal of Plankton Research*.

Cattrall, C. K.L. Carder, and **H.R. Gordon**, Columnar aerosol single-scattering albedo and phase function retrieved from sky radiance over the oceans: Measurements of African dust, *Jour. Geophys. Res*., (Submitted).

Gordon, H.R., Comment on "Pitfalls in atmospheric correction of ocean color imagery: how should aerosol optical properties be computed?" *Applied Optics*, (Submitted)**.**

Vaillancourt, R.D., C.W. Brown, R.R.L. Guillard, **W. M. Balch**. Submitted. Light backscattering by phytoplankton algae and a heterotrophic bacterium measured with a multi-wavelength, fixed-angle backscattering meter. *Jour. Geophys. Res.*

APPENDIX I

Simultaneous retrieval of oceanic and atmospheric parameters for ocean color imagery by spectral optimization: A validation

by

Roman M Chomko, Howard R. Gordon, Stephane Maritorena, and David A. Siegel

RSE 02-006

Simultaneous retrieval of oceanic and atmospheric parameters for ocean color imagery by spectral optimization: A validation

by

Roman M Chomko,[1] Howard R. Gordon,[1] Stephane Maritorena,[2] David A. Siegel[2,3]

[1]Department of Physics
University of Miami
Coral Gables, FL 33124

[2]Institute for Computational Earth System Science
University of California, Santa Barbara
Santa Barbara, CA 93106

[3]Department of Geography
University of California, Santa Barbara
Santa Barbara, CA 93106

Acknowledgement

This research was support by NASA Contracts NAS5-31363 (HRG), NAS5-31734 (HRG), NAS5-0096 (SM), NAS5-99083 (DAS) and NAG5-9818 (DAS). The authors would like to thank the SeaWiFS Project (Code 970.2) and the Distributed Active Archive Center (Code 902) at the Goddard Space Flight Center, Greenbelt, MD 20771, for the production and distribution of these data, respectively. These activities are sponsored by NASA's Earth Science Enterprise Program. Finally, we extend our thanks to the NASA Airborne Oceanographic Lidar Team for providing the CDOM measurements, and to the reviewers for helpful suggestions.

Keywords: Ocean color; Chlorophyll; CDM, Aerosols; Atmospheric Correction; SeaWiFS

Abstract

We report application and validation of a spectral optimization algorithm for processing SeaWiFS data in Case 1 waters. The algorithm couples a simplified aerosol model with a sophisticated water-reflectance model to simultaneously retrieve both atmospheric and ocean parameters. Two of the retrieved ocean properties – the absorption coefficient of colored detrital material and the chlorophyll *a* concentration – are validated by comparison with "surface" truth obtained with airborne and space borne sensors. We show that employing a more complete water reflectance model significantly improves the decoupling between the oceanic and atmospheric optical signals. Methodologies for applying the algorithm to Case 2 waters and for delineating terrestrial vs. marine CDOM are suggested.

Introduction

Traditionally, ocean color imagery has been processed in two sequential steps (e.g., Gordon and Morel, 1983). First, an atmospheric correction algorithm is applied to remove the effects of the atmosphere and enable retrieval of the water-leaving reflectance (ρ_w) from the satellite-measured reflectance of the ocean-atmosphere system (ρ_t). Then, the water-leaving reflectances are used in a bio-optical algorithm to extract the chlorophyll concentration associated with phytoplankton in the surface waters. In the case of SeaWiFS (Hooker *et al*., 1992) the Gordon and Wang (1994) atmospheric correction procedure is applied and the chlorophyll concentration is retrieved from ρ_w using bio-optical algorithms such as described by O'Reilly *et al*. (1998). A main problem with this approach is accounting for absorbing aerosol effects. The Gordon and Wang (1994) algorithm uses spectral bands in the near infrared (NIR), where $\rho_w \approx 0$, to assess the aerosol's contribution to the reflectance in the visible. This approach is applicable only for a non- or weakly-absorbing aerosol (Gordon, 1997). When the aerosol is strongly absorbing, associated with both soot or dust aerosols, the NIR reflectance provides no clue to the visible reflectance. This means that the two-step process will fail in the presence of strongly absorbing aerosols, so the visible bands must be used to assess the aerosol absorption. Employing the visible bands, where $\rho_w \neq 0$, requires coupling the ocean property retrieval and the atmospheric correction.

Such coupled algorithms for retrieval of the chlorophyll concentration date back to the proof-of-concept Coastal Zone Color Scanner mission (CZCS, Hovis *et al.*, 1980). The CZCS lacked spectral bands in the NIR, the longest wavelength usable channel being at 670 nm. The initial CZCS algorithms (Gordon *et al.*, 1980) assumed that the water-leaving reflectance at 670 nm in Case 1 waters was null at all trophic levels. [Case 1 waters are defined to be those for which the optical properties are determined by the water itself and phytoplankton along with their immediate detrital material (Gordon and Morel 1983). Most of the world oceans are Case 1 waters, the remaining are called Case 2 waters, comprising, for example, coastal waters subject to riverine input, re-suspended sediments from the bottom, etc.] This assumption allowed assessment of the atmospheric effects at 670 nm, leading to an atmospheric correction. However, at even mesotrophic chlorophyll concentrations the water-leaving reflectance is already detectable in the NIR (Siegel *et al.*, 2000) and is even larger in the red. Thus, in general the CZCS had no band that was free of ρ_w, and therefore algorithms that coupled ocean property retrieval and atmospheric correction were developed to overcome this difficulty. Some algorithms used empirical relationships between the water-leaving reflectance in the four CZCS visible bands (Smith and Wilson 1981); others used semi-analytic models relating the four water-leaving reflectances to the phytoplankton pigment concentration (Bricaud and Morel 1987; Andre and Morel, 1991). All solved the resulting set of nonlinear equations using iterative techniques. SeaWiFS was designed to overcome this difficulty with the addition of spectral bands in the NIR; however, similar techniques are still required for sediment-dominated (Case 2) coastal waters or eutrophic Case 1 waters in which the

water-leaving reflectance even in the NIR cannot be ignored (Ruddick *et al*., 2000; Siegel *et al*., 2000).

Several recent attempts have been made to develop coupled ocean-atmosphere correction algorithms for retrieving ocean and aerosol properties through an atmosphere characterized by absorbing aerosols (Gordon *et al*., 1997; Chomko and Gordon, 1998). These coupled algorithms use bio-optical models relating the ρ_w to the water's constituents and aerosol models (particle size frequency distribution and complex refractive index) relating the aerosol's contribution to ρ_t as a function of its concentration. Retrieval of the oceanic and atmospheric parameters is then effected by finding the combination of parameter values and an aerosol model that best reproduce the measured ρ_t throughout the spectrum.

Moulin *et al*. (2001a) adapted the Gordon *et al*. (1997) spectral-matching algorithm to effect atmospheric correction of SeaWiFS imagery in the presence of Saharan dust off the coast of West Africa. To implement the algorithm, they used SeaWiFS to develop aerosol models specifically tuned to capture the spectral variation of the dust's contribution to ρ_t (Moulin *et al*., 2001b). This was necessary because (unlike most aerosols) Saharan dust absorption is a strong function of wavelength – increasing dramatically from red to blue – requiring the imaginary part of the particle refractive index (the absorption index) to be wavelength dependent. They showed that successful atmospheric correction was possible under conditions when the optical thickness of the dust was as high as 0.8.

Chomko and Gordon (2001) reported the successful operation of a spectral optimization algorithm (SOA, Chomko and Gordon, 1998) for simultaneous atmospheric correction and retrieval of water properties from SeaWiFS imagery. In this algorithm, no effort was made to precisely model the aerosol. Rather, a simple one-parameter Junge-distributed collection of spherical particles was used for the size-shape distribution, along with a wavelength-independent complex refractive index. Such an aerosol model should be adequate for atmospheric correction when the aerosol is non-absorbing or when the absorption index is independent of wavelength, e.g., black carbon. Application to imagery off the U.S. East Coast showed consistent retrieved water properties between days with turbid and clear atmospheres. However, aerosol properties (particularly the aerosol single scattering albedo) were not well-retrieved in clear atmospheres, presumably because large variations in aerosol properties produced only small changes in ρ_t at low aerosol concentration. Unfortunately, because the bio-optical model differed considerably from that for the standard SeaWiFS processing, an unbiased comparison of the SOA and SeaWiFS ocean products was not possible.

Both of these above implementations of coupled ocean-atmosphere algorithms used the Gordon *et al*. (1988) two-parameter radiance model to provide the oceanic reflectance. The Gordon *et al.* model expresses the water-leaving radiance as a function of the pigment concentration *P* and a scattering parameter. However, more complete radiance models are now available (Garver and Siegel, 1997; Carder *et al.* 1999; Maritorena *et al*. 2002). These models make it possible to obtain ocean parameters in addition to the chlorophyll *a* concentration such as particulate backscatter and the

absorption by colored dissolved and detrital particulate materials (CDM). In this paper we combine a globally tuned version of the Garver and Siegel (1997) bio-optical model (Maritorena et al. 2002; hereafter referred to as GSM01) with an improved version of the Chomko and Gordon (1998) SOA. This will enable us to retrieve a set of ocean parameters along with estimates of aerosol optical properties. The ocean retrievals are validated using a combination of airborne laser fluorescence transect observations and SeaWiFS operational products. Comparison of the SOA retrievals with the laser fluorescence estimates of CDM suggests a path by which terrestrial vs. marine dissolved materials may be distinguished with the next generation of ocean color satellite imagery. In addition, we show that the difficulty in retrieving aerosol properties in relatively clear atmospheres is minimized using the GSM01 bio-optical algorithm.

We begin by briefly reviewing radiative transfer, the aerosol models, and the bio-optical model. Next, we describe the mechanics of the spectral optimization algorithm, and validate its retrieval of water properties. Finally, we show that the retrieved aerosol properties are almost completely decoupled from the ocean properties in both clear and turbid atmospheres.

Radiative Transfer

The reflectance $\rho_t(\lambda)$ of the ocean-atmosphere system at a wavelength λ can be expressed as

$$\rho_t(\lambda) = \rho_r(\lambda) + \rho_A(\lambda) + t_v(\lambda)t_s(\lambda)\rho_w(\lambda)\,, \qquad (1)$$

where $\rho_r(\lambda)$ is the pure Rayleigh scattering contribution, $\rho_A(\lambda)$ is the aerosol contribution (in the *presence* of Rayleigh scattering), and $\rho_w(\lambda)$ is the normalized water-leaving reflectance. The quantities $t_s(\lambda)$ and $t_v(\lambda)$ are the diffuse transmittances of the atmosphere from the sun to the sea surface and from the sensor to the sea surface, respectively. The atmospheric contribution $\rho_r(\lambda) + \rho_A(\lambda)$ includes light specularly reflected from the sea surface as well as scattered in the atmosphere. All of the information regarding the water's constituents resides in $\rho_w(\lambda)$. Note that we have simplified the earlier notation wherein $\rho_w(\lambda)$ was written $[\rho_w(\lambda)]_N$ (Gordon, 1997), and $\rho_A(\lambda)$ was written $\rho_a(\lambda)+\rho_{ra}(\lambda)$, where $\rho_a(\lambda)$ is the reflectance contribution from aerosol scattering in the *absence* the Rayleigh scattering by the air, and $\rho_{ra}(\lambda)$ a correction term resulting from interaction between Rayleigh and aerosol scattering (Gordon and Wang, 1994).

The Aerosol Model

The atmospheric contribution $\rho_r(\lambda) + \rho_A(\lambda)$ is computed from an aerosol model in the following manner. First $\rho_r(\lambda)$ is computed at all wavelengths using a radiative transfer code in which the aerosol-free atmosphere is bounded by a (flat) Fresnel reflecting ocean that absorbs all photons penetrating the surface. Then the same code is used with a model aerosol uniformly mixed with air from the surface to 2 km to compute $\rho_r(\lambda) + \rho_A(\lambda)$, the atmospheric contribution when $\rho_w(\lambda)= 0$, as a function of the aerosol optical thickness at 865 nm (τ_a). Finally, $\rho_r(\lambda)$ is subtracted from $\rho_r(\lambda) + \rho_A(\lambda)$ to provide $\rho_A(\lambda)$

as a function of τ_a. In the aerosol model, particles are distributed according to a Junge power law:

$$\frac{dN}{dD} = 0\,,\ D < D_0,$$

$$\frac{dN}{dD} = \frac{K}{D_1^{\nu+1}}\,,\ D_0 \le D \le D_1,$$

$$\frac{dN}{dD} = \frac{K}{D^{\nu+1}}\,,\ D_1 \le D \le D_2, \tag{2}$$

$$\frac{dN}{dD} = 0\,,\ D > D_2,$$

where D is the particle diameter and dN is the number of particles per unit volume in the size interval $D \pm dD/2$. We take D_0 = 0.06 μm, D_1 = 0.20 μm, and D_2 = 20 μm. The optical properties of the aerosol are computed from Mie theory using the above size distribution and the complex index of refraction $m = m_r - m_i$. In the present application, m_r is either 1.50 or 1.333, and m_i = 0, 0.001, 0.003, 0.010, 0.030, and 0.040. The parameter ν ranges from 2.0 to 4.5 in steps of 0.5. Thus, there are 72 separate aerosol models (2 values of $m_r \times$ 6 values of $m_i \times$ 6 values of ν). For each of these models, $\rho_A(\lambda)$ is computed as a function of the aerosol optical thickness $\tau(\lambda)$ for a wide range of viewing and solar geometries and fit to a quartic expression

$$\rho_A(G,\lambda,m_r,m_i,v) = a(G,\lambda,m_r,m_i,v)\tau(\lambda) + b(G,\lambda,m_r,m_i,v)\tau^2(\lambda) + c(G,\lambda,m_r,m_i,v)\tau^3(\lambda) + d(G,\lambda,m_r,m_i,v)\tau^4(\lambda), \quad (3)$$

where G indicates a particular geometry. The quantities a, b, c, and d are then stored as lookup tables (LUTs) for use by the optimization procedure. The diffuse transmittances are computed separately by assuming that the in-water upwelling radiance distribution just beneath the surface is uniform (Yang and Gordon 1997).

The Bio-optical Model

In most ocean reflectance models, the water-leaving reflectance (ρ_w) is provided as a function of the absorption (a) and backscattering (b_b) coefficients. The (spectral) absorption and backscattering coefficients are separated into the constituent components plus that of water: $a(\lambda) = a_w(\lambda) + a_{ph}(\lambda) + a_{dp}(\lambda) + a_{CDOM}(\lambda)$ and $b_b(\lambda) = b_{bw}(\lambda) + b_{bp}(\lambda)$, where the subscripts "*w*", "*ph*", "*dp*", "*CDOM*", and "*p*" refer, respectively, to water, phytoplankton, detrital particles, colored dissolved organic matter, and particles of all kinds. Working with a limited data set, Gordon *et al*. (1988) related the absorption of all of the components to the pigment concentration. Particle backscattering was also modeled as function of P. Hence, the water-leaving reflectance spectrum depended on a

single free parameter, P, which assumes that fixed relationships exist between $a_{ph}(\lambda)$, $a_{dp}(\lambda)$ and $a_{CDOM}(\lambda)$ and P.

Recent models for ocean reflectance provide more information than a simple measure of pigment concentration by retrieving relevant optical properties individually (e.g., Lee *et al.*, 1994; Roesler and Perry, 1995; Hoge and Lyon, 1996; Garver and Siegel, 1997; Carder *et al.*, 1999). These models typically combine $a_{dp}(\lambda) + a_{CDOM}(\lambda)$, due to their similar spectral signatures, to form $a_{cdm}(\lambda) \equiv a_{dp}(\lambda) + a_{CDOM}(\lambda)$ (the absorption coefficient of colored detrital material or CDM). However, the remaining components are retrieved individually. The GSM01 model (Garver, and Siegel, 1997; Maritorena *et al.* 2002) retrieves three parameters: (1) the absorption coefficient of colored detrital matter at 443 nm ($a_{cdm}(443)$); (2) the chlorophyll *a* concentration C, and (3) the backscattering coefficient of particulate matter at 443 nm ($b_{bp}(443)$). Specifically, the non-water components are modeled as

$$a_{ph}(\lambda) = C \; a_{ph}^{*}(\lambda), \tag{4}$$

$$a_{cdm}(\lambda) = a_{cdm}(443) \exp(-S(\lambda - 443)), \tag{5}$$

$$b_{bp}(\lambda) = b_{bp}(443) \, (443/\lambda)^{n}, \tag{6}$$

where $a_{ph}^{*}(\lambda)$ is the chlorophyll specific absorption coefficient spectrum for phytoplankton, S is the CDM spectral "slope" parameter and n parameterizes the spectral variation of the particle backscattering. The difficulty in developing these models is the sensitivity of retrievals to choices of the parameters in the models ($a_{ph}^{*}(\lambda)$, S and n;

Garver and Siegel, 1997; O'Reilly *et al.*, 1998). In the GSM01 model these parameter values have been optimized for global applications by using an extended version of the SeaBAM data set (Maritorena *et al.*, 2002). A global optimization procedure determined the "best" values of $a_{ph}^{*}(\lambda)$, S and n, for retrieving the three unknowns – C, $a_{cdm}(443)$, and $b_{bp}(443)$. Details concerning the GSM01 model and its global tuning can be found in Maritorena *et al.* (2002). The GSM01 water reflectance model can then be represented functionally as,

$$\hat{\rho}_w(\lambda) = \hat{\rho}_w(\lambda; C, a_{cdm}(443), b_{bp}(443)). \qquad (7)$$

Note that $\rho_w(\lambda)$ is assumed to be independent of illumination or viewing geometry and that henceforth, a circumflex will indicate a modeled quantity.

The GSM01 model has the advantage that it is a function only of wavelength and the three retrieved products. This makes it straightforward to implement in the SOA procedure. For example, Carder *et al.* (1999) use essentially the same decomposition of absorption and scattering coefficients; however, their expression for $b_{bp}(\lambda)$ contains parameters that are dependent upon reflectance itself. This makes the model difficult to implement in the present procedure. It is important to note that the GSM01 model is tuned to essentially the same data set as the O'Reilly *et al.* (1998) bio-optical algorithms and when tested with in situ data performs identically as the standard empirical algorithm used in processing SeaWiFS imagery (Maritorena *et al.*, 2002). Hence, the GSM01 and the standard SeaWiFS processing should result in the same chlorophyll *a* concentration

given the same $\rho_w(\lambda)$ estimates. This enables us to assess the SOA retrievals of C using standard SeaWiFS-data products.

The Optimization Procedure

The coupling of the atmosphere and ocean reflectance models is achieved as follows. The Rayleigh contribution $\rho_r(\lambda)$ is first subtracted from $\rho_t(\lambda)$ for each SeaWiFS band. One is then left with

$$\rho_{Aw}(G,\lambda,measured) \equiv \rho_A(G,\lambda) + t_v(G,\lambda)t_s(G,\lambda)\rho_w(\lambda)\,. \tag{8}$$

The modeled counterpart of ρ_{Aw} can be expressed as

$$\begin{aligned}\hat{\rho}_{Aw}(G,\lambda,m_r,m_i,\nu,\tau_a,C,a_{cdm}(443),b_b(443) \equiv\ & \hat{\rho}_A(G,\lambda,m_r,m_i,\nu,\tau_a) \\ & + \hat{t}_v(G,\lambda,m_r,m_i,\nu,\tau_a)\hat{t}_s(G,\lambda,m_r,m_i,\nu,\tau_a) \\ & \times \hat{\rho}_w(\lambda,C,a_{cdm}(443),b_{bp}(443)).\end{aligned} \tag{9}$$

We assume that the water-leaving reflectance in the 765 nm and 865 nm SeaWiFS bands is negligible, which allows the direct estimation of ν and τ_a from determinations of $\rho_{Aw}(765)$ and $\rho_{Aw}(865)$ (Chomko and Gordon, 2001). However, rather than using the method described by Chomko and Gordon (2001, 1998), wherein an average (over all m_r and m_i) value of ν is estimated at each pixel, we require an exact fit to $\rho_A(765)$ and $\rho_A(865)$ for each (m_r,m_i) combination. This results in twelve values of ν and τ_a, for which the functions $\nu = \nu(m_r,m_i)$ and $\tau_a = \tau_a(m_r,m_i)$ are established by interpolation (Figure 1 in

Gordon and Chomko (1998) shows that for a given $\rho_A(765)$ and $\rho_A(865)$, the value of $\nu(m_r,m_i)$ can vary as much as ±0.2 to ±0.4 from the mean as m_r and m_i are varied.). Thus given the functions $\nu(m_r,m_i)$ and $\tau_a(m_r,m_i)$, we minimize the quantity

$$\sum_{\lambda_i}\left\{\hat{\rho}_{Aw}(G,\lambda_i,m_r,m_i,\nu,\tau_a,C,a_{cdm}(443),b_{bp}(443))-\rho_{Aw}(G,\lambda_i,measured)\right\}^2 \quad (10)$$

over the remaining 6 SeaWiFS bands using standard optimization techniques to find the other 5 parameters to provide aerosol and ocean parameters simultaneously. In effect, we have optimized for 7 parameters:

$$C,\ a_{cdm}(443),\ b_{bp}(443),\ \nu,\ \tau_a,\ m_r,\ \text{and}\ m_i;$$

using the 8 spectral bands of SeaWiFS and the constraint that $\hat{\rho}_{Aw} = \rho_{Aw}$ *exactly* in the NIR. In the optimization, $\hat{\rho}_A(G,\lambda,m_r,m_i,\nu,\tau_a)$ is interpolated over the 72 grid (model) points. For interpolation in the m_i direction we interpolate on $m_i^{1/4}$ rather than m_i itself as $\hat{\rho}_A(G,\lambda,m_r,m_i,\nu,\tau_a)$ is closer to linearity as a function of $m_i^{1/4}$. No interpolation is required for $\hat{\rho}_w(\lambda)$ as an analytic formulation is used.

Application to SeaWiFS Imagery

We applied the SOA algorithm to a full resolution SeaWiFS image from the Middle Atlantic Bight (MAB) acquired on day 279 of 1997. As described in Chomko and Gordon (2001), the atmosphere over the MAB on this day was quite turbid with $\tau_a(865)$ exceeding 0.2 over significant portions of the image. Retrieved images of $a_{cdm}(443)$, C, and $b_{bp}(443)$ are shown in Figures 1, 2, and 3, respectively. As expected, strong gradients of $a_{cdm}(443)$ and C are observed across the Gulf Stream. Near the coast, values of $a_{cdm}(443)$ and C, respectively, are more than 100 and 10 times greater than values found within the Sargasso Sea. The front for $a_{cdm}(443)$ found across the Gulf Stream is particularly strong. Retrievals of $a_{cdm}(443)$ are especially high near known river outflows as is expected (Hoge *et al.*, 1995; Vodacek *et al.*, 1997). Series of mesoscale meander and ring features as well as many smaller, sub-mesoscale features are also observed on either side of the Gulf Stream in both $a_{cdm}(443)$ and C. High values of C (> 1.5 mg m^{-3}) are found associated with Georges Bank while retrievals of $a_{cdm}(443)$ there do not increase as intensely.

Contrasting this, values of $b_{bp}(443)$ show considerably weaker patterns associated with the Gulf Stream and its associated features (Figure 3). High values of $b_{bp}(443)$ are associated with enclosed, semi-enclosed and near-shore waters, particularly for locations where intense values of $a_{cdm}(443)$ and C are found, such as Georges Bank. Ocean variations in the value of $b_{bp}(443)$ are relatively small, typically a factor of 2-3 across the Gulf Stream.

CDM Validation using Airborne Lidar

Superimposed on the image of $a_{cdm}(443)$ are three tracks flown by the Airborne Oceanographic Lidar (AOL) on the same day, providing an independent estimate of surface ocean optical properties. Laser-induced fluorescence returns from the AOL can be used to derive the absorption coefficient at 355 nm, $a_{CDOM}(355)$, of chromophoric dissolved organic matter (CDOM) – the dissolved component of CDM (e.g., Hoge, *et al.* 1995). This technique is based upon an empirical relationship between the fluorescence of CDOM, excited by a laser operating at 355 nm, and the absorption coefficient of CDOM at 355 nm (Hoge *et al.*, 1993). Because the SOA retrieves $a_{cdm}(443)$, to compare the two we must either convert the retrieved value to that at 355 nm or the AOL value to 443 nm. We chose the latter.

The AOL-determined value of $a_{cdm}(443)$ is derived from its measurement of $a_{CDOM}(355)$ through multiplication by the factor, $\exp(-S(443-355))$. Using the value of S from GSM01 ($S = 0.0206$ nm^{-1}), Figure 4a compares the SOA-retrieved $a_{cdm}(443)$ with the AOL-retrieved dissolved component $a_{CDOM}(443)$ from the north–south AOL transect shown in Figure 1. We see that there is excellent agreement between the two estimates in and south of the Gulf Stream. Even the small-scale variations in the AOL measurements of $a_{CDOM}(443)$ are captured by the SOA retrievals. However, this agreement is degraded to the north where the SOA values are always larger than the AOL. Besides the possibility of measurement/algorithm error, there may be two physical reasons for the disagreement. First, across the entire transect a single value for S (0.0206 nm^{-1}) was used to convert the AOL-retrieved dissolved component at 335 nm to 443 nm. Such a value

may be characteristic of oligotrophic waters of the Gulf Stream; however coastal waters with significant terrestrial exchanges are characterized by lower *S* values for the CDOM spectrum (e.g., Green and Blough, 1994; Blough and DelVecchio, 2002). Second, the SOA retrieves the absorption of *both* the dissolved and suspended detrital components, while the AOL retrieves just the dissolved component. Therefore in the absence of measurement or model error, the AOL estimate should always be smaller than the SOA retrieval. However for most oceanic environments, detrital particulates make only small contributions to the $a_{cdm}(443)$ signal (Siegel *et al.*, 2002). An extensive data set of spectrophotometric absorption measurements from the Gulf of Maine and Georges Bank show $a_{dp}(443)$ to be 17.2% (s.d. = 12.9%, N=403) of the observed $a_{cdm}(443)$ value (Siegel *et al.*, manuscript in progress). Field observations from the shelf regions around Florida and the Bahamas islands indicate that detrital particles only contribute 12.4% of the $a_{cdm}(443)$ value (s.d. = 9.0%, N=272). Thus, $a_{dp}(443) << a_{CDOM}(443)$, so $a_{cdm}(443) \approx a_{CDOM}(443)$.

It is interesting to determine the value of *S* required to bring the SOA retrieved $a_{cdm}(443)$ into confluence with the AOL-retrieved $a_{CDOM}(443)$ at each point along the track (Figure 4b). The resulting *S* values show a clear trend of decreasing into the mesotrophic waters as would be expected (Green and Blough, 1994). Similar results are found for the other two tracks.

Assuming that $a_{CDOM}(443)$ is the major component of the satellite-retrieved $a_{cdm}(443)$, these comparisons suggest that the SOA is performing well in retrieving $a_{cdm}(443)$ from

the SeaWIFS imagery. The spatial patterns of their variation are well matched, and there is reasonable quantitative agreement. Differences in the two are readily explained by differences in the *S* value associated with the CDOM source. This result also suggests that indices for land-ocean interaction can be developed from retrievals of the *S* value with a new generation of ocean color sensors, e.g., equipped with spectral bands in the UV.

Chlorophyll Validation using SeaWIFS Operational Products

To examine the quality of the chlorophyll *a* retrieval we compared it to the standard SeaWiFS product (STD). The SeaWiFS data have been validated (Hooker and McClain, 2000) and we take them to be surface truth for the comparison. We used the SeaWiFS 8-day mean (days 273-280) covering the image we examined (day 279). The chlorophyll *a* composite image is presented in Figure 5. Figure 6 compares the 8-day mean with the SOA-retrieved values of *C* along the two lines drawn on Figure 5. There is close agreement between the mean STD processing for the 8-day period and the SOA for day 279, suggesting that the SOA also performs well in retrieving *C*.

Figure 6 also suggests a difficulty with the SOA algorithm for regions characterized by large values of $a_{cdm}(443)$, e.g., greater than about 0.05-0.10 m^{-1}. For these regions, the SOA algorithm often gives $C \approx 0.7$ mg/m^3. In our operation of the optimization algorithm, we use four sets of starting values for the five parameters. Optimization proceeds with each and after ten iterations, the starting point that produced the smallest

residual is allowed to continue until the convergence criteria are meant, or until further iterations are deemed to result in little gain. The chlorophyll *a* value for two of the starting points is 0.7 mg/m^3. Thus, it appears that for high $a_{cdm}(443)$ environments the SOA gets "stuck" near its starting point. We are trying to find a way to circumvent this behavior; however, it may be that for high-$a_{cdm}(443)$ and high-*C* regions it is not possible to estimate *C* accurately using the present SOA procedure, because ρ_w in the blue becomes too small.

Aerosol Parameters

Retrieved values of the aerosol single scattering albedo (ω_0) are seen to be nearly unity over most of the image (Figure 7). This contrasts the previous Chomko and Gordon (2001) application of the SOA procedure where retrieved ω_0 values were unity (non-absorbing aerosol) over the low-*C* areas south of the Gulf Stream and ~ 0.95 in the higher-*C* regions. The difference here is the use of the GSM01 vs. the Gordon *et al*. (1988) reflectance model. Values of ω_0 are far from unity only very close to the coast (Figure 7). There the water-leaving reflectance in the NIR is not negligible (Case 2 waters; Gordon and Morel, 1983; Siegel et al. 2000). This suggests that the SOA has achieved its goal of a nearly complete decoupling of $\rho_A(\lambda)$ and $\rho_w(\lambda)$. As mentioned earlier, in the Chomko and Gordon (2001) application it was found that when the SOA was applied to imagery for which the aerosol concentration was very low $\rho_A(\lambda)$ and $\rho_w(\lambda)$ did not totally decouple as evidenced by the presence of strong oceanic patterns in ω_0. In Figure 8, we present the image of ω_0 retrieved for Middle Atlantic Bight from SeaWiFS

imagery acquired on day 281 of 1997. Day 281 of 1997 was the very clear day examined in Chomko and Gordon (2001). Figure 8 shows ω_0 ~ unity over the whole region, with only a faint suggestion of oceanic features, except in the coastal regions. In contrast, the inserted image, which is processed by replacing the GSM01 reflectance model with the *Gordon et al.* (1988) reflectance model, clearly shows oceanic features north of the Gulf Stream. This failure to decouple $\rho_A(\lambda)$ and $\rho_w(\lambda)$ in the inserted image is due to the incomplete nature of the Gordon *et al*. (1988) model for $\rho_w(\lambda)$. In the present application (using GSM01), lowering $\rho_w(412)$ relative to $\rho_w(443)$ can be achieved by either increasing $a_{cdm}(443)$ or m_i. When using *Gordon et al.* (1988) this is possible *only* by increasing m_i (which decreases ω_0). We note that even with GSM01 there are still coastal regions (including Georges Bank) where low values of ω_0 are retrieved. These are in Case 2 waters for which the GSM01 parameters (e.g., S, $a_{ph}^*(\lambda)$, and/or n) are not properly optimized.

Concluding Remarks

We have applied the SOA to SeaWiFS imagery using a more complete model to provide $\rho_w(\lambda)$ for the optimization procedure. Validation with airborne (AOL) and space borne (SeaWiFS) acquired surface "truth," and a nearly complete decoupling of $\rho_A(\lambda)$ and $\rho_w(\lambda)$ suggests that the algorithm is a useful alternative to processing ocean color imagery. It should have wide applicability in that it works well in the presence of non-absorbing aerosols and has the potential to provide accurate retrievals in cases where the aerosol is strongly absorbing, e.g., urban pollution. However, the present coupled

algorithm will not work well for mineral dust aerosols because of the assumed wavelength-independent refractive index.

More importantly, the extension of the algorithm to Case 2 waters is immediate. The principal difficulty in Case 2 waters is that one can no longer assume $\rho_w \approx 0$ in the NIR (e.g., Ruddick et al. 2000; Siegel et al. 2000). Thus, direct application of the algorithm in its present form would yield incorrect results for $\nu(m_r,m_i)$ and $\tau_a(m_r,m_i)$. However, given a bio-optical model for $\rho_w(\lambda)$ tuned to the particular Case 2 waters of interest (needed to interpret $\rho_w(\lambda)$ anyway) that extends into the NIR, one can perform an additional iteration to improve $\nu(m_r,m_i)$ and $\tau_a(m_r,m_i)$ in the following manner. First apply the SOA with $\rho_w = 0$ in the NIR and find values for all of the parameters. Next use the water parameters to predict ρ_w in the NIR and remove its contribution to $\rho_t - \rho_r$ in the NIR. Operate the ν-τ_a portion of the algorithm to obtain a better estimate for $\nu(m_r,m_i)$ and $\tau_a(m_r,m_i)$. Finally, operate the visible portion of the optimization to obtain improved water parameters, etc. Although such an approach is computationally intensive, Case 2 water regions for which a particular bio-optical algorithm would be applicable are usually not spatially large, so intense computation is not an obstacle to processing Case 2 water regions. Such an extension is not effected here because the GSM01 model is not (yet) tuned for turbid Case 2 waters.

References

Andre, J.-M., and A. Morel, Atmospheric Corrections and Interpretation of Marine Radiances in CZCS Imagery, Revisited, *Oceanologica Acta*, **14**, 3—22 (1991).

Blough, N.V., and R. Del Vecchio, Chromophoric DOM in the coastal environment. *Biogeochemistry of Marine Dissolved Organic Matter*, D.A. Hansell and C.A. Carlson, eds., Academic Press, p. 509—546 (2002).

Bricaud, A., and A. Morel, Atmospheric Corrections and Interpretation of Marine Radiances in CZCS Imagery: Use of a Reflectance Model, *Oceanologica Acta*, **7**, 33—50 (1987)

Carder, K.L. F.R. Chen, Z.P. Lee, S.K. Haws, D. Kamykowski, Semianalytic Moderate Resolution Imaging Spectrometer algorithms for chlorophyll a and absorption with bio-optical domains based on nitrate-depletion temperatures, *Jour. Geophys. Res.*, **104C**, 5403—5421 (1999).

Chomko, R.M., and H.R. Gordon, Atmospheric correction of ocean color imagery: Use of the Junge power-law aerosol size distribution with variable refractive index to handle aerosol absorption, *Applied Optics* **37**, 5560-5572 (1998).

Chomko, R.M. and H.R. Gordon, Atmospheric correction of ocean color imagery: Test of the spectral optimization algorithm with SeaWiFS, *Applied Optics*, **40**, 2973 — 2984 (2001).

Degrandpre M.D., A. Vodacek, R.K. Nelson, E.J. Bruce, N.V. Blough, Seasonal seawater optical properties of the US Middle Atlantic Bight. *Jour. Geophys. Res.*, **101C**, 22727-22736 (1996).

Gordon, H.R., D.K. Clark, J.L. Mueller, and W.A. Hovis, Phytoplankton Pigments Derived from the Nimbus-7 CZCS: Initial Comparisons with Surface Measurements, *Science*, **210**, 63—66 (1980).

Gordon, H.R. and A.Y. Morel, *Remote Assessment of Ocean Color for Interpretation of Satellite Visible Imagery: A Review*, Springer-Verlag, New York (1983) 114 pp.

Gordon, H.R., O.B. Brown, R.E. Evans, J.W. Brown, R.C. Smith, K.S. Baker, and D.K. Clark, A Semi-Analytic Radiance Model of Ocean Color, *Jour. Geophys. Res.*, **93D**, 10909-10924 (1988).

Gordon, H.R., T. Du, and T. Zhang, Remote sensing ocean color and aerosol properties: resolving the issue of aerosol absorption, *Applied Optics*, **36**, 8670-8684 (1997).

Garver, S., and D. Siegel, Inherent optical property inversion of ocean color spectra and its biogeochemical interpretation: 1 time series from the Sargasso Sea, *Geophys. Res.*, **102C**, 18607—18625 (1997).

Green, S.A., N.V. Blough, Optical absorption and fluorescence properties of chromophoric dissolved organic matter in natural waters. *Limnol. Oceanogr.*, **39**, 1903-

1916 (1994).

Hoge, F.E. and P.E. Lyon, Satellite retrieval of inherent optical properties by linear matrix inversion of oceanic radiance models - an analysis of model and radiance measurement errors. *Jour. Geophys. Res.*, **101C**, 16631—16648 (1996).

Hoge, F.E., A. Vodacek, R.N. Swift, J.K. Yungel, and N.V. Blough, Inherent optical properties of the ocean: retrieval of the absorption coefficient of chromophoric dissolved organic matter from airborne laser spectral fluorescence measurements, *Applied Optics*, **34**, 7032—7038 (1995).

Hoge, F.E., A. Vodacek, and N.V. Blough, Inherent optical properties of the ocean: retrieval of the absorption coefficient of chromophoric dissolved organic matter from fluorescence measurements, *Limnology and Oceanography*, **38**, 1394—1402 (1993).

Hooker, S.B., W.E. Esaias, G.C. Feldman, W.W. Gregg, and C.R. McClain, An Overview of SeaWiFS and Ocean Color, SeaWiFS Technical Report Series: Volume 1, S.B. Hooker and E.R. Firestone (Ed.), NASA, Greenbelt, MD, Technical Memorandum 104566, July 1992.

Hooker, S.B., and C.R. McClain, The calibration and validation of SeaWiFS data, *Progress in Oceanography*, **45**, 427—465, (2000).

Hovis, W.A., D.K. Clark, F. Anderson, R.W. Austin, W.H. Wilson, E.T. Baker D. Ball, H.R. Gordon, J.L. Mueller, S.Y. El Sayed, B. Sturm, R.C. Wrigely, and C.S. Yentsch, Nimbus-7 Coastal Zone Color Scanner: System Description and Initial Imagery, *Science*, **210**, 60—63 (1980).

Lee Z.P., K.L. Carder, S.K. Hawes, R.G. Steward, T.G. Peacock and C.O. Davis, Model for the interpretation of hyperspectral remote-sensing reflectance. *Applied Optics*, **33**, 5721-5732 (1994).

Maritorena, S., D.A. Siegel and A.R. Peterson, Optimization of semi-analytical ocean color model for global scale applications, *Applied Optics* **41**, 2705 — 2714 (2002).

Moulin,C., H.R. Gordon, R.M. Chomko, V.F. Banzon, and R.H. Evans, Atmospheric correction of ocean color imagery through thick layers of Saharan dust, *Geophys. Res. Lett.*, **28**, 5—8 (2001a).

Moulin,C., H.R. Gordon, V.F. Banzon, and R.H. Evans, Assessment of Saharan dust absorption in the visible from SeaWiFS imagery, *Jour. Geophys. Res.*, **106D**, 18239—18249 (2001b).

O'Reilly, J.E., S. Maritorena, B.G. Mitchell, D.A. Siegel, K.L. Carder, S.A. Garver, M. Kahru, C. McClain, Ocean color chlorophyll algorithms for SeaWiFS, *Jour. Geophys. Res.*, **103C**, 24937−24953 (1998).

Roesler, C.S., and M.J. Perry, in situ phytoplankton absorption, fluorescence emission, and particulate backscattering spectra determined from reflectance. *J. Geophys. Res.*, **100**, 13279–13294 (1995).

Ruddick, K.G.; F. Ovidio and M. Rijkeboer, Atmospheric correction of SeaWiFS imagery for turbid coastal and inland waters. *Applied Optics*, **39**, 897—912 (2000).

Siegel, D.A., M. Wang, S. Maritorena and W. Robinson, Atmospheric correction of satellite ocean color imagery: The black pixel assumption. *Applied Optics*, **39**, 3582–2591 (2000).

Siegel, D.A., S. Maritorena, N. B. Nelson, D.A. Hansell and M. Lorenzi-Kayser, 2001: Global ocean distribution of colored dissolved and detrital materials. In press *Journal of Geophysical Research*.

Smith, R.C, and W.H. Wilson, Ship and satellite bio-optical research in the California Bight, in *Oceanography from Space*, ed. J.F.R. Gower, Plenum, New York (1981) p. 281—294.

Vodacek, A., Blough, N.V., DeGrandpre, M.D., Peltzer, E.T. & Nelson, R.K. Seasonal variation of CDOM and DOC in the Middle Atlantic Bight: Terrestrial inputs and photooxidation. *Limnol. Oceanogr.* 42, 674–686 (1997).

Yang, H. and H.R. Gordon, Remote sensing of ocean color: Assessment of the water-leaving radiance bidirectional effects on the atmospheric diffuse transmittance, *Applied Optics*, **36**, 7887–7897 (1997).

Figure Captions

Figure 1: $a_{cdm}(443)$ retrieved from the SeaWiFS image for Day 279 of 1997 in the Middle Atlantic Bight. "Surface truth" data were obtained with the AOL along the white lines off the coast between the Chesapeake Bay and Delaware Bay. The Color scale is logarithmic (labels are 0.003, 0.010, 0.030, 0.100, 0.300, and 0.500 m^{-1}).

Figure 2: *C* retrieved from SeaWiFS for the same image as Figure 1. The Color scale is logarithmic (labels are 0.05, 0.10, 0.30, 0.50, 1.00, and 1.50 mg m^{-3}).

Figure 3: $b_{bp}(443)$ retrieved from SeaWiFS for the same image as Figure 1. The Color scale is logarithmic (labels are 0.0003, 0.0010, 0.0030, 0.0100, and 0.0300 m^{-1}).

Figure 4a. $a_{cdm}(443)$ derived from the AOL and the SOA along the north-south AOL flight line on Figure 1

Figure 4b. Value of *S* required to bring the AOL-retrieved $a_{CDOM}(443)$ into agreement with the SOA-retrieved $a_{cdm}(443)$ for the north-south track on Figure 1.

Figure 5. SeaWiFS 8-day mean *C* for days 273-280 1997. Extractions in Figure 6 are along the red lines on the figure.

Figure 6. Comparison between the SeaWiFS standard 8-day *C* (STD) and that derived by the SOA. Data are extracted along the lines in Figure 5: (a) North-South line; (b) East-West line.

Figure 7. Retrieved ω_0 for day 279.

Figure 8. Retrieved ω_0 for day 281. Full image uses the methodology described in the text. Inserted image is also the retrieved ω_0, but with GSM01 ρ_w model replaced by the *Gordon et al.* [1988] ρ_w model. Note that the inserted image retrieves lower ω_0 values and shows obvious oceanic structure in ω_0 in the slope and shelf waters. This indicates there is incorrect atmospheric correction in these regions. In contrast, oceanic features are nearly absent from the full image, indicating a better decoupling between the oceanic and atmospheric reflectances. (Color bar labels are 0.6, 0.7, 0.8, 0.9, 1.0.)

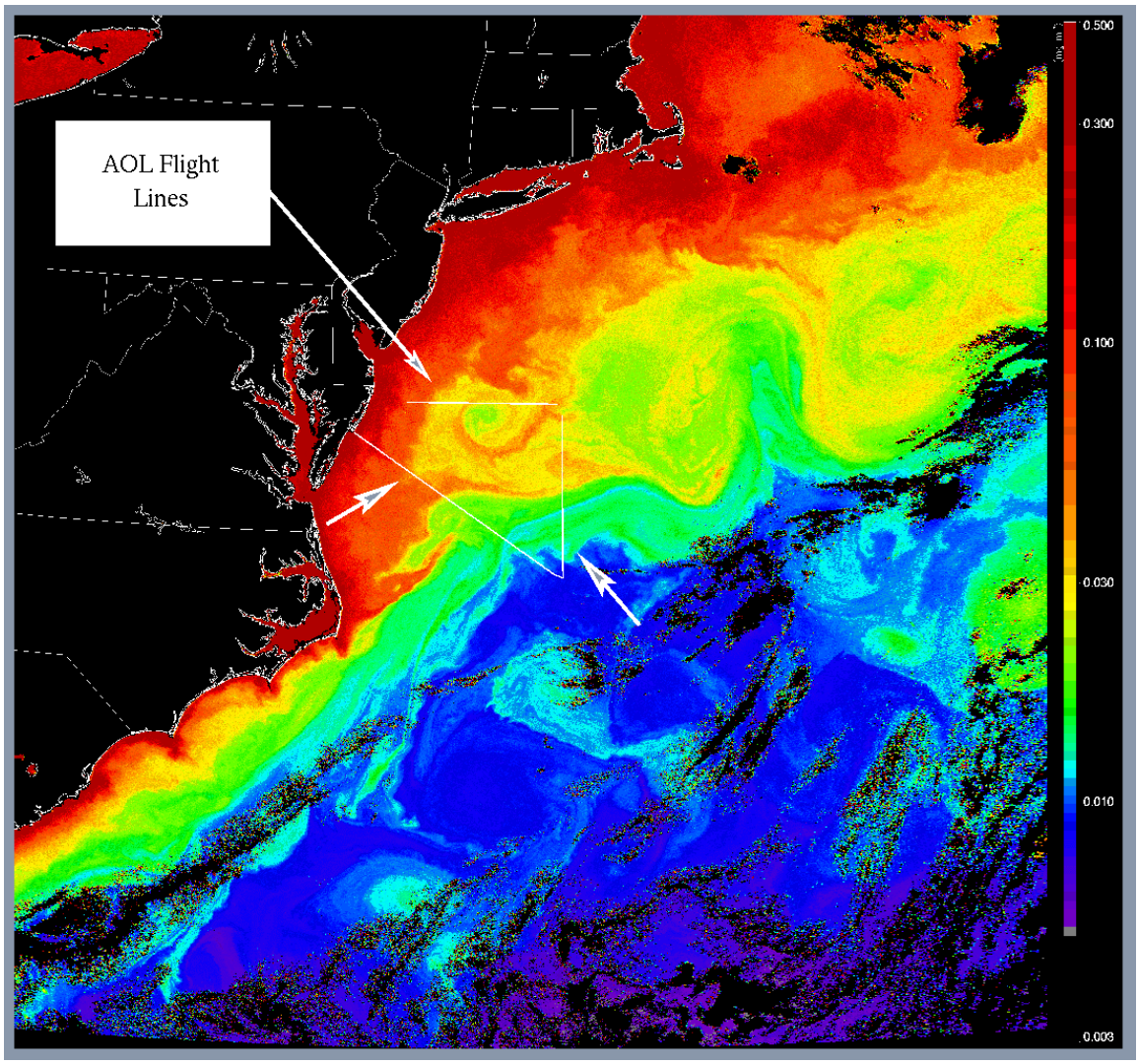

Figure 1: $a_{cdm}(443)$ retrieved from the SeaWiFS image for Day 279 of 1997 in the Middle Atlantic Bight. "Surface truth" data were obtained with the AOL along the white lines off the coast between the Chesapeake Bay and Delaware Bay. The Color scale is logarithmic (labels are 0.003, 0.010, 0.030, 0.100, 0.300, and 0.500 m^{-1}).

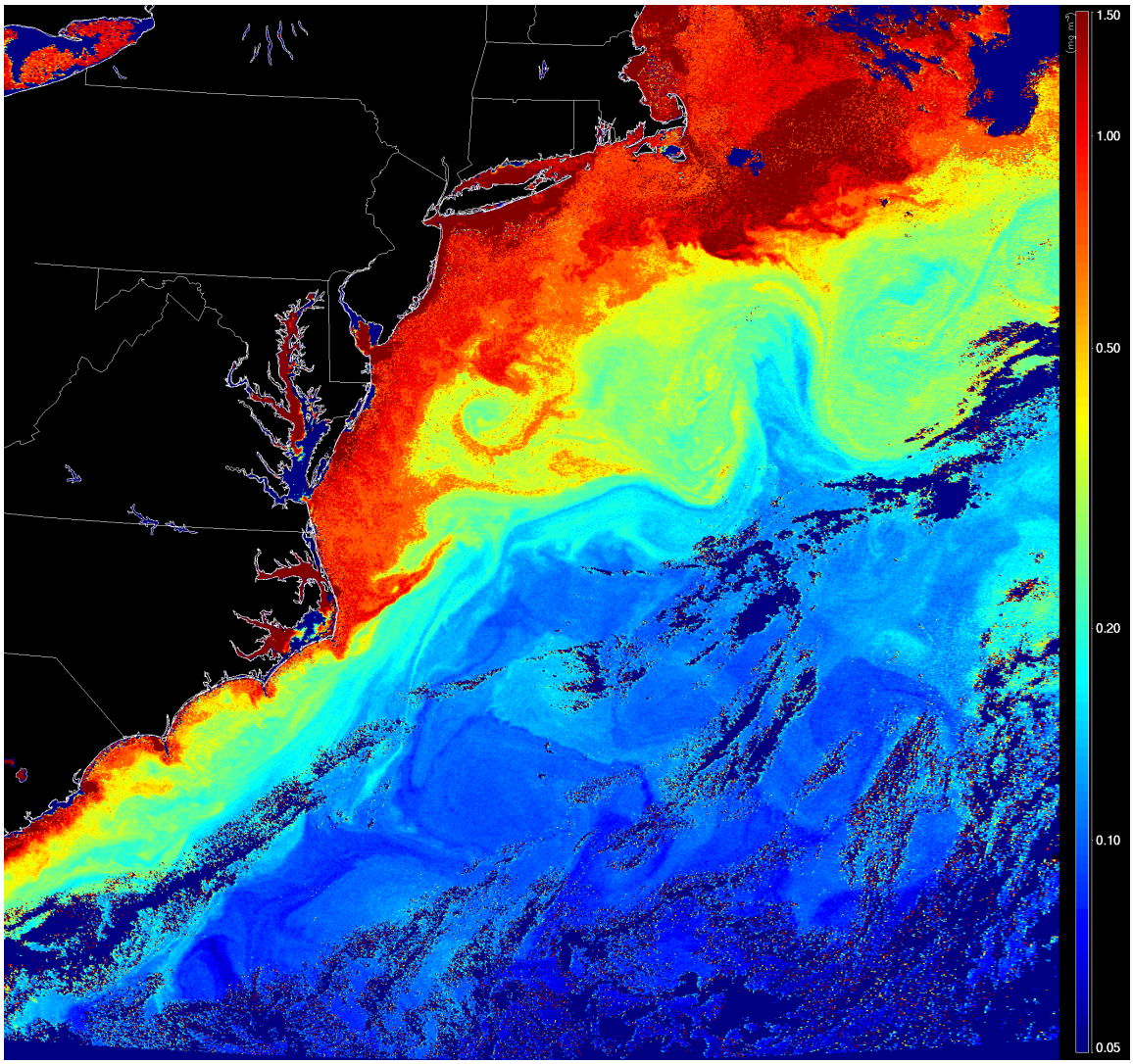

Figure 2: *C* retrieved from SeaWiFS for the same image as Figure 1. The Color scale is logarithmic (labels are 0.05, 0.10, 0.30, 0.50, 1.00, and 1.50 mg m^{-3}).

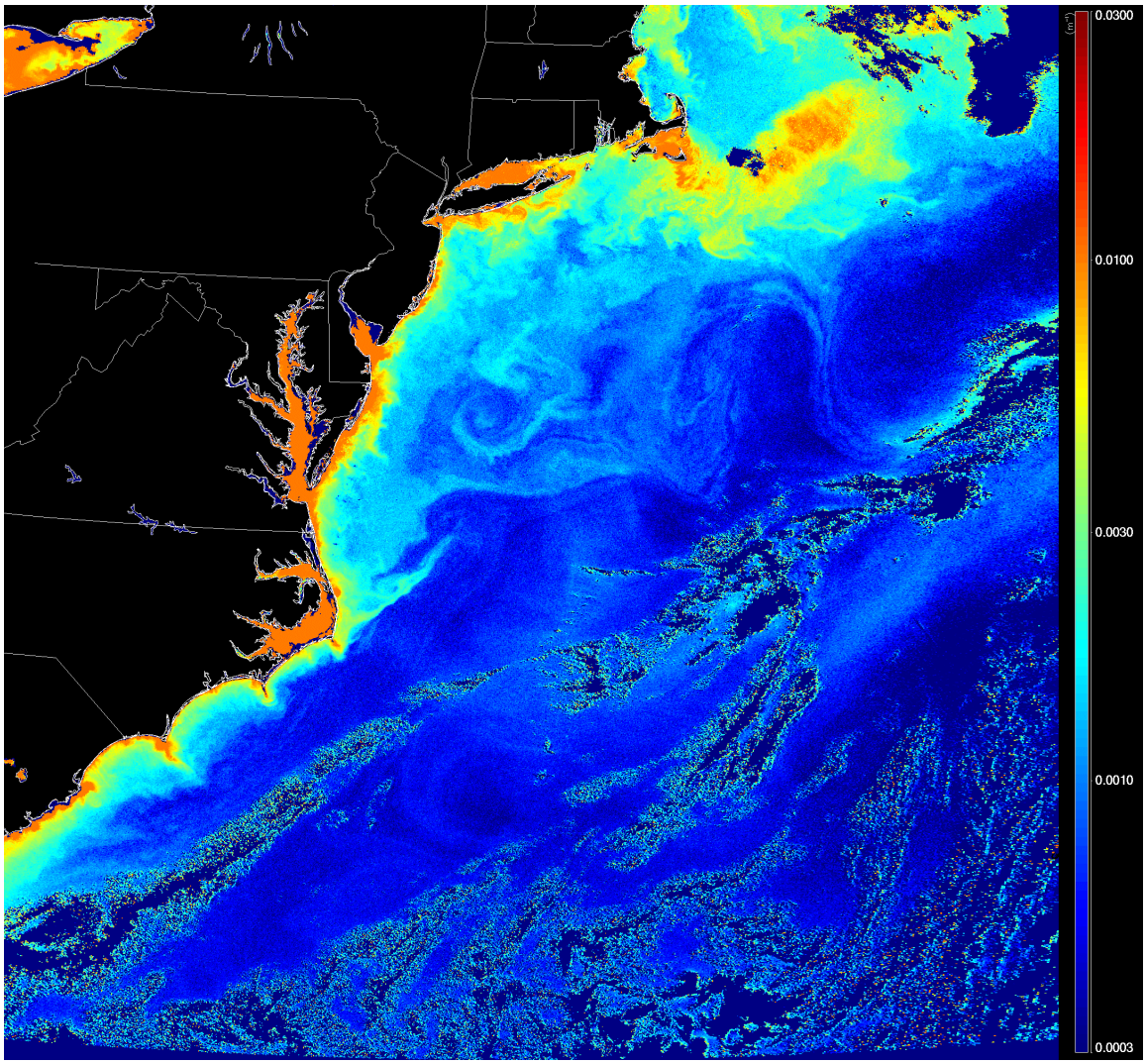

Figure 3: $b_{bp}(443)$ retrieved from SeaWiFS for the same image as Figure 1. The Color scale is logarithmic (labels are 0.0003, 0.0010, 0.0030, 0.0100, and 0.0300 m^{-1}).

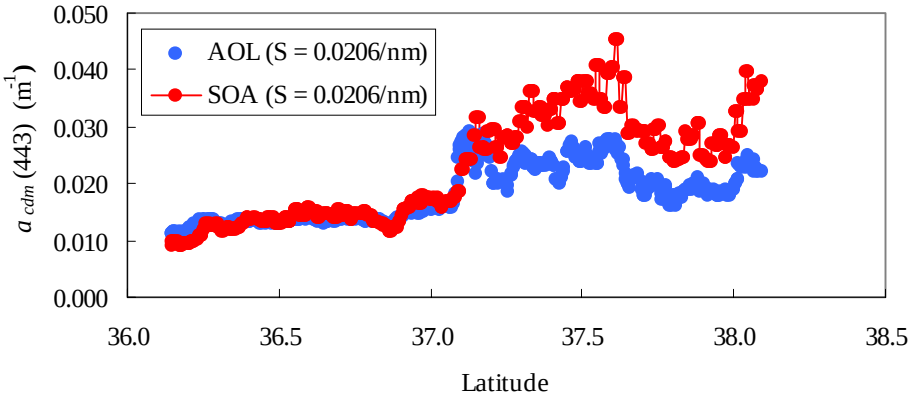

Figure 4a. $a_{cdm}(443)$ derived from the AOL and the SOA along the north-south AOL flight line on Figure 1.

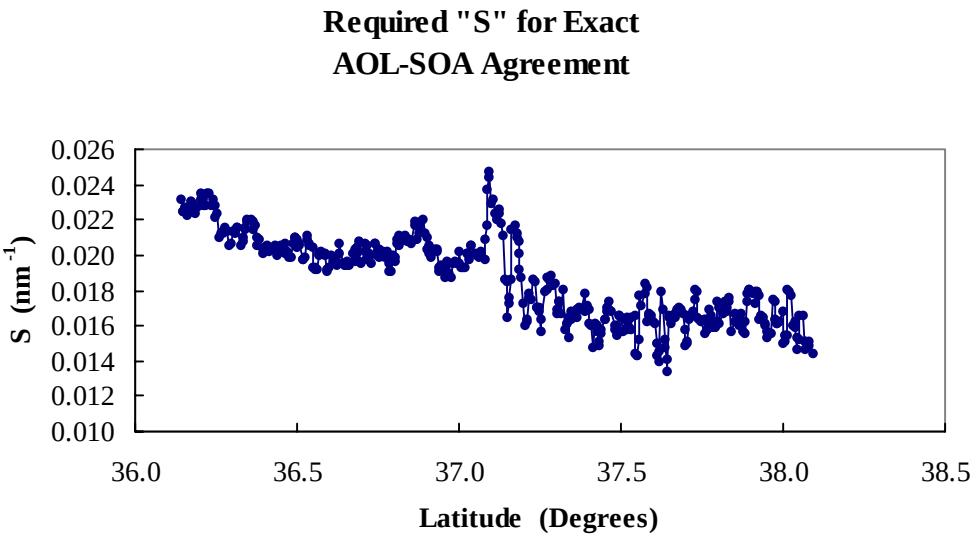

Figure 4b. Value of *S* required to bring the AOL-retrieved $a_{CDOM}(443)$ into agreement with the SOA-retrieved $a_{cdm}(443)$ for the north-south track on Figure 1.

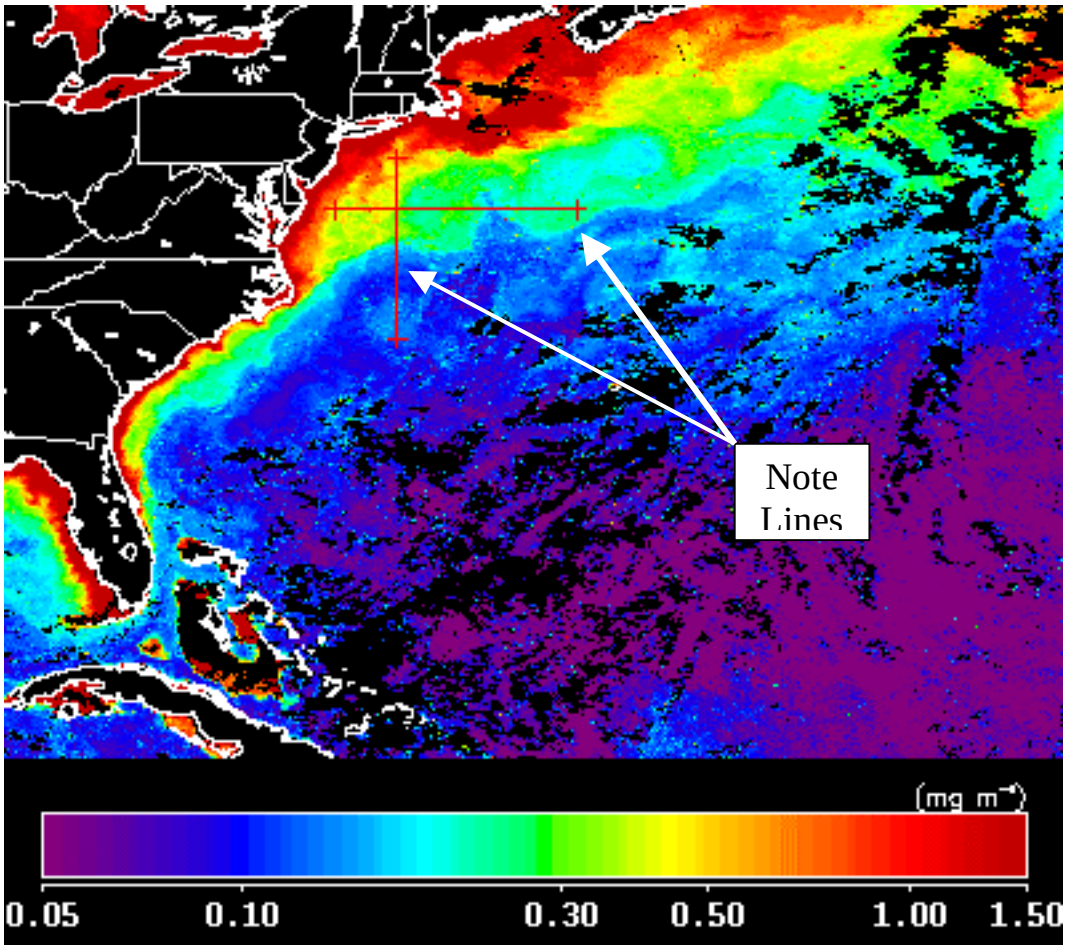

Figure 5. SeaWiFS 8-day mean *C* for days 273-280 1997.
Extractions in Figure 6 are along the red lines on the figure.

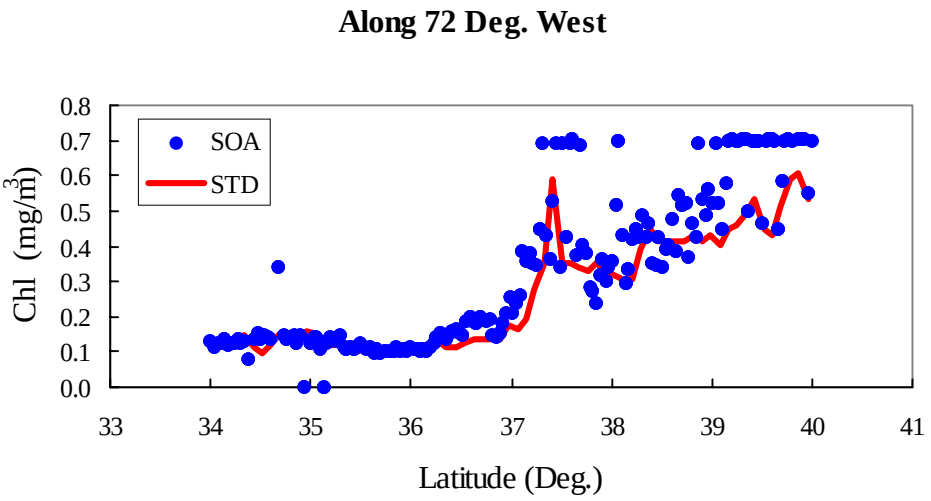

(a)

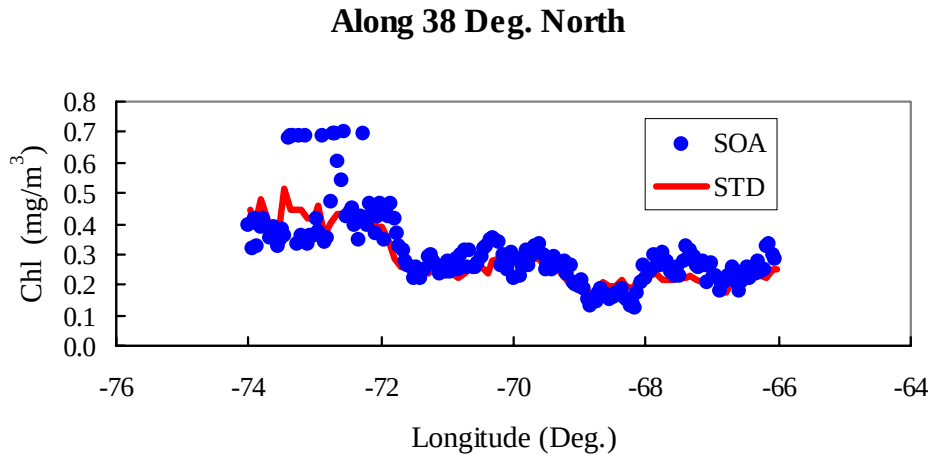

(b)

Figure 6. Comparison between the SeaWiFS standard 8-day *C* (STD) and that derived by the SOA. Data are extracted along the lines in Figure 5: (a) North-South line; (b) East-West line.

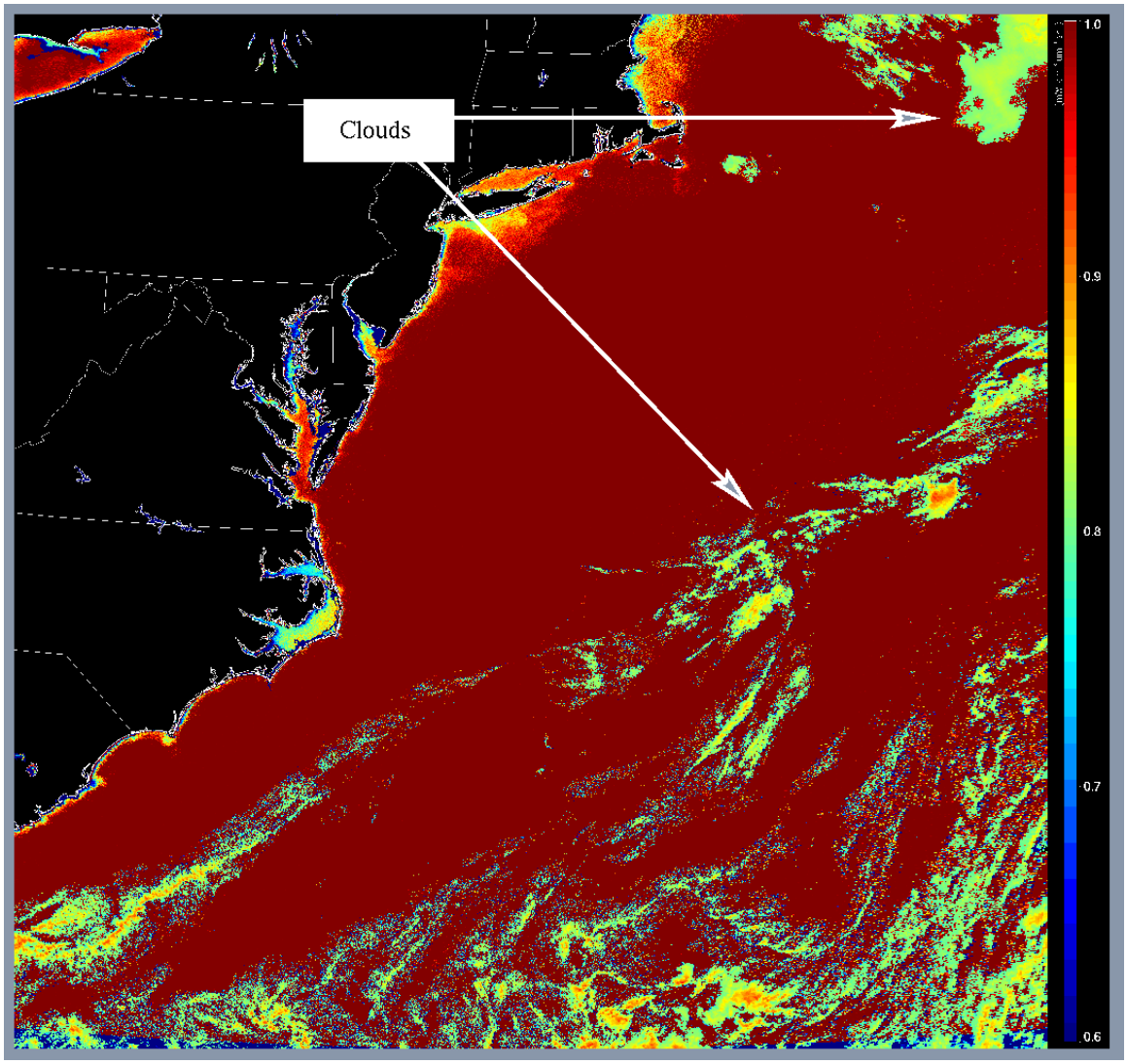

Figure 7. Retrieved ω_0 for day 279.

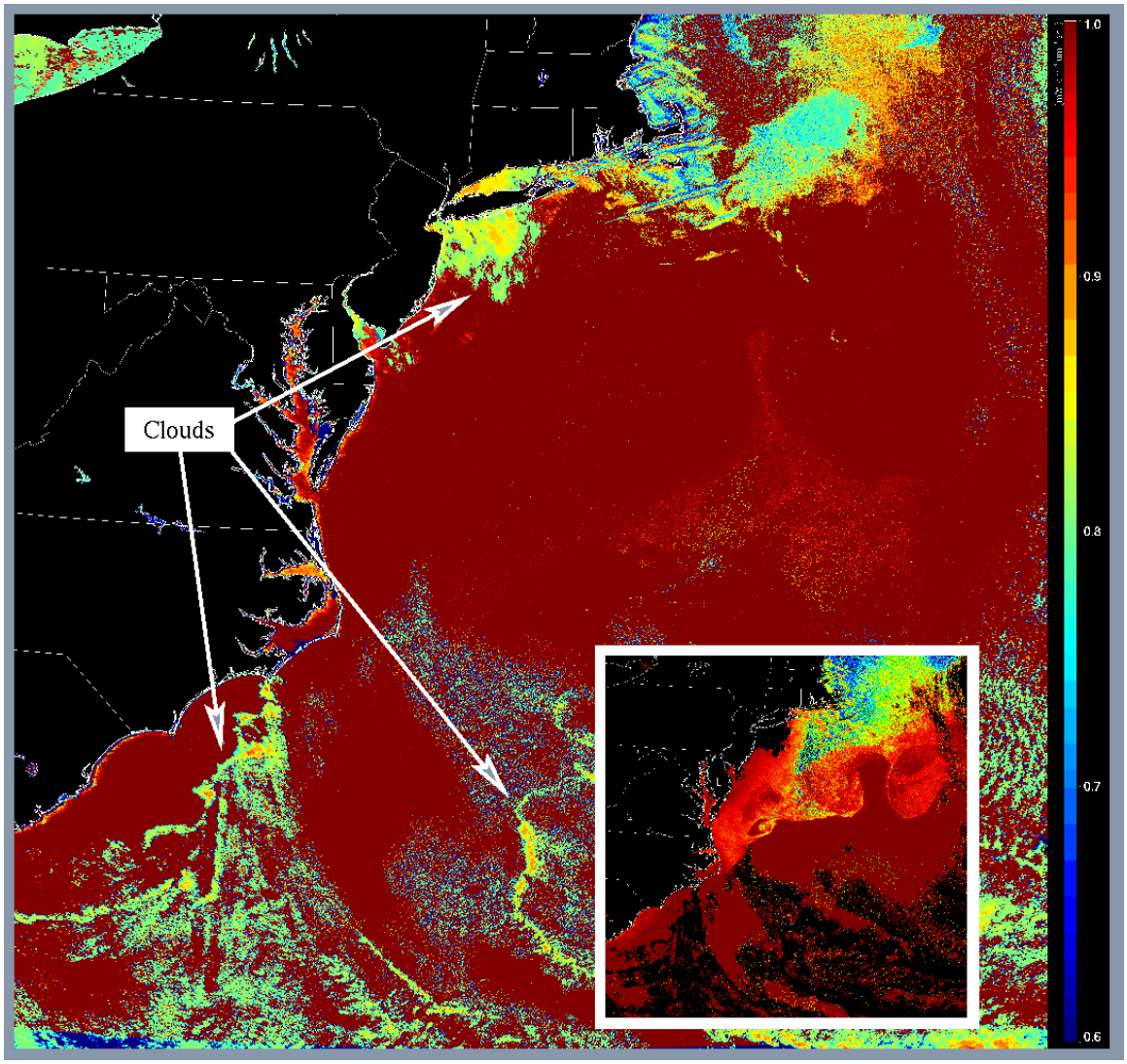

Figure 8. Retrieved ω_0 for day 281. Full image uses the methodology described in the text. Inserted image is also the retrieved ω_0, but with GSM01 ρ_w model replaced by the *Gordon et al.* [1988] ρ_w model. Note that the inserted image retrieves lower ω_0 values and shows obvious oceanic structure in ω_0 in the slope and shelf waters. This indicates there is incorrect atmospheric correction in these regions. In contrast, oceanic features are nearly absent from the full image, indicating a better decoupling between the oceanic and atmospheric reflectances. The differences between the insert and Figure 8 of Chomko and Gordon (2001) are due to the two different methods of retrieving ν and τ_a. (Color bar labels are 0.6, 0.7, 0.8, 0.9, 1.0.)

APPENDIX II

Solar Zenith Angle Equals Zero Cruise
May 2002

K.J. Voss

Solar Zenith Angle = Zero cruise, May 2002

Cruise report: Initial Data summary

Kenneth Voss

July 11, 2002

Note: while this report was written by myself, this is the summary of work performed by myself and Dennis Clark and his group at NOAA/NESDIS. Other than the NuRADS data, all other data was contributed by the NOAA/NESDIS group.

Introduction

This is a brief summary of the data collected during the Solar Zenith Angle Zero cruise in May 2002. The objective of this cruise was to obtain the spectral radiance distribution, with the new NuRADS camera system over a wide range of solar zenith angles. Along with the radiance distribution, ancillary data was collected documenting the sky, water, and meteorological conditions to help interpret the radiance distribution data. This report will discuss very preliminary information on the radiance distribution and present a summary of the ancillary data acquired during the cruise. The calibrations on the NuRADS system have just been concluded we have reduced the data to calibrated radiance distribution images. We are beginning to investigate the applications of this data set.

Presently MOBY is the primary calibration point for the ocean color community, including SeaWiFS and MODIS. In general the radiance at nadir is used to provide the water leaving radiance, which is then compared with the satellite-derived value for fine adjustments of the satellite calibration. Unfortunately MODIS rarely (and SeaWiFS never) views the MOBY site at nadir, so the variation with viewing geometry, BRDF, effects are ignored. For more accurate use of the MOBY data these BRDF effects must be understood, or modeled. The MOBY site is generally very clear water, but the solar zenith angle and relative view-sun azimuth angles change throughout the year. With a complete set of BRDF data for solar zenith angles experienced throughout the year, an empirical model could be developed to relate the nadir radiance to the specific viewing geometry of the satellite. The goal of this cruise was to get the BRDF over a complete range of solar zenith angles experienced at the MOBY site, in similar (clear) water.

Between May 15th, 2002 and May 22, 2002 we made daily trips on the R/V Klaus Wyrtki, a University of Hawaii vessel. These trips were arranged such that data collection could begin at approximately 60 degree solar zenith angle (approximately 9AM local time), and measurements continued until either the sun set at 60 degrees solar zenith angle or afternoon clouds built up. Predominately at this location clouds increased during the late morning so that few days could continue significantly past early afternoon. On 5 days during this period NuRADS data was collected. The first day, 5/15/02, was a test day. Unfortunately on the second day (5/16/02) the NuRADS instrument did not work well, but in the remaining days the NuRADS instrument collected a set of 6 spectral radiance distribution images every 2 minutes and worked continuously from approximately 9AM until the clouds filled the sky in the afternoon. In addition to this time, other NuRADS data were collected from the R/V K'o K' on May 26th and 27th at the MOBY site after the MOBY buoy had been deployed for its quarterly rotation. The NuRADS data from this latter period will be included in this report, the ancillary data from this period is not available yet so will not be in this report.

NuRADS Calibration:

Some of the NuRADS calibration results will be documented in this report.

Spectral calibration

NuRADS has 6 spectral bands available. The spectral filters are nominally 10nm interference filters, with additional filters in some cases for extra out-of-band blocking, and a BG-18 glass filter installed to reduce the infrared out-of-band response during calibrations. Each filter combination was removed from the instrument and measured, and the Band center and band width (Full Width at Half Maximum) determined. In the configuration used during this cruise the spectral bands were:

Filter number	Band center (nm)	Band width, FWHM(nm)
1	410.5	9.6
2	435.8	10.8
3	486.5	10.8
4	525.7	10
5	615.8	9.8
6	666.1	10.7

Angular calibration

The mapping of the image to the external angular space must be determined. With the fisheye system, behind a dome window, this calibration must be done in water and in air. If the optical system is located correctly (with the first principle plane at the center of the dome curvature) the wet and dry angular calibrations will be the same. On the next page is shown the result of an angular calibration done in air and with the system immersed. Also a fit to the submersed data is shown. As can be seen in the figure, the submersed and dry calibrations are almost identical, indicating that we have the optical system in the correct location (a somewhat difficult to determine specification). The fish eye projection should be a linear relationship between the external zenith angle and radius from the center in the image. We found the relationship to be:

Image angle = 1.9596 (+-0.317) + 0.28257 (+-0.00205) *radius

The important number is the slope of this relationship (0.28257) and here the error in this coefficient is less than 1%.

Rolloff calibration

The rolloff for this camera system works out to be a simple linear function of radius from the center:

Rolloff function = 1+radius*1.579E-4.

This equation works out to 70 degree zenith angle at which time the rolloff gets very large. Since our concern is water leaving radiance, which has a maximum in-water zenith angle of approximately 50 degrees, this function works well for us. Note that the rolloff factor is only a few percent at maximum, making this factor small relative to the rolloff in some of our previous radiance distribution systems.

Immersion calibration

The immersion calibration is important since our absolute calibrations are done in air, but our data is acquired in water. With the radiance distribution system this calibration turns out to be slightly tricky. Because of the curved dome window the normal n^2 (n = index of refraction) effect doesn't appear, however another n^2 effect does appear because the camera aperture changes apparent size due to the curved window and different index of refraction.

To determine this effect an experiment was performed. The instrument is set in an empty container looking upwards at an illuminated calibration plaque. Images of the plaque are obtained, then the container is filled until the water is just covering the camera dome window. Images of the plaque are obtained again. The average of a small area in the center of the plaque is determined for both situations. The ratio of these two cases was found to be: water/dry= 0.9636. When this ratio is included with the expected radiance changes of the plaque due to refraction at the flat air-water interface, and different fresnel reflectance factors in the two cases the immersion factor (factor to multiply the data by to get the true radiance in water) was found to be 1.905.

Absolute calibration

To get the absolute calibration number we took images of a standard calibration plaque illuminated by an absolute irradiance source. The image is processed by the rolloff and a center portion of the plaque is averaged. The radiance of the plaque can be calculated and the average counts and expected radiance can be combined to find the absolute calibration factor (including the above immersion factor). We found that the calibration numbers were:

Filter	Calibration number Counts/(uW cm-2 sr-1 nm-1)
Filter 1	9.995E-6
Filter 2	1.903E-5
Filter 3	9.587E-5
Filter 4	1.989E-4
Filter 5	3.670E-4
Filter 6	1.182E-4

NuRads Data Summary

During this cruise NuRADS was floated away from the ship approximately 75 yards. NuRADS was suspended under a small dark float (approximately 10cm diameter, 40cm long) at a measurement depth of 70 cm. The data/power cable to NuRADS is a slightly positively buoyant cable, which allows it to easily float on/near the surface. The distance from the ship enabled measurement of the upwelling radiance distribution with negligible ship shadow effects. NuRADS was set on an automatic data collection cycle that enabled the 6 spectral images of the radiance distribution, with associated dark images, to be taken in less than 2 minutes. The instrument was cycled to continue this measurement sequence until the sky became too cloudy for measurements, or the solar zenith angle increased above 70 degrees. Predominately the measurements were halted due to clouds because of early afternoon build up of clouds coming off of Oahu.

To get a measure of data quality of the NuRADS images, the central 100x100 pixels were averaged in each image (after subtraction of a dark image). These are plotted vs. solar zenith angle for each filter on a following page. For filters 1-4 the relationship between solar zenith angle and this average, uncalibrated, value is simply related to the cosine of the solar zenith angle (relating the true irradiance falling on the surface) combined with the extra attenuation of the incoming irradiance due to extra atmospheric pathlength as the solar zenith angle increases. This factor can be used to automatically filter bad (because of clouds or instrument malfunction) data from the rest. By looking at 0.85 (for low) and 1.15 (for high) times the center value one can eliminate the data that falls outside this range. For filters 5-6 this relationship doesn't hold as well, and the hypothesis at this point is the center portion has instrument shadow at small solar zenith angles. In any case the lower limit can be decreased to 0.8 for these filters to get rid of truly bad data. When we eliminate bad data by this method, the result is shown in the following table, where for each filter the number of images which pass this quality control filter are shown, along with the failures and the total number of images in each filter. Many of the failures are due to either cloud contamination, or instrument failures (on the first day). On the last two days there were only on the order of one failure per 90 images.

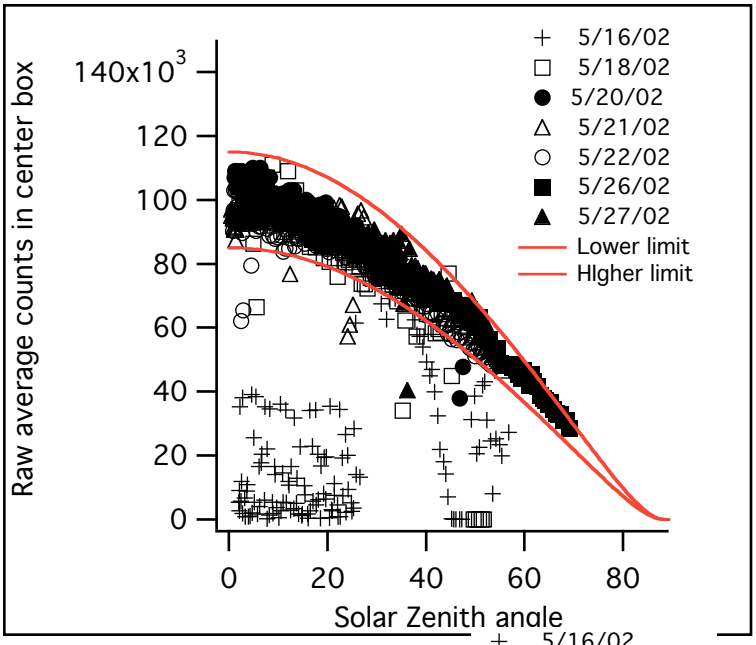
Raw average counts in center box
140x10^3
120
100
80
60
40
20
0
0
20
40
60
80
Solar Zenith angle
5/16/02
5/18/02
5/20/02
5/21/02
5/22/02
5/26/02
5/27/02
Lower limit
HIgher limit

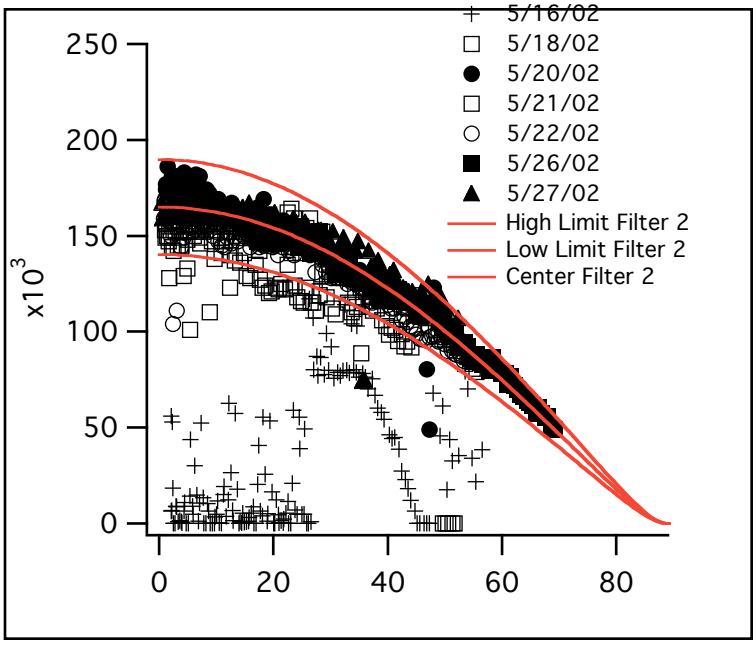
250
200
150
100
50
0
x10^3
0
20
40
60
80
5/16/02
5/18/02
5/20/02
5/21/02
5/22/02
5/26/02
5/27/02
High Limit Filter 2
Low Limit Filter 2
Center Filter 2

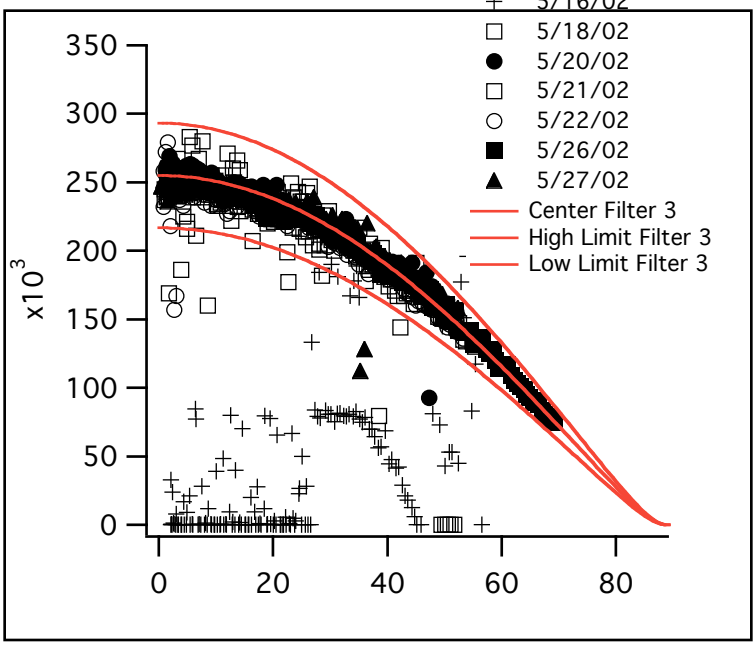
350
300
250
200
150
100
50
0
x10^3
0
20
40
60
80
5/16/02
5/18/02
5/20/02
5/21/02
5/22/02
5/26/02
5/27/02
Center Filter 3
High Limit Filter 3
Low Limit Filter 3

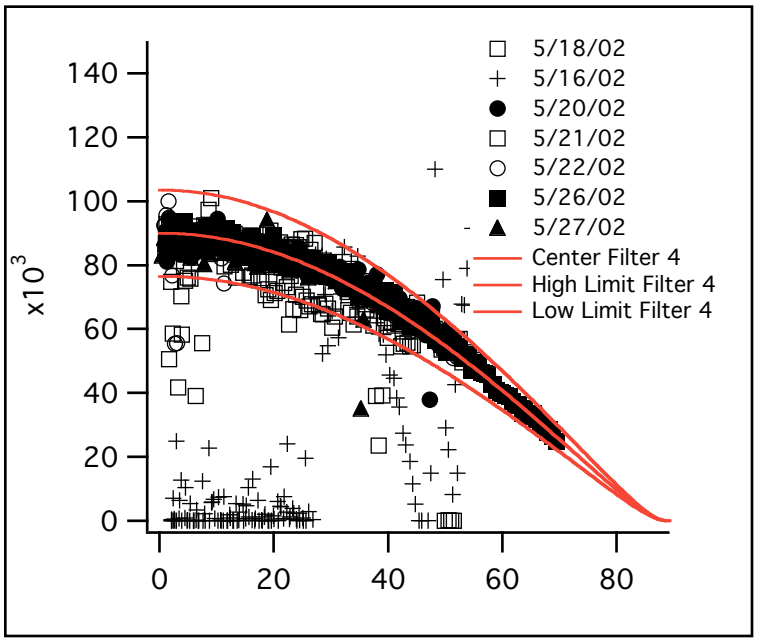
140
120
100
80
60
40
20
0
x10^3
0
20
40
60
80
5/18/02
5/16/02
5/20/02
5/21/02
5/22/02
5/26/02
5/27/02
Center Filter 4
High Limit Filter 4
Low Limit Filter 4

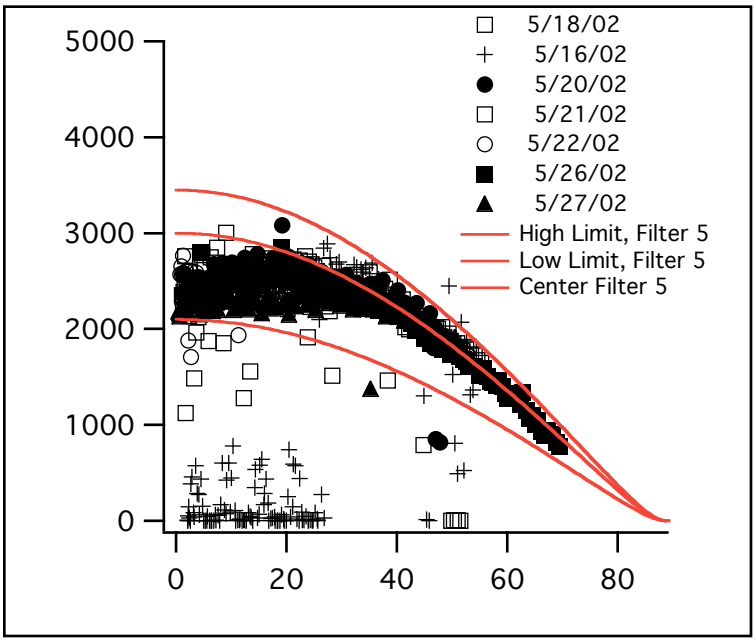
5000
4000
3000
2000
1000
0
0
20
40
60
80
5/18/02
5/16/02
5/20/02
5/21/02
5/22/02
5/26/02
5/27/02
High Limit, Filter 5
Low Limit, Filter 5
Center Filter 5

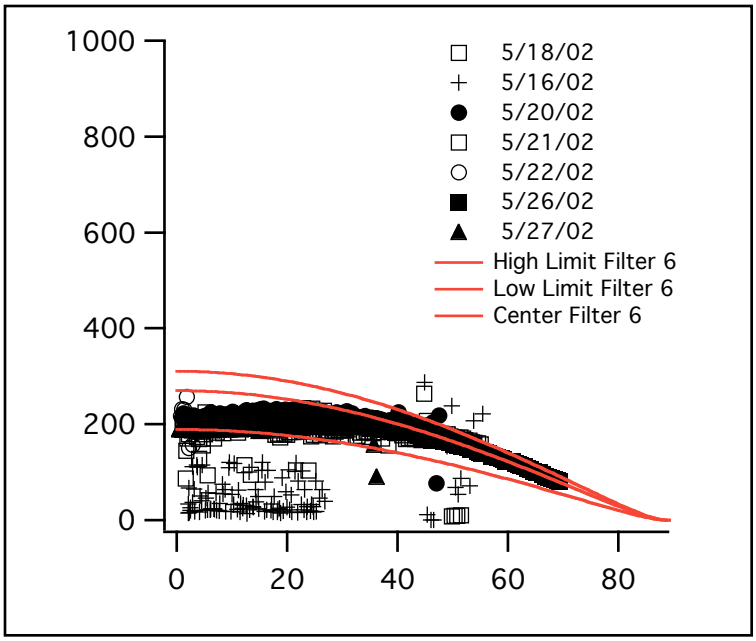
1000
800
600
400
200
0
0
20
40
60
80
5/18/02
5/16/02
5/20/02
5/21/02
5/22/02
5/26/02
5/27/02
High Limit Filter 6
Low Limit Filter 6
Center Filter 6

	Pass	Fail	total
1	668	156	824
2	616	207	823
3	657	165	822
4	659	161	820
5	657	160	817
6	641	172	813
Total	3898	1021	4919

The data has been reduced using the calibration data summarized above. An example radiance distribution is shown on the top of the next page. This radiance distribution was taken at a solar zenith angle of 23 degrees. This was filter 2 (436 nm). The obvious feature in the image is the anti-solar position, from which the sun rays seem to emanate. The line in the image points from the center of the image (nadir) towards the north. The black box is the calculated anti-solar spot, which is slightly different due to small instrument tilt and wave effects. The edge of the image is at nadir angle of 70 degrees, the nadir angle is linearly proportional to radius from the center of the image. The color bar shows the equivalent radiance (in μW cm^{-2} nm^{-1} sr^{-1}).

The lower figure on the next page shows a preliminary example of what we are trying to get from this experiment. This is the correction (Lview/Lnadir) for the Moby site for a satellite view angle of 50 degrees, as a function of solar zenith angle and relative sun-satellite azimuth angle. This example is for Filter 1 (412nm) with only one days data (5/22). This graph shows several effects. First, when the solar zenith angle is near 0 deg., the correction factor is uniformly near 1.04 (or 4%). When the solar zenith angle goes to 50 degrees, the relative azimuth between the sun and satellite view become important, with the maximum correction (over 1.2) occurring when the satellite is viewing near the anti-solar point, and the minimum (0.90) occurring when the satellite is viewing towards the sun (which would actually be completely hidden in the surface glitter pattern). What we will be doing is combining the data from all the days and looking at this result and also looking for spectral variations in this effect.

On the pages following this radiance distribution graph will be the ancillary data collected. Before each set a short description will be provided.

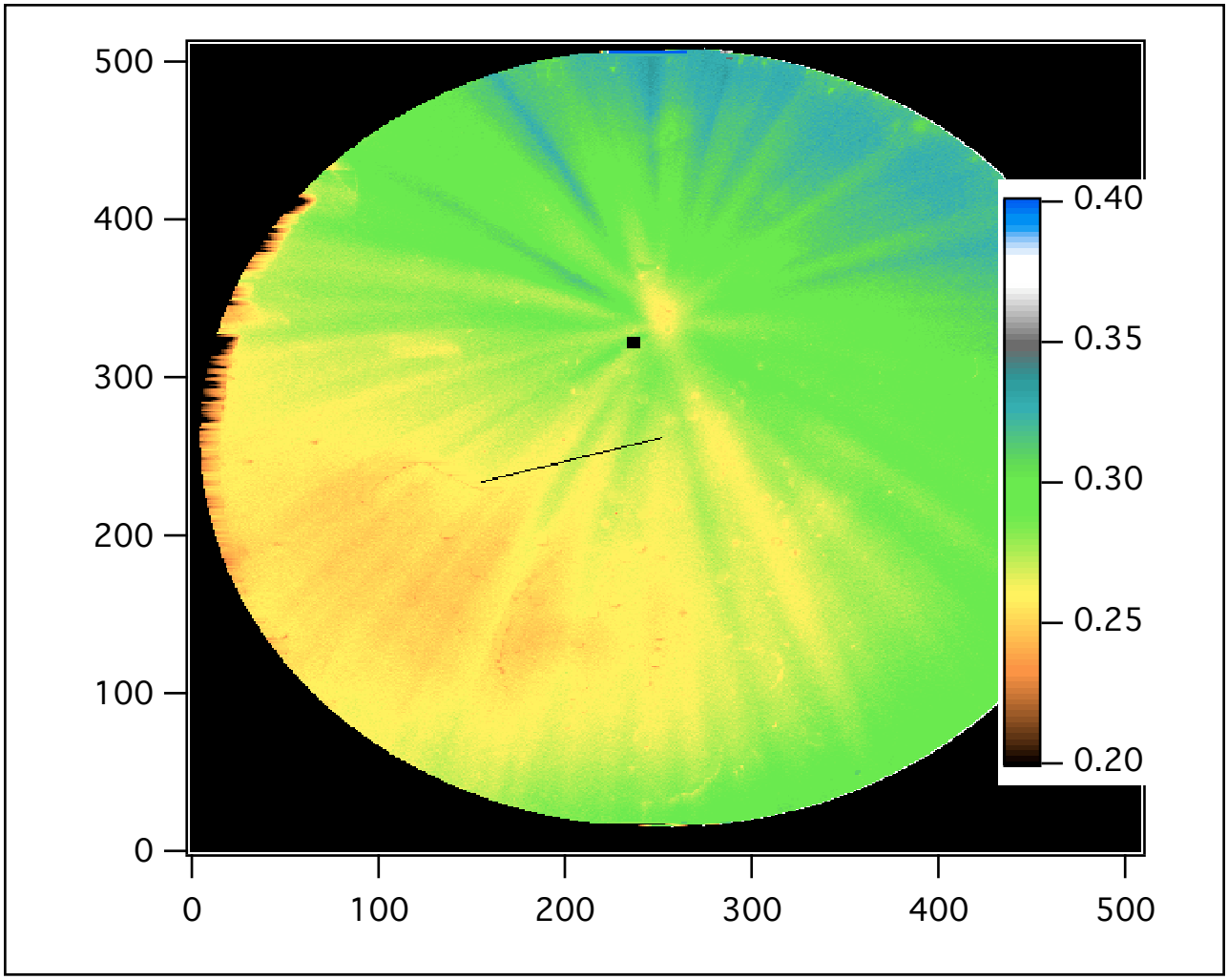
500
400
300
200
100
0
0
100
200
300
400
500
0.40
0.35
0.30
0.25
0.20

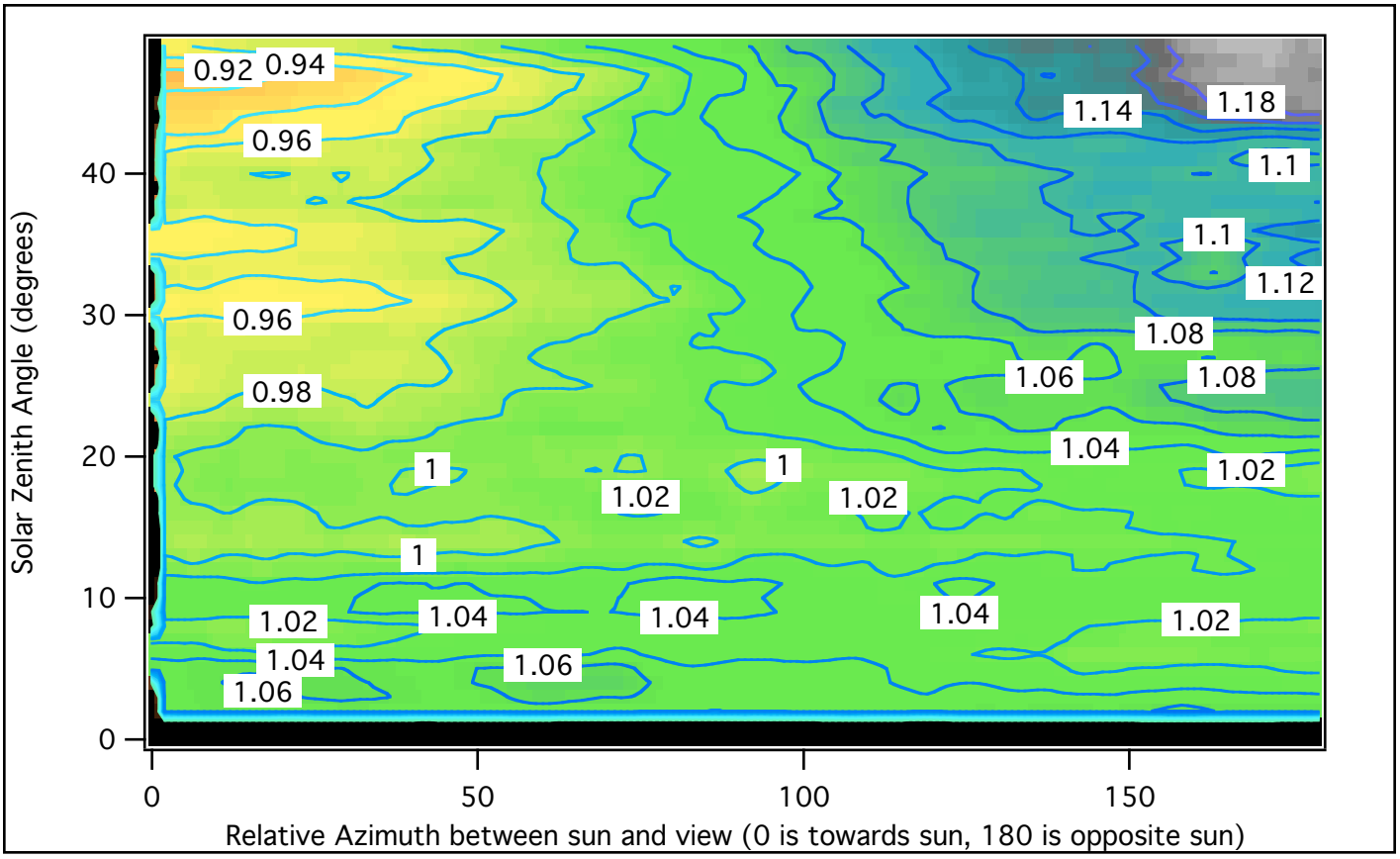
Solar Zenith Angle (degrees)
0
10
20
30
40
0
50
100
150
Relative Azimuth between sun and view (0 is towards sun, 180 is opposite sun)
0.92
0.94
0.96
0.96
0.98
1
1
1
1.02
1.02
1.02
1.04
1.04
1.04
1.04
1.06
1.06
1.14
1.18
1.1
1.1
1.12
1.08
1.06
1.08
1.04
1.02

Downwelling total surface irradiance.

The spectral downwelling surface irradiance was measured using the SIS irradiometer. The data is available throughout the measurement period at two minute resolution and approximately 10nm resolution through the visible. Shown is the total downwelling irradiance for 4 channels in the visible, listed in the figure legend. Variations can be seen in the normal downwelling irradiance pattern can be seen due to clouds. This measurement gives us an idea of the incoming light conditions during the NuRADS measurements. Each figure is for a different day during the small boat portion of the cruise. SIS was also working during the large boat operations.

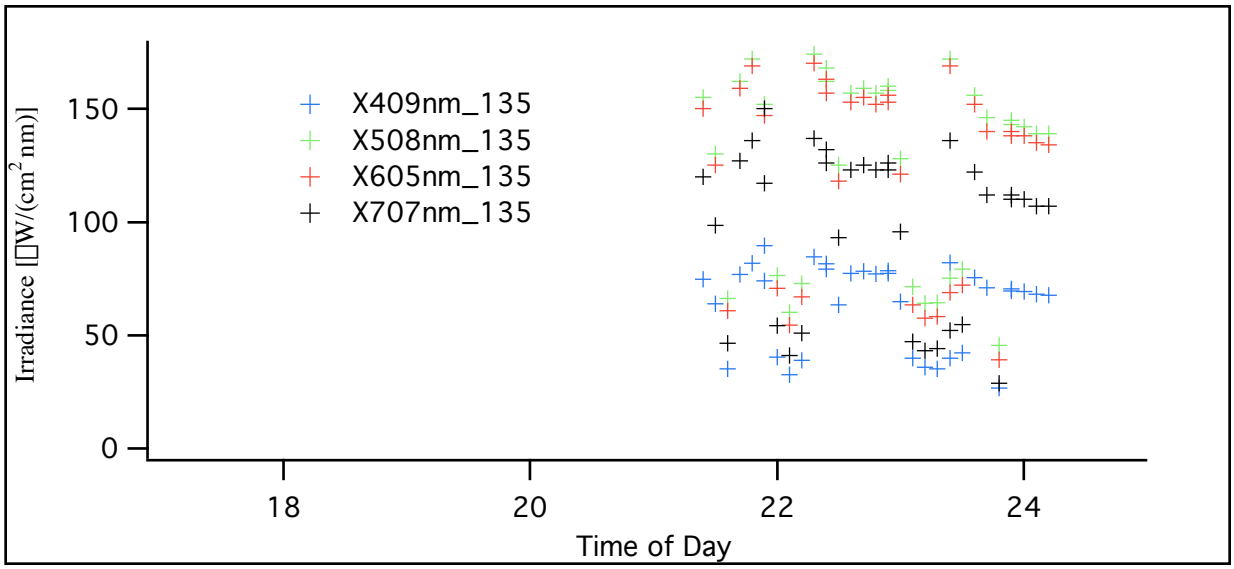
X409nm_135
X508nm_135
X605nm_135
X707nm_135
Irradiance [□W/(cm² nm)]
150
100
50
0
18
20
22
24
Time of Day

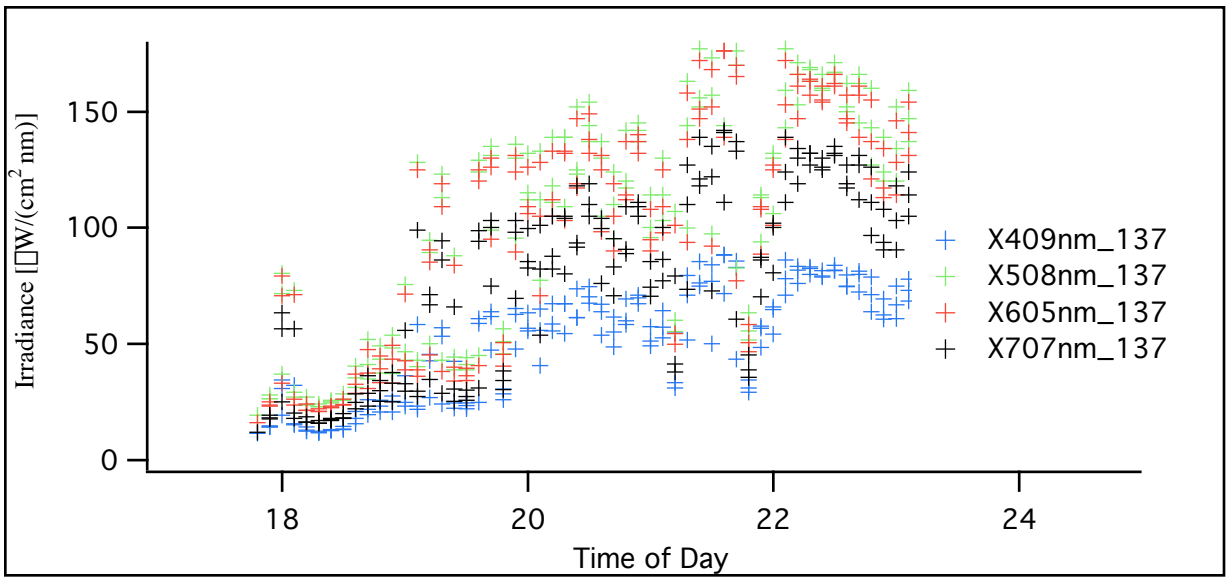
X409nm_137
X508nm_137
X605nm_137
X707nm_137
Irradiance [□W/(cm² nm)]
150
100
50
0
18
20
22
24
Time of Day

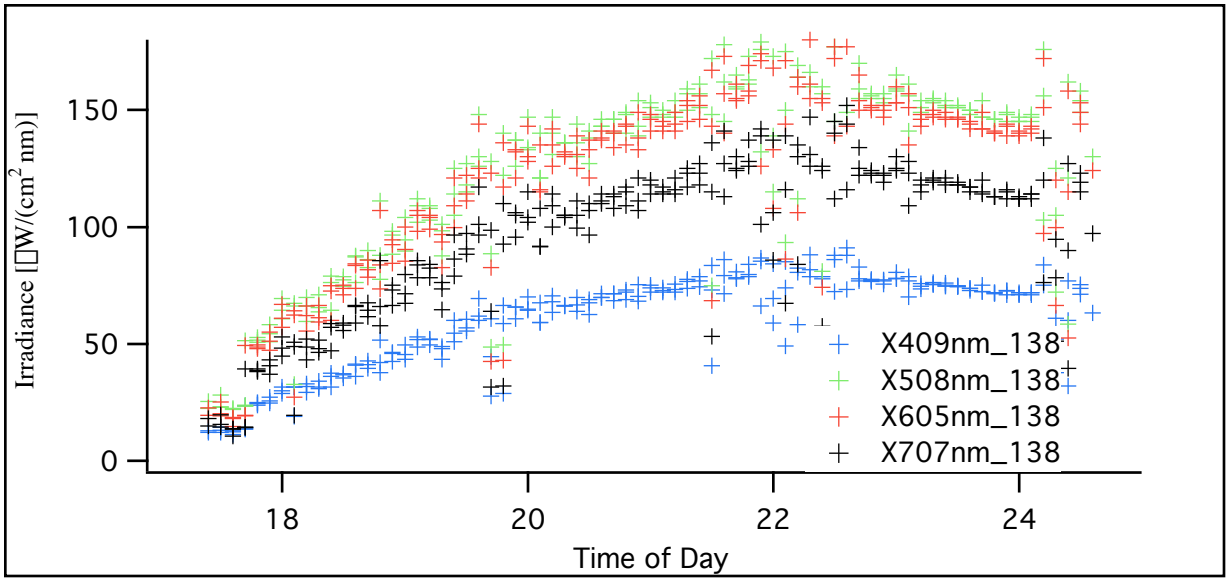
X409nm_138
X508nm_138
X605nm_138
X707nm_138
Irradiance [□W/(cm² nm)]
150
100
50
0
18
20
22
24
Time of Day

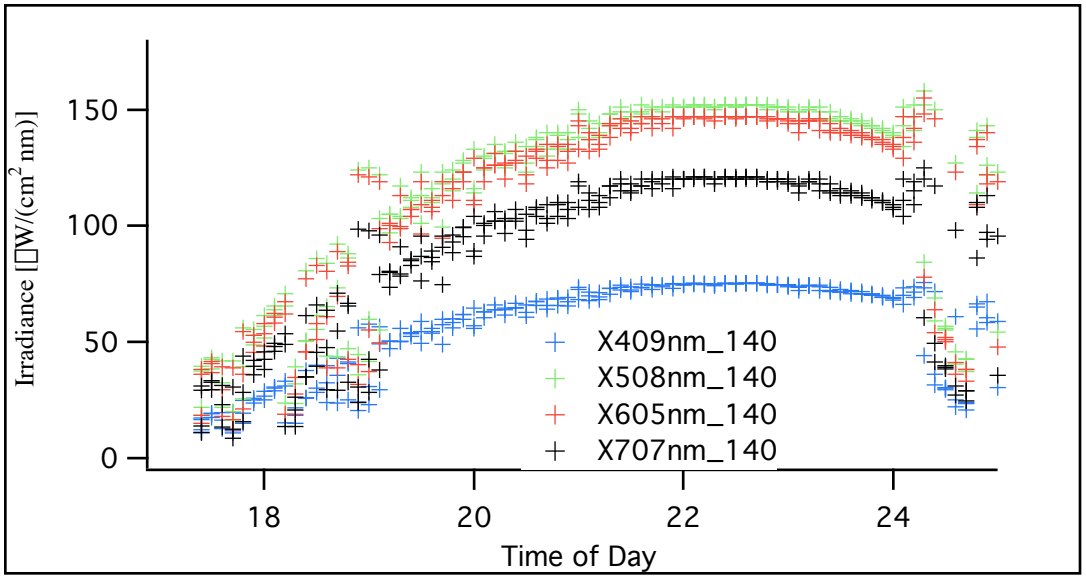
Irradiance [□W/(cm² nm)]
150
100
50
0
18
20
22
24
Time of Day
X409nm_140
X508nm_140
X605nm_140
X707nm_140

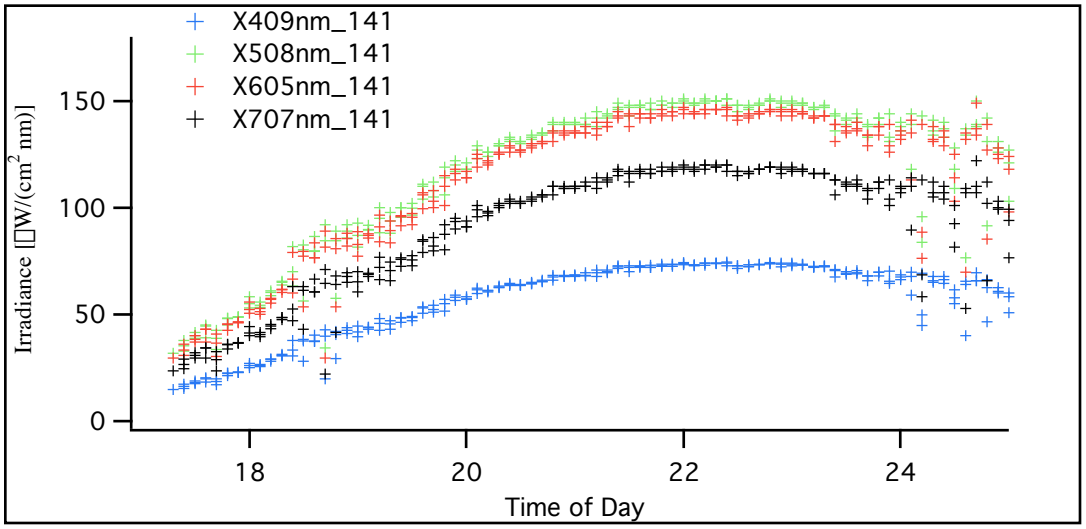
X409nm_141
X508nm_141
X605nm_141
X707nm_141
Irradiance [□W/(cm² nm)]
150
100
50
0
18
20
22
24
Time of Day

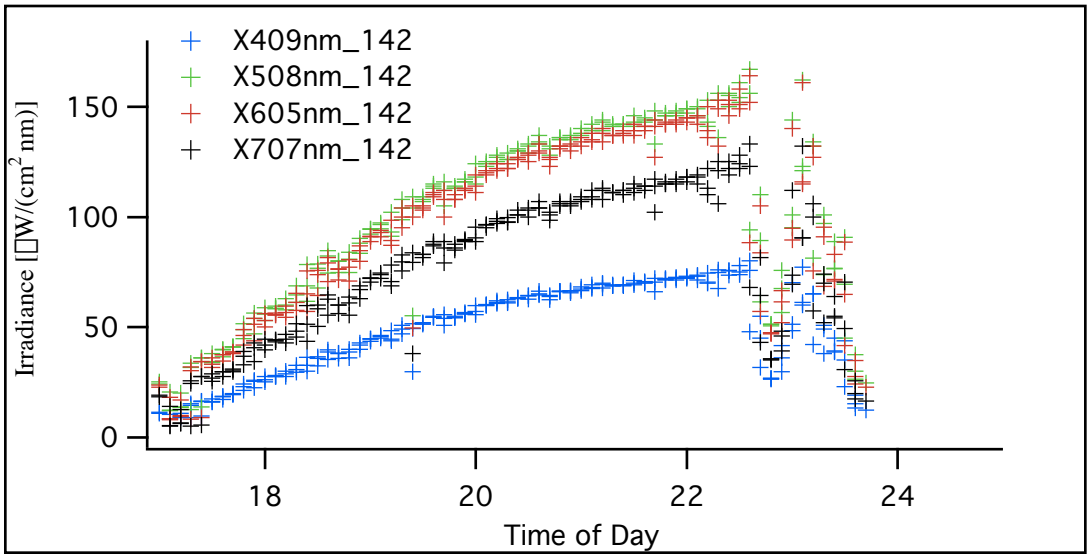
X409nm_142
X508nm_142
X605nm_142
X707nm_142
Irradiance [□W/(cm² nm)]
150
100
50
0
18
20
22
24
Time of Day

Direct/Diffuse Ratio

At periodic times on two days of the cruise the direct diffuse ratio was measured. The following two pages show the results of these measurements. This ratio gives the component of incoming radiance that is in the direct beam versus the diffuse (skylight), which will be useful when interpreting the NuRADS data. This measurement was done spectrally using the Satlantic Microprobe deck cell.

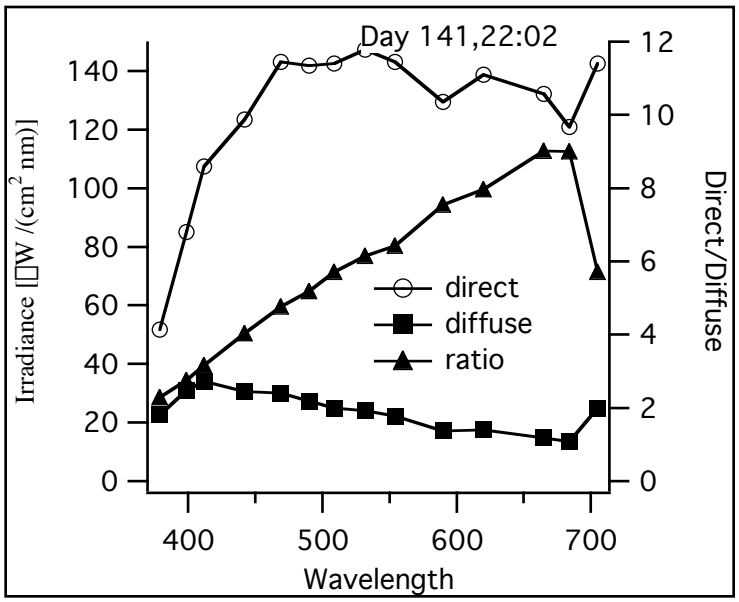
Day 141,22:02
direct
diffuse
ratio
Irradiance [□W /(cm² nm)]
Direct/Diffuse
Wavelength

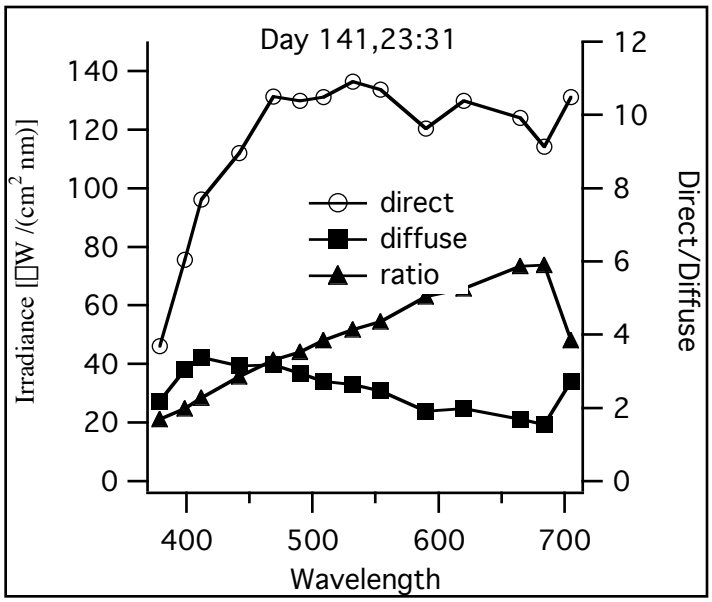
Day 141,23:31
direct
diffuse
ratio
Irradiance [□W /(cm² nm)]
Direct/Diffuse
Wavelength

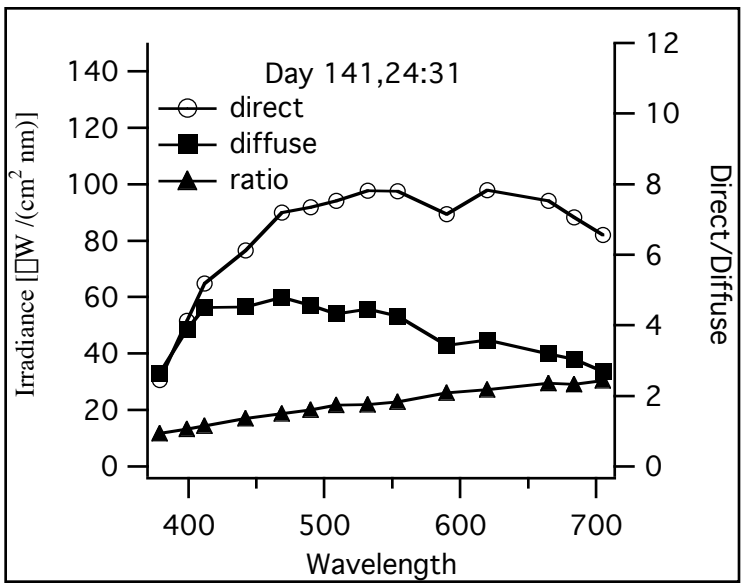
Day 141,24:31
direct
diffuse
ratio
Irradiance [□W /(cm² nm)]
Direct/Diffuse
Wavelength

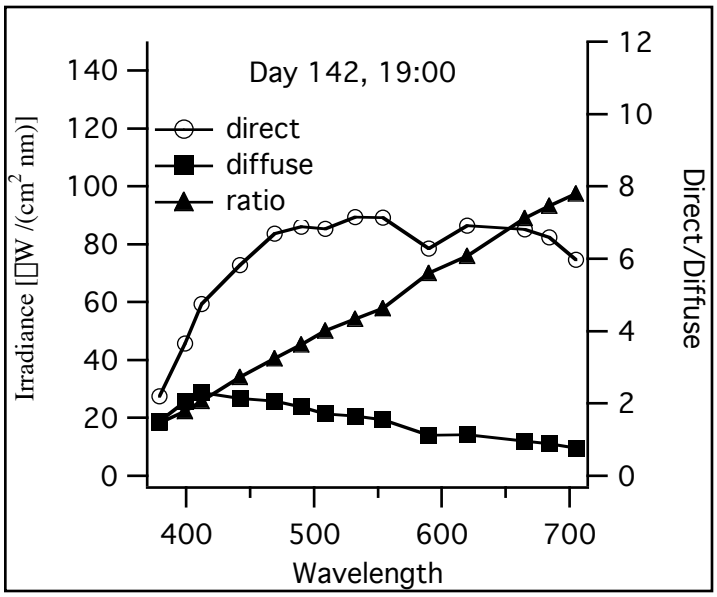
Day 142, 19:00
direct
diffuse
ratio
Irradiance [□W /(cm² nm)]
Direct/Diffuse
Wavelength

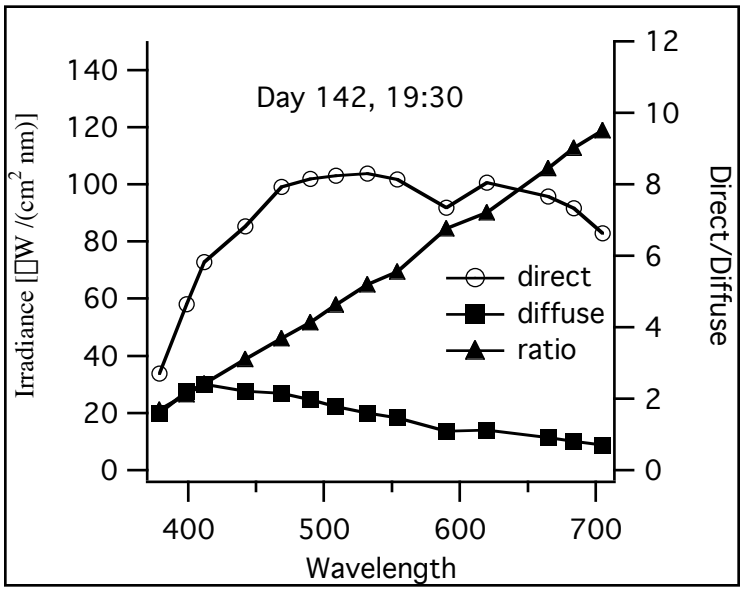
Day 142, 19:30
direct
diffuse
ratio
Irradiance [□W /(cm² nm)]
Direct/Diffuse
Wavelength

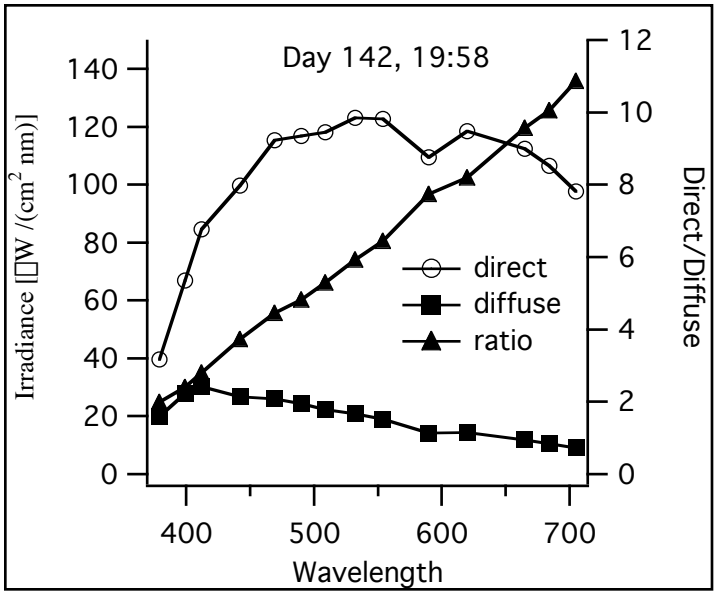
Day 142, 19:58
direct
diffuse
ratio
Irradiance [□W /(cm² nm)]
Direct/Diffuse
Wavelength

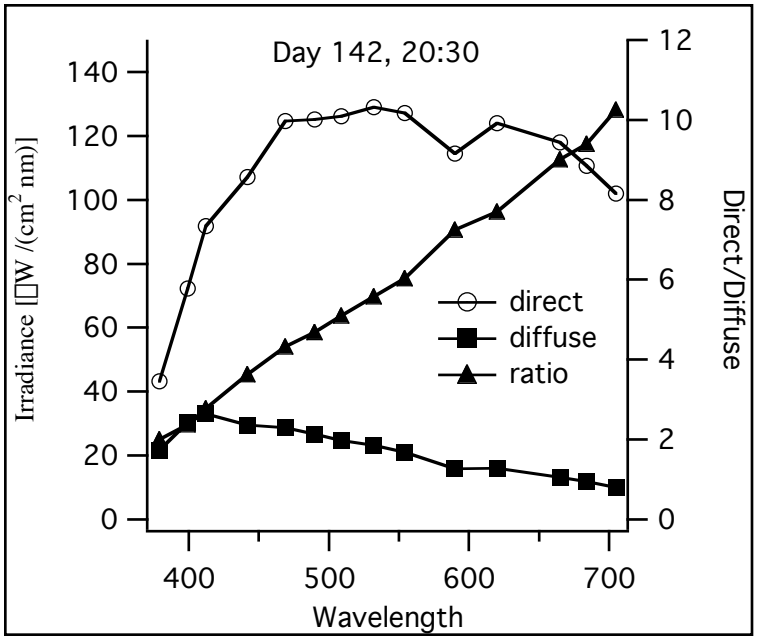
Day 142, 20:30
Irradiance [□W /(cm² nm)]
Direct/Diffuse
Wavelength
direct
diffuse
ratio

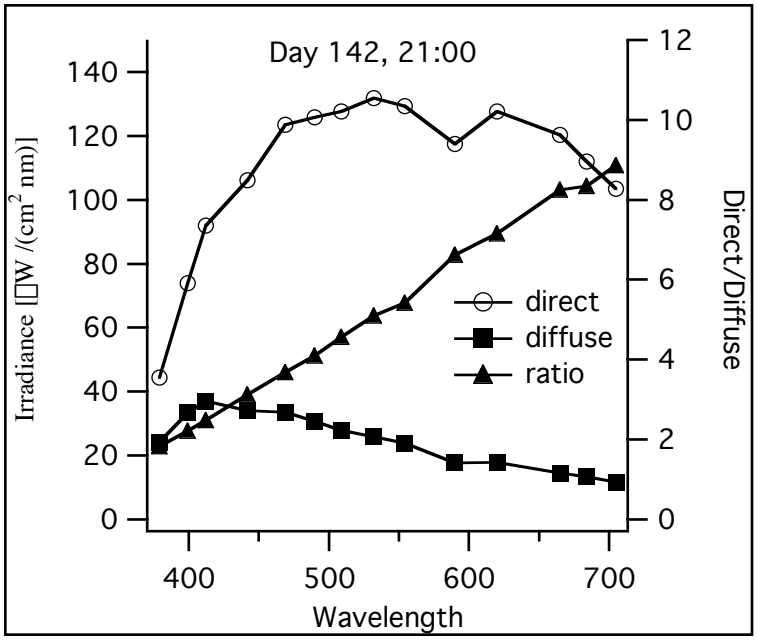
Day 142, 21:00
Irradiance [□W /(cm² nm)]
Direct/Diffuse
Wavelength
direct
diffuse
ratio

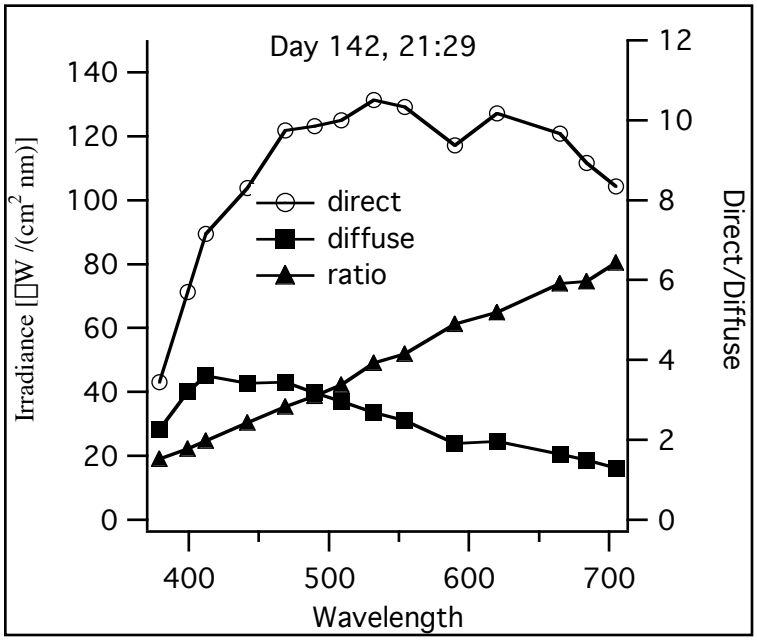
Day 142, 21:29
Irradiance [□W /(cm² nm)]
Direct/Diffuse
Wavelength
direct
diffuse
ratio

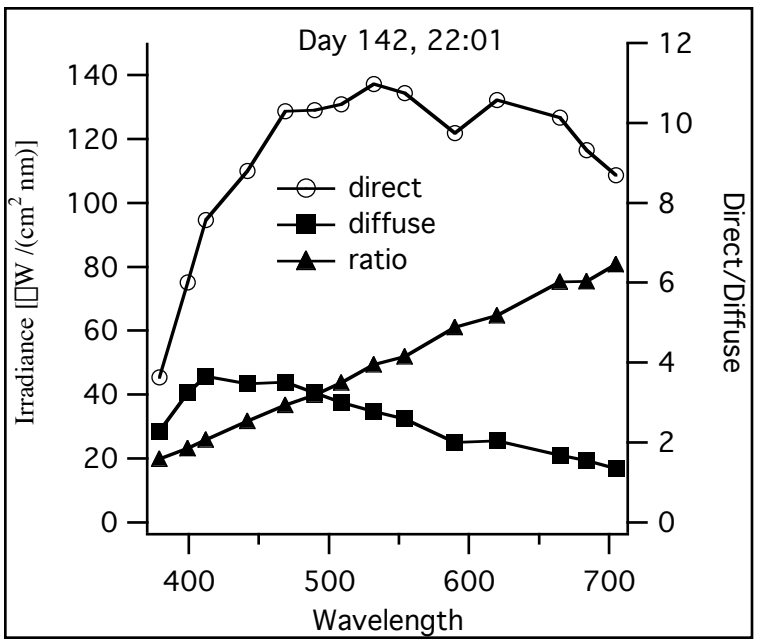
Day 142, 22:01
Irradiance [□W /(cm² nm)]
Direct/Diffuse
Wavelength
direct
diffuse
ratio

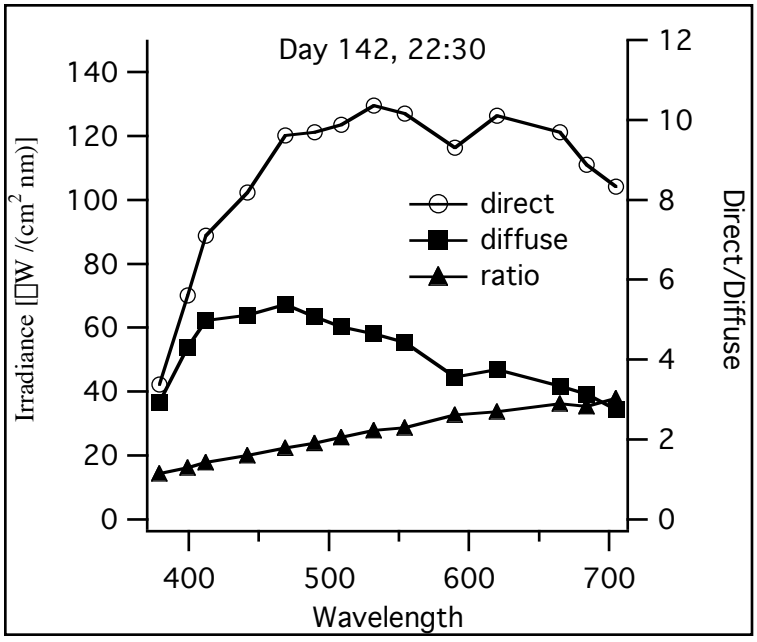
Day 142, 22:30
Irradiance [□W /(cm² nm)]
Direct/Diffuse
Wavelength
direct
diffuse
ratio

AC-9 measurements

Surface water absorption and beam attenuation was measured using an AC-9 in flow through mode. For both measurements the water was near the clear water accuracy limit of the instrument.

Absorption: the following two pages show the plot of absorption vs time during the measurements on each day. The AC-9 manual from wetlabs indicates that the measurement limit for this instrument was +-0.005 m-1. Almost all of this data, after being corrected for salinity, temperature, and calibration offsets (using pure water measurements done each day) was approximately at this limit. Thus the in-situ absorption characteristics are basically those of pure water.

Beam attenuation: On the pages following the absorption plots are the beam attenuation time series during this measurement period. As with absorption, the beam attenuation was very nearly at the instrument accuracy limit. Beam attenuation was almost significantly less than 0.05 m-1, often nearer to zero than this. Thus the beam attenuation is only slightly higher then that of pure water.

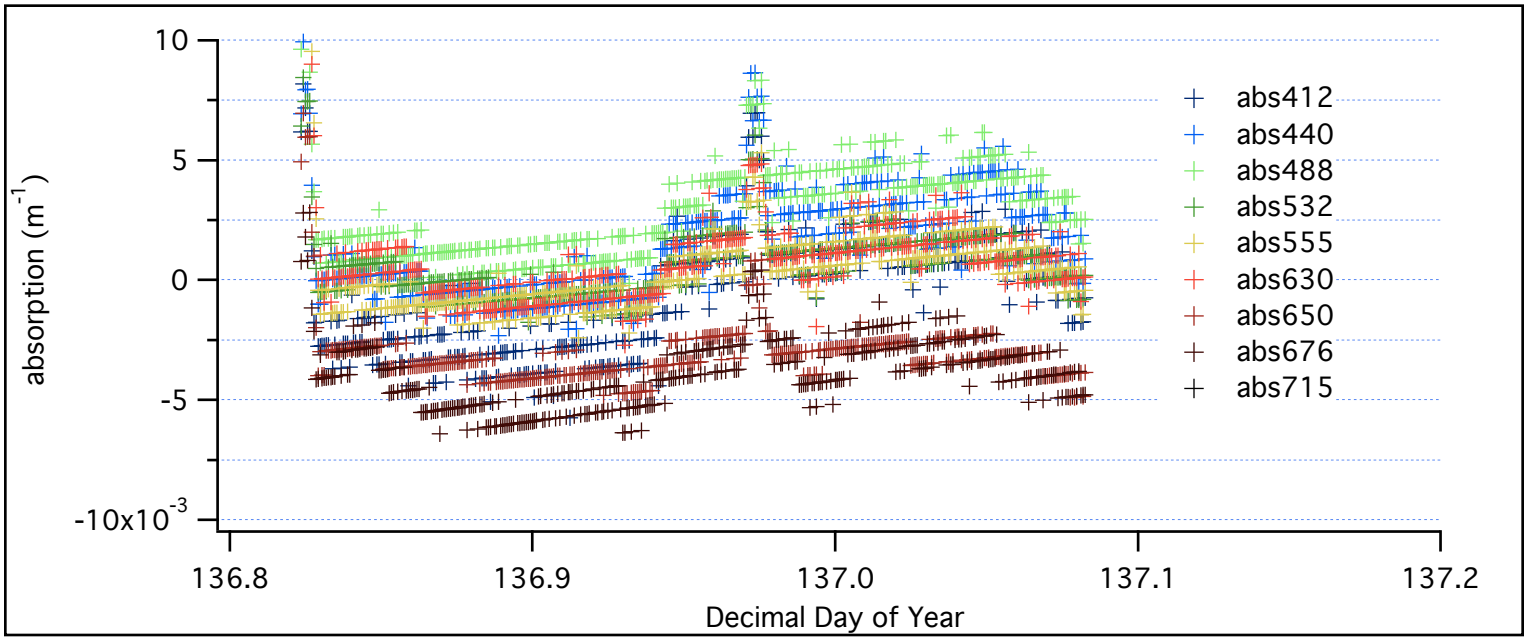
absorption (m-1)
10
5
0
-5
-10x10-3
136.8
136.9
137.0
137.1
137.2
Decimal Day of Year
abs412
abs440
abs488
abs532
abs555
abs630
abs650
abs676
abs715

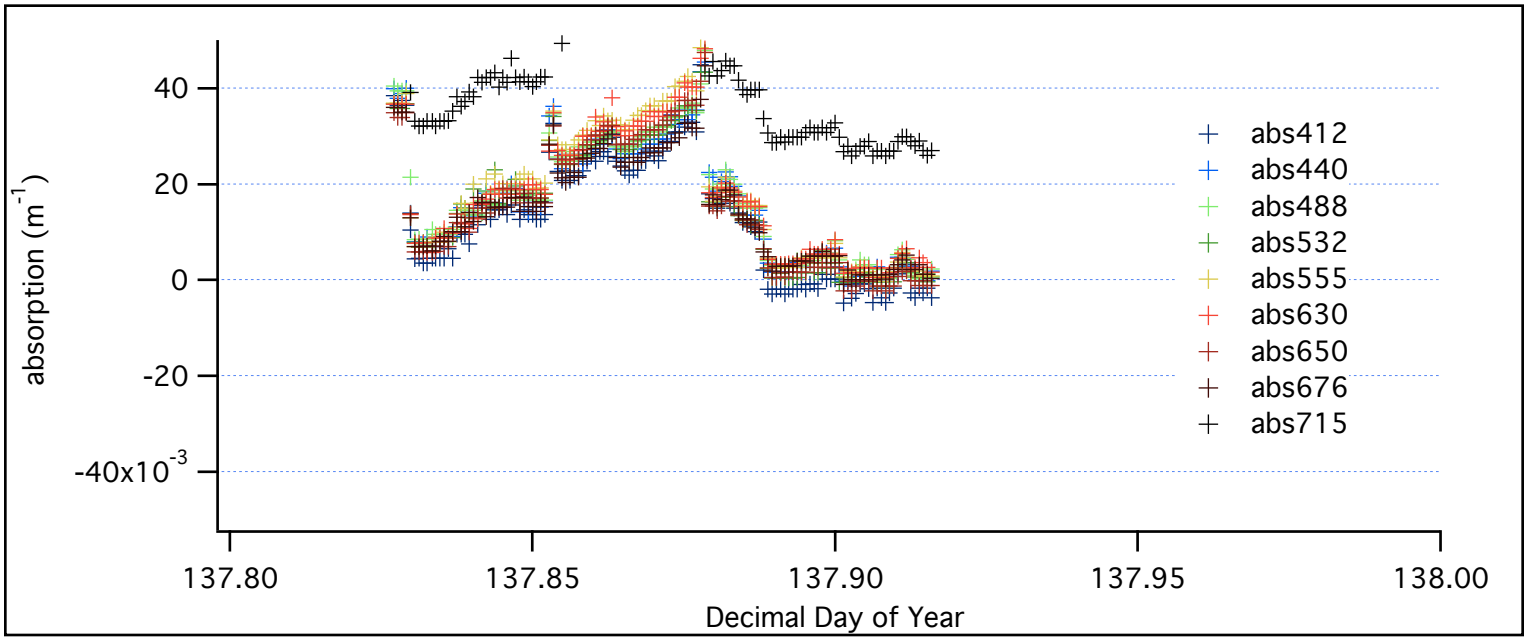
absorption (m-1)
40
20
0
-20
-40x10-3
137.80
137.85
137.90
137.95
138.00
Decimal Day of Year
abs412
abs440
abs488
abs532
abs555
abs630
abs650
abs676
abs715

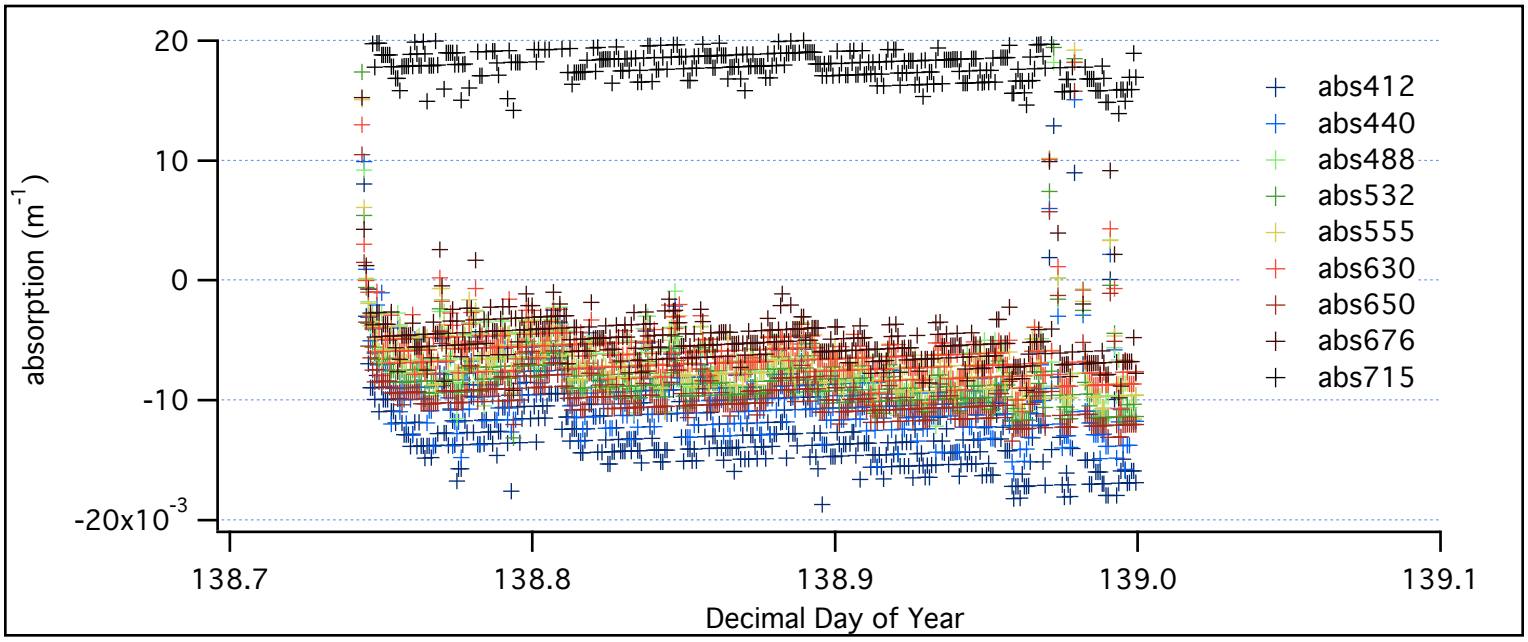
absorption (m-1)
20
10
0
-10
-20x10-3
138.7
138.8
138.9
139.0
139.1
Decimal Day of Year
abs412
abs440
abs488
abs532
abs555
abs630
abs650
abs676
abs715

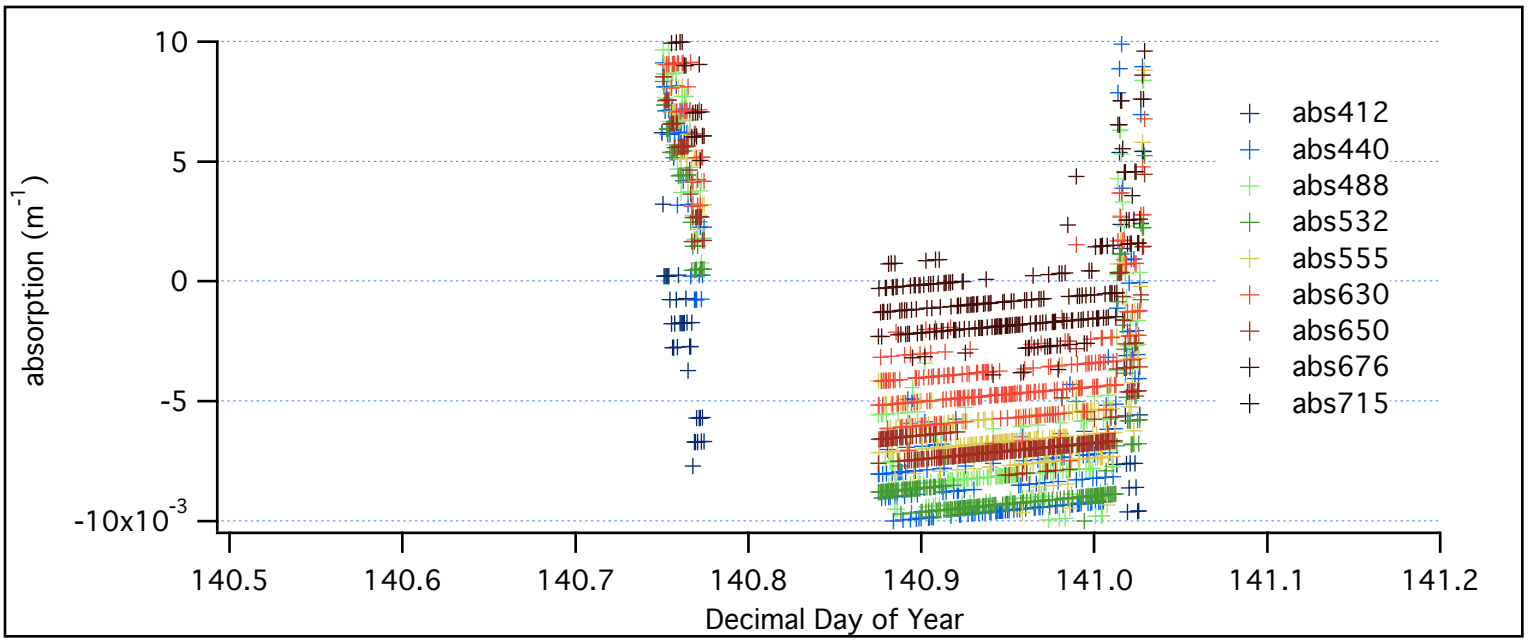
absorption (m-1)
10
5
0
-5
-10x10-3
140.5
140.6
140.7
140.8
140.9
141.0
141.1
141.2
Decimal Day of Year
abs412
abs440
abs488
abs532
abs555
abs630
abs650
abs676
abs715

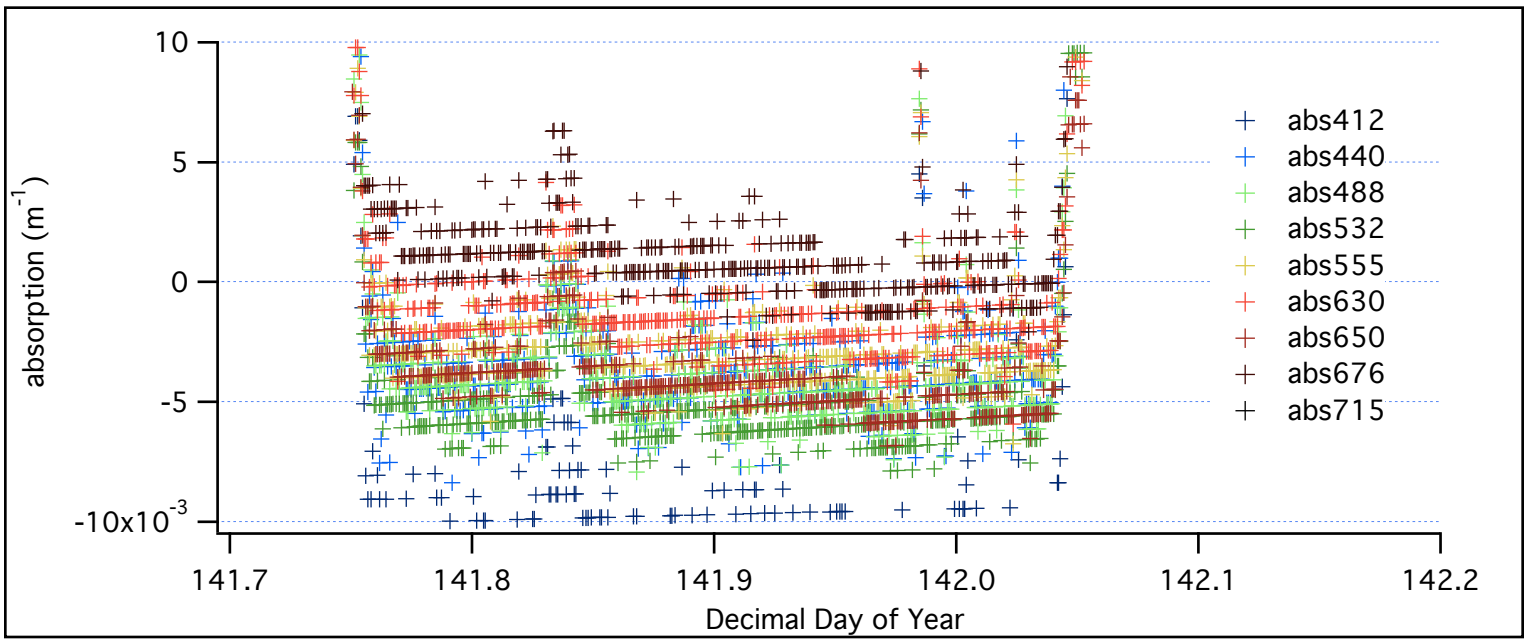
absorption (m-1)
10
5
0
-5
-10x10-3
141.7
141.8
141.9
142.0
142.1
142.2
Decimal Day of Year
abs412
abs440
abs488
abs532
abs555
abs630
abs650
abs676
abs715

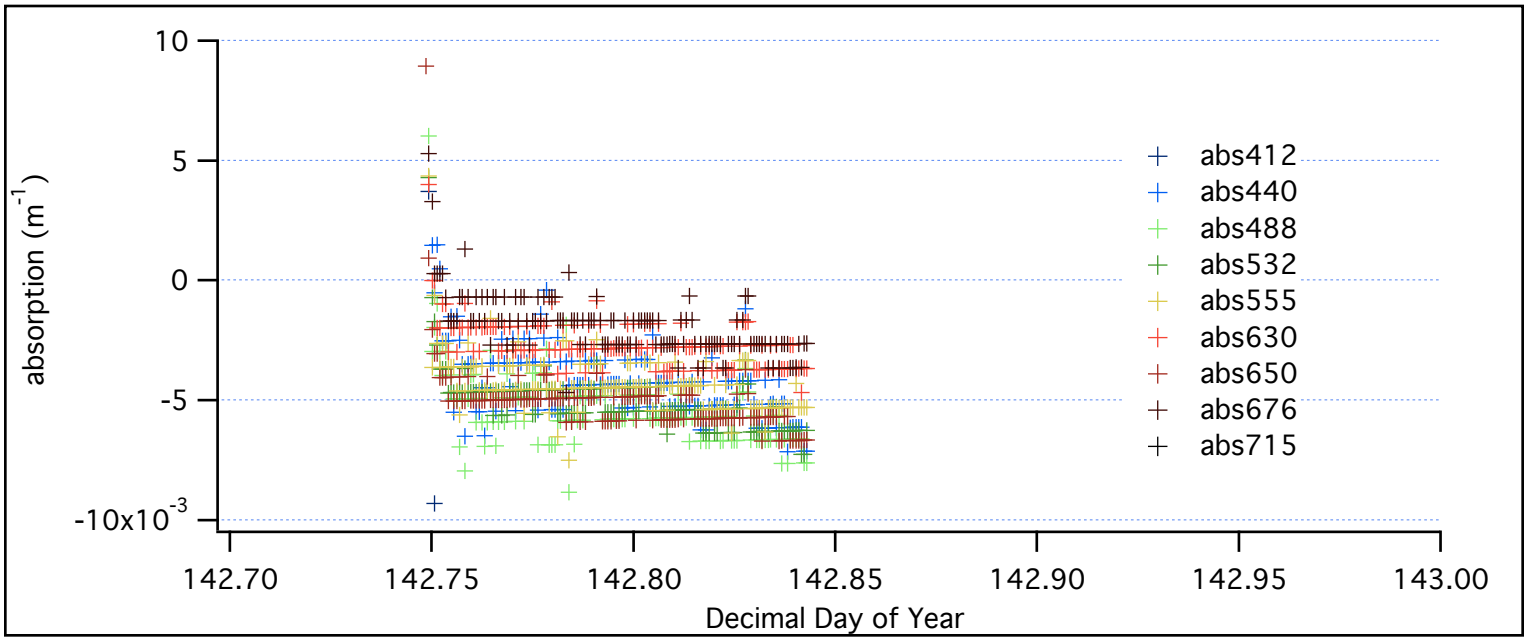
absorption (m-1)
10
5
0
-5
-10x10-3
142.70
142.75
142.80
142.85
142.90
142.95
143.00
Decimal Day of Year
abs412
abs440
abs488
abs532
abs555
abs630
abs650
abs676
abs715

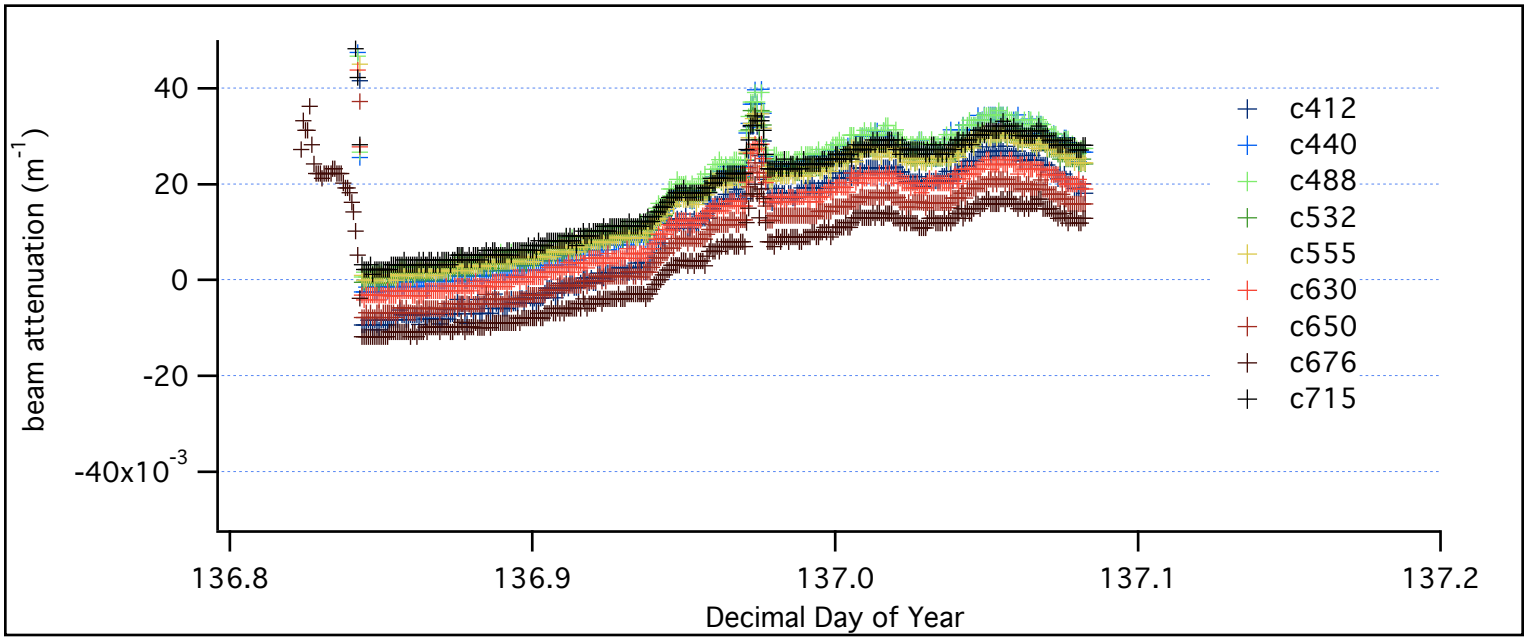
beam attenuation (m-1)
40
20
0
-20
-40x10-3
136.8
136.9
137.0
137.1
137.2
Decimal Day of Year
c412
c440
c488
c532
c555
c630
c650
c676
c715

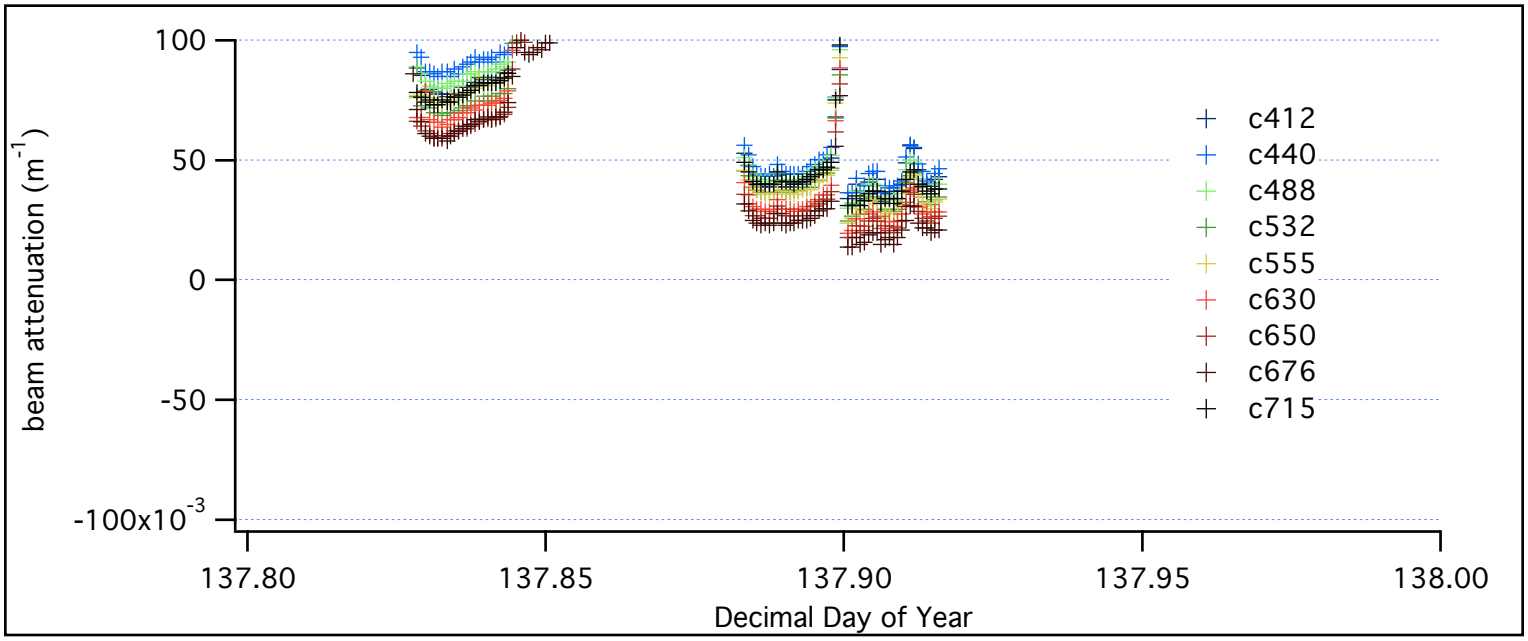
beam attenuation (m-1)
100
50
0
-50
-100x10-3
137.80
137.85
137.90
137.95
138.00
Decimal Day of Year
c412
c440
c488
c532
c555
c630
c650
c676
c715

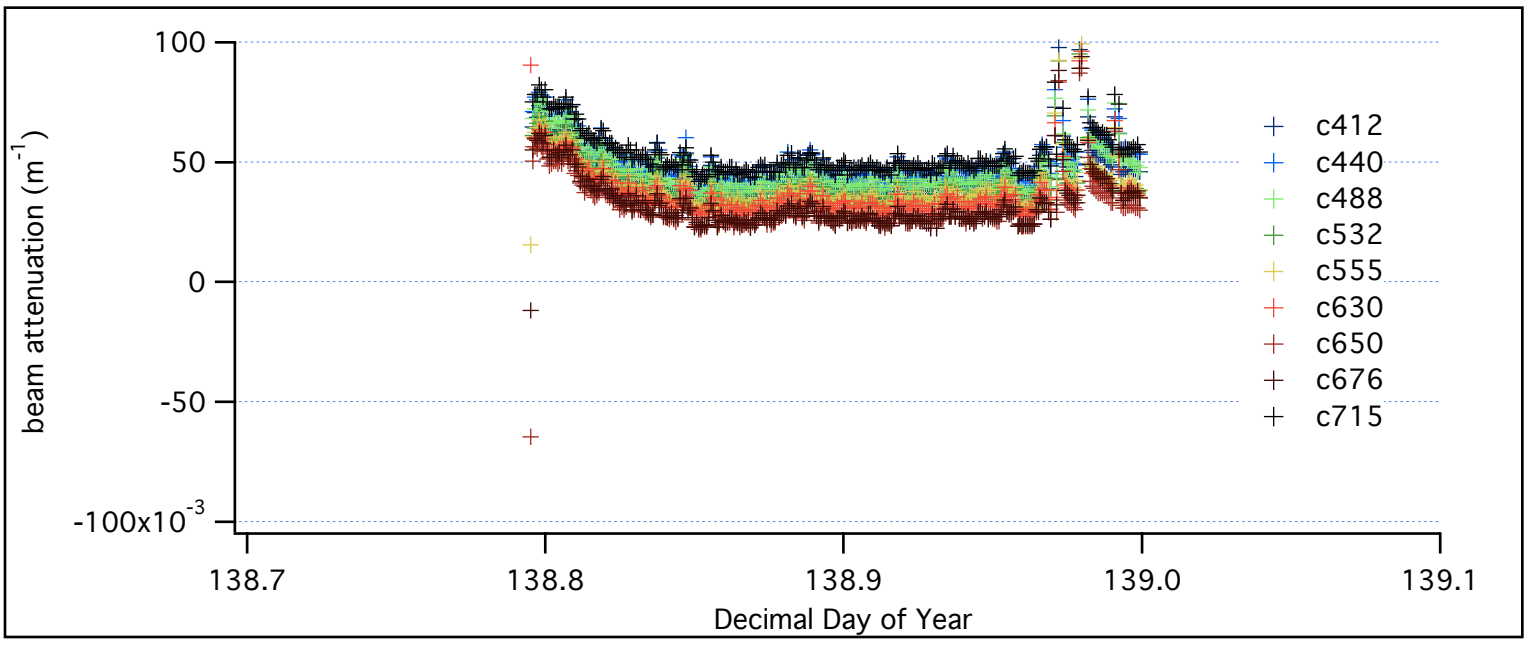
beam attenuation (m-1)
100
50
0
-50
-100x10-3
138.7
138.8
138.9
139.0
139.1
Decimal Day of Year
c412
c440
c488
c532
c555
c630
c650
c676
c715

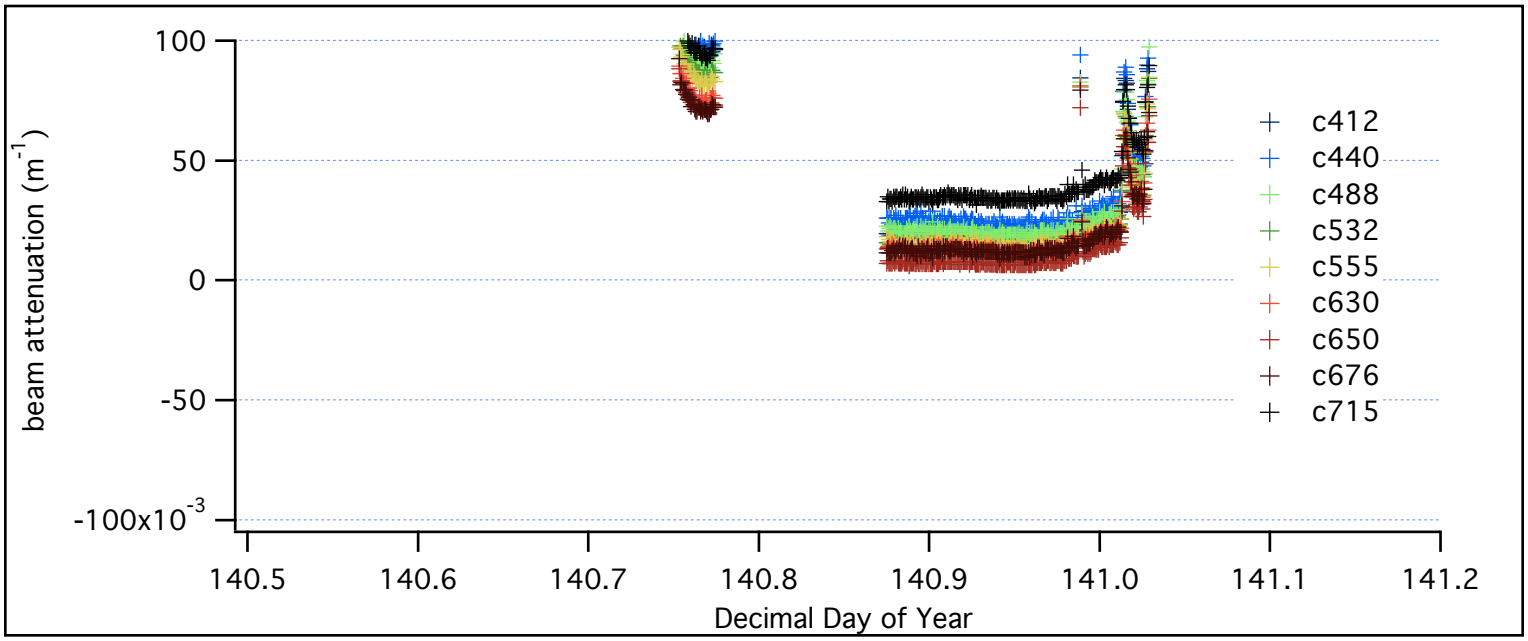
100
50
0
-50
-100x10^-3
beam attenuation (m^-1)
140.5
140.6
140.7
140.8
140.9
141.0
141.1
141.2
Decimal Day of Year
c412
c440
c488
c532
c555
c630
c650
c676
c715

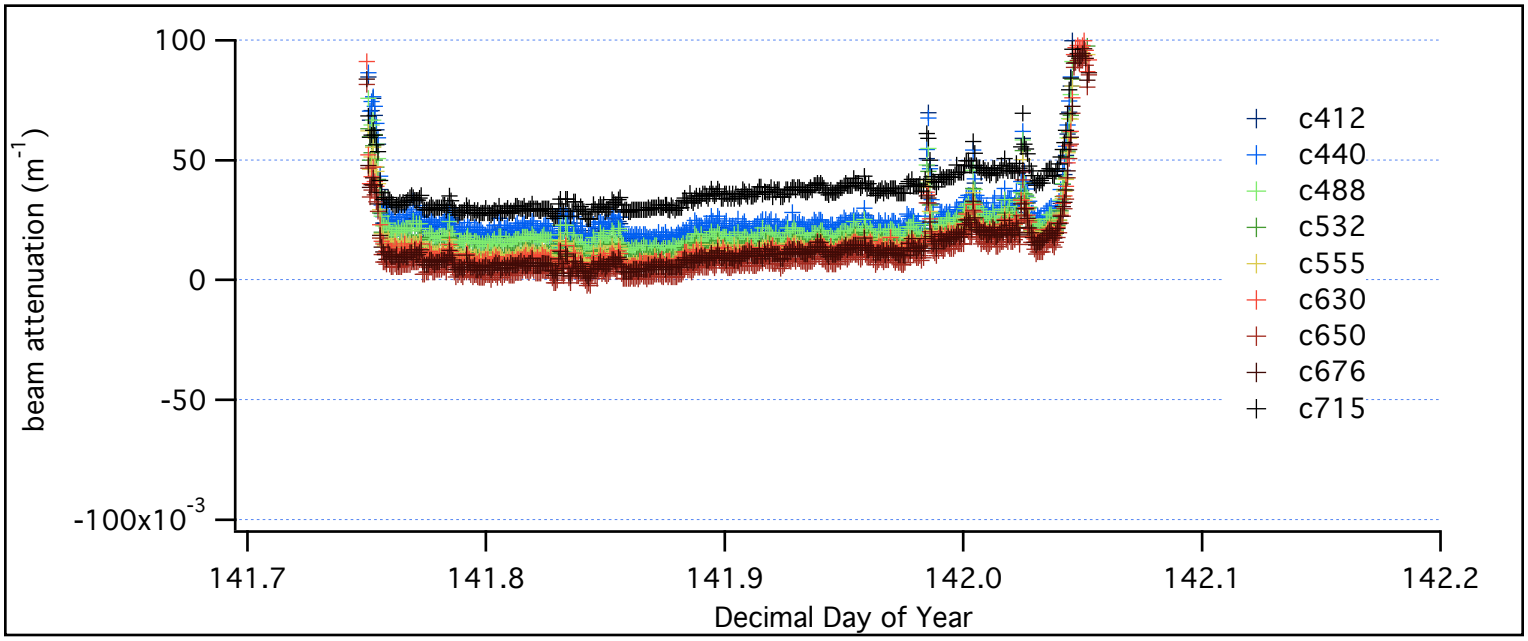
100
50
0
-50
-100x10^-3
beam attenuation (m^-1)
141.7
141.8
141.9
142.0
142.1
142.2
Decimal Day of Year
c412
c440
c488
c532
c555
c630
c650
c676
c715

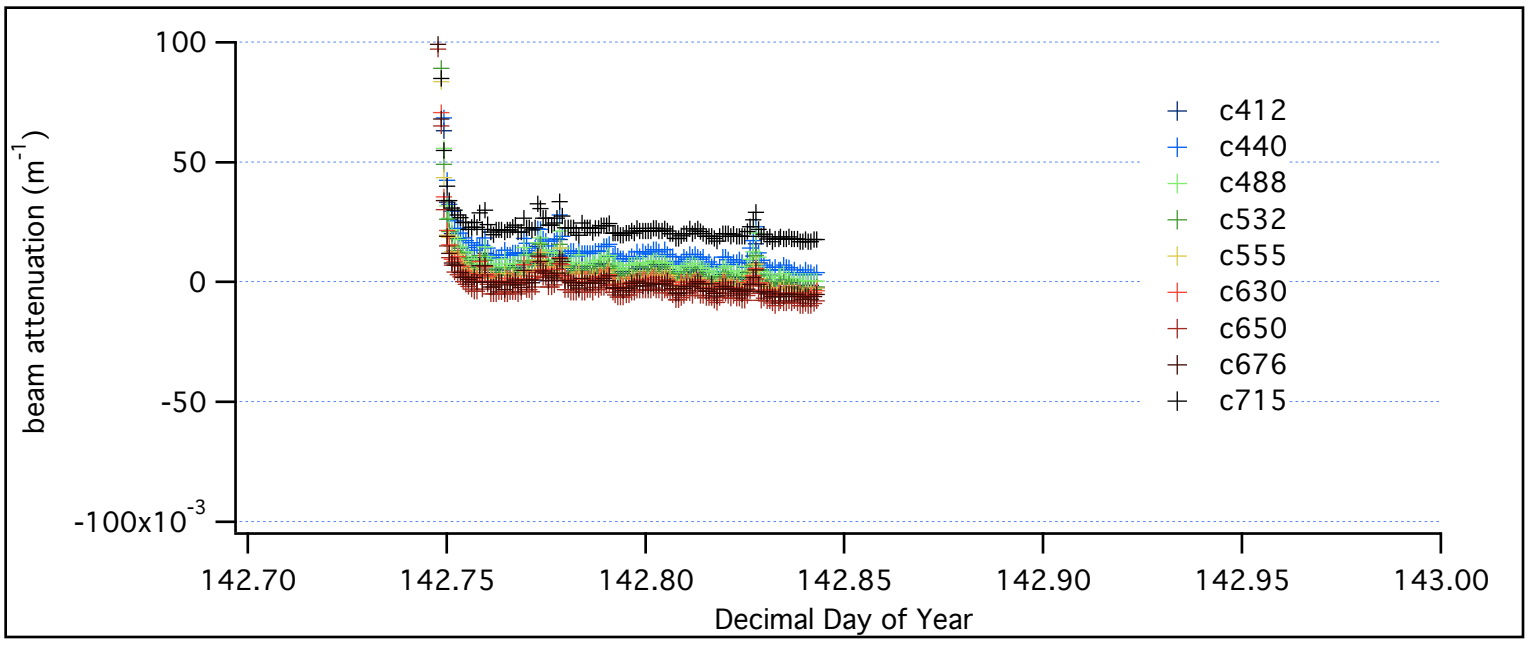
100
50
0
-50
-100x10^-3
beam attenuation (m^-1)
142.70
142.75
142.80
142.85
142.90
142.95
143.00
Decimal Day of Year
c412
c440
c488
c532
c555
c630
c650
c676
c715

Satlantic temperature profiles

The Satlantic radiometer was used to make measurements of the near surface water structure. The vertical casts showing the water temperature profile are shown in the next figures. On all days the water column was fairly mixed to 30m, then a thermocline began. On the last two days (when it was calmer) a very shallow warmer layer of water existed on the surface.

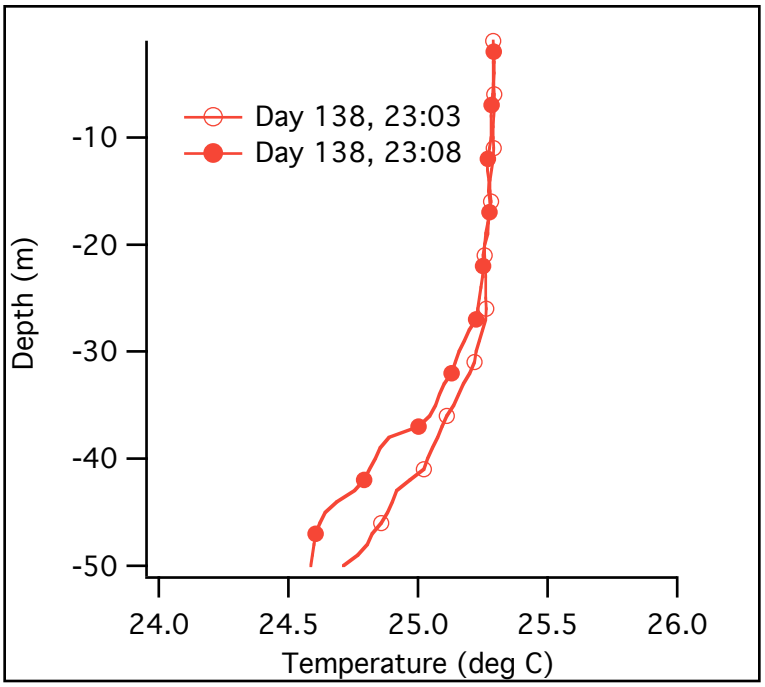
Day 138, 23:03
Day 138, 23:08
-10
-20
-30
-40
-50
Depth (m)
24.0
24.5
25.0
25.5
26.0
Temperature (deg C)

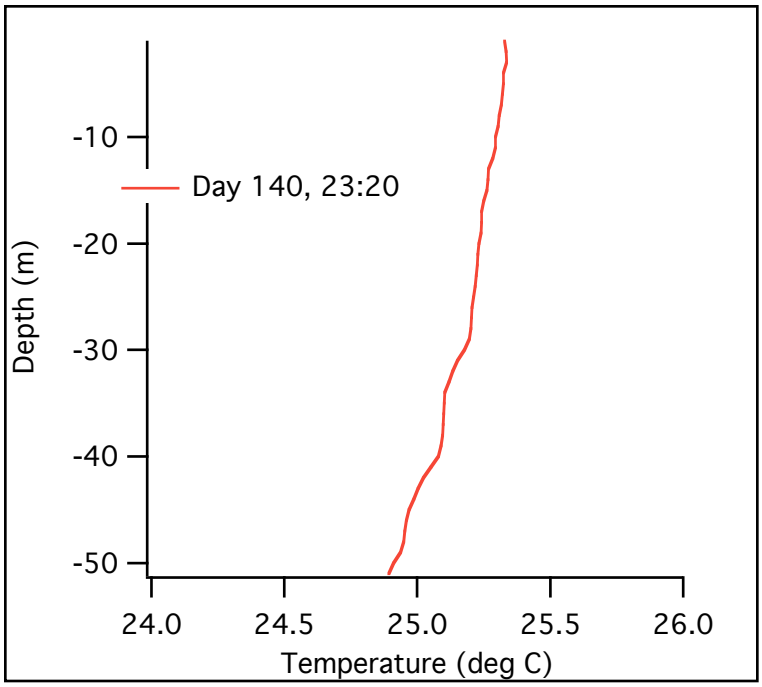
Day 140, 23:20
-10
-20
-30
-40
-50
Depth (m)
24.0
24.5
25.0
25.5
26.0
Temperature (deg C)

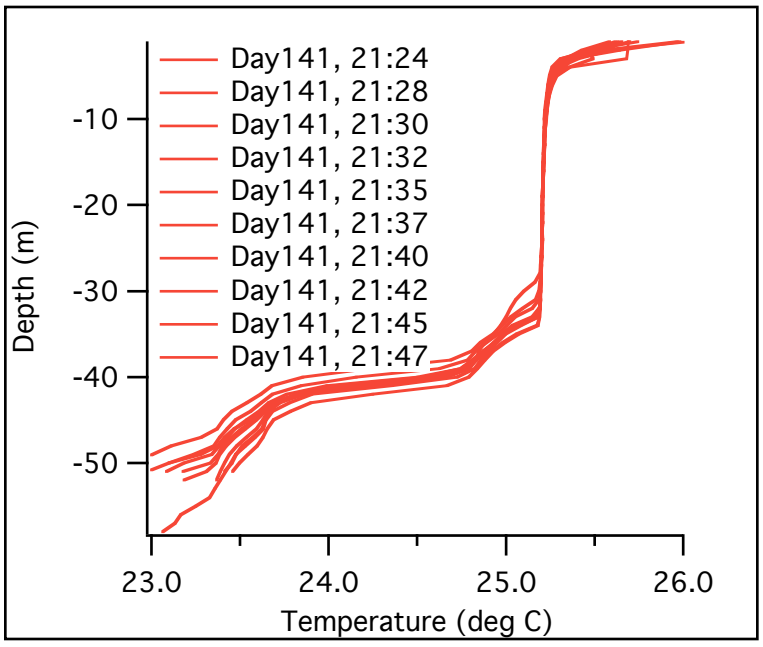
Day141, 21:24
Day141, 21:28
Day141, 21:30
Day141, 21:32
Day141, 21:35
Day141, 21:37
Day141, 21:40
Day141, 21:42
Day141, 21:45
Day141, 21:47
-10
-20
-30
-40
-50
Depth (m)
23.0
24.0
25.0
26.0
Temperature (deg C)

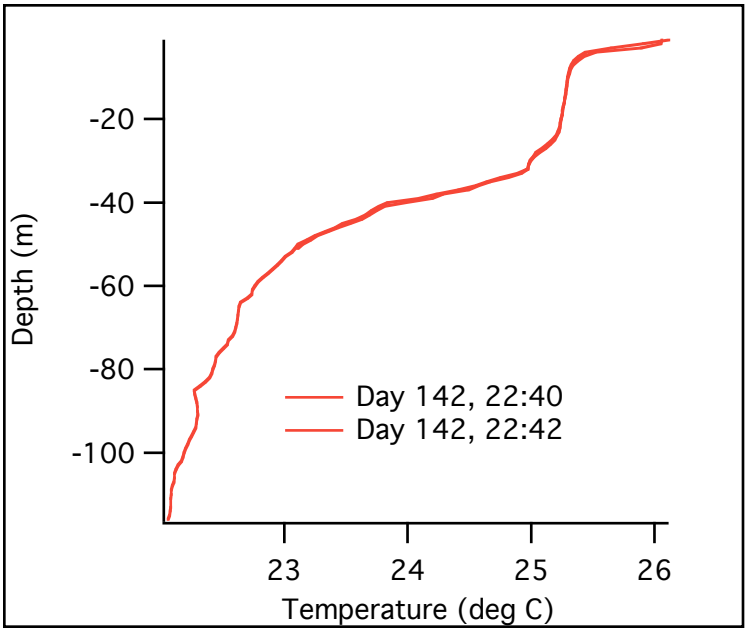
Day 142, 22:40
Day 142, 22:42
-20
-40
-60
-80
-100
Depth (m)
23
24
25
26
Temperature (deg C)

The last figures are the meteorological data. The relative humidity was usually between 70 and 80%, atmospheric pressure varied between 1014 and 1018, and temperature was fairly constant at around 25 deg C. Probably the most important fact for this study is that the wind was high (>20 mph) for most of the data set until the last two days. Thus sea state was fairly high (4-6 foot).

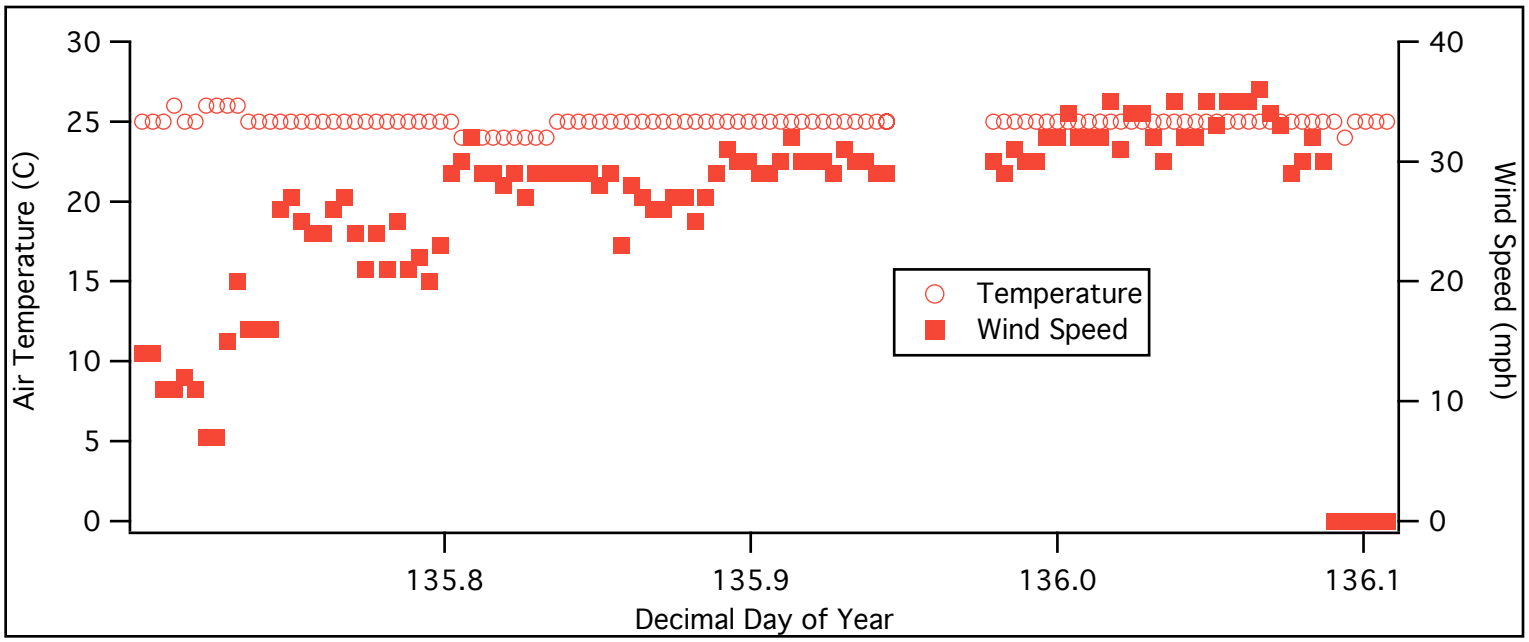
Air Temperature (C)
Wind Speed (mph)
Temperature
Wind Speed
Decimal Day of Year
135.8
135.9
136.0
136.1

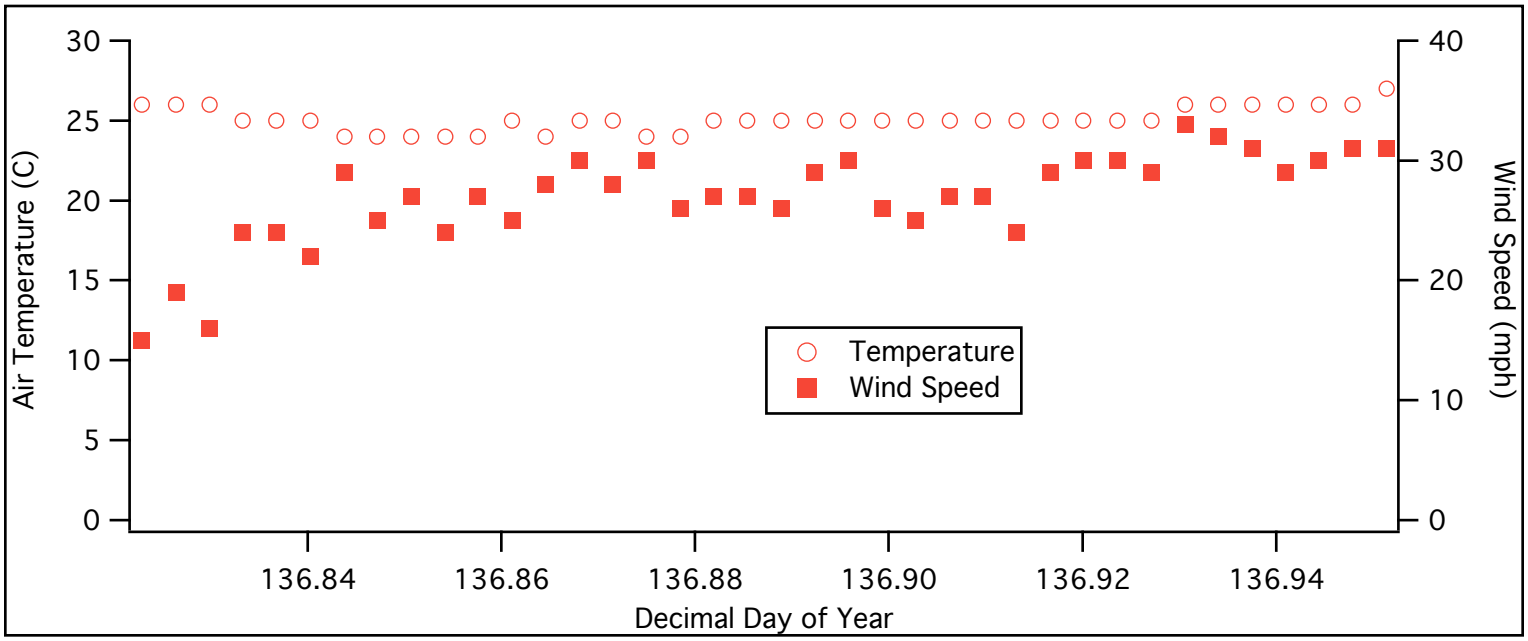
Air Temperature (C)
Wind Speed (mph)
Temperature
Wind Speed
Decimal Day of Year
136.84
136.86
136.88
136.90
136.92
136.94

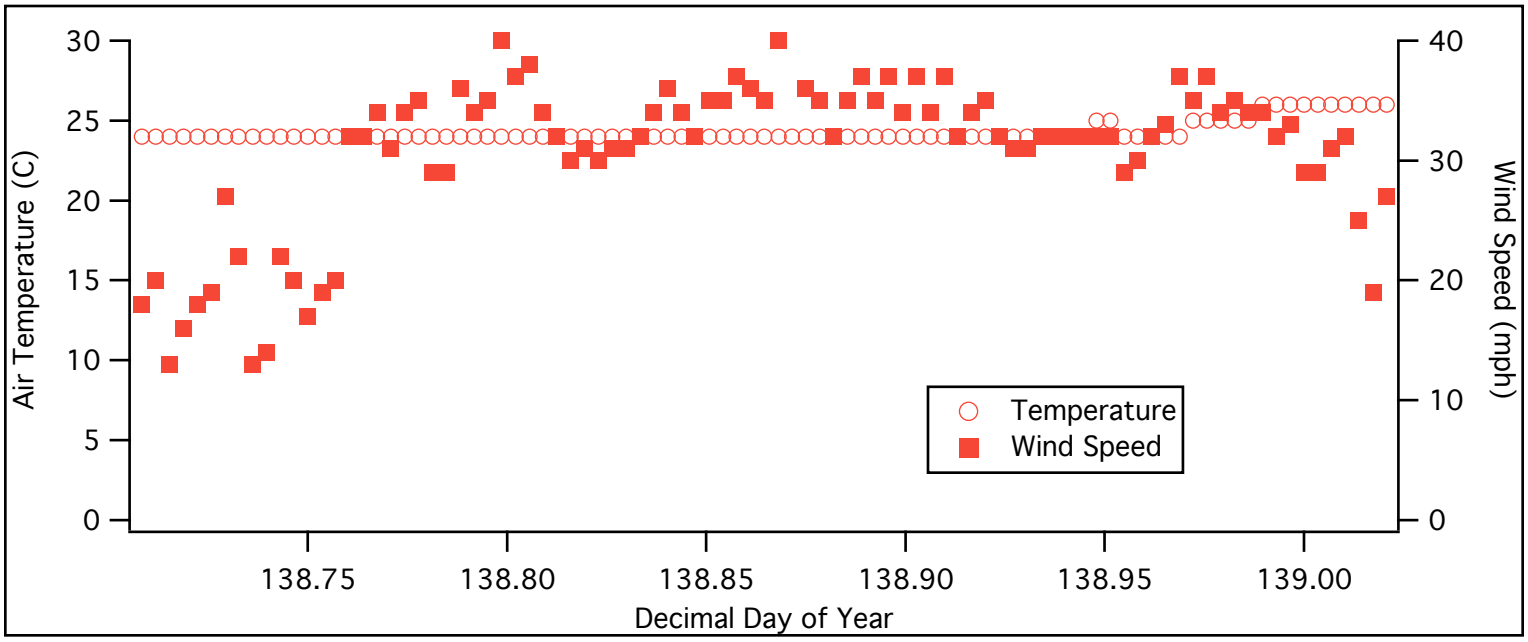
Air Temperature (C)
Wind Speed (mph)
Temperature
Wind Speed
Decimal Day of Year
138.75
138.80
138.85
138.90
138.95
139.00

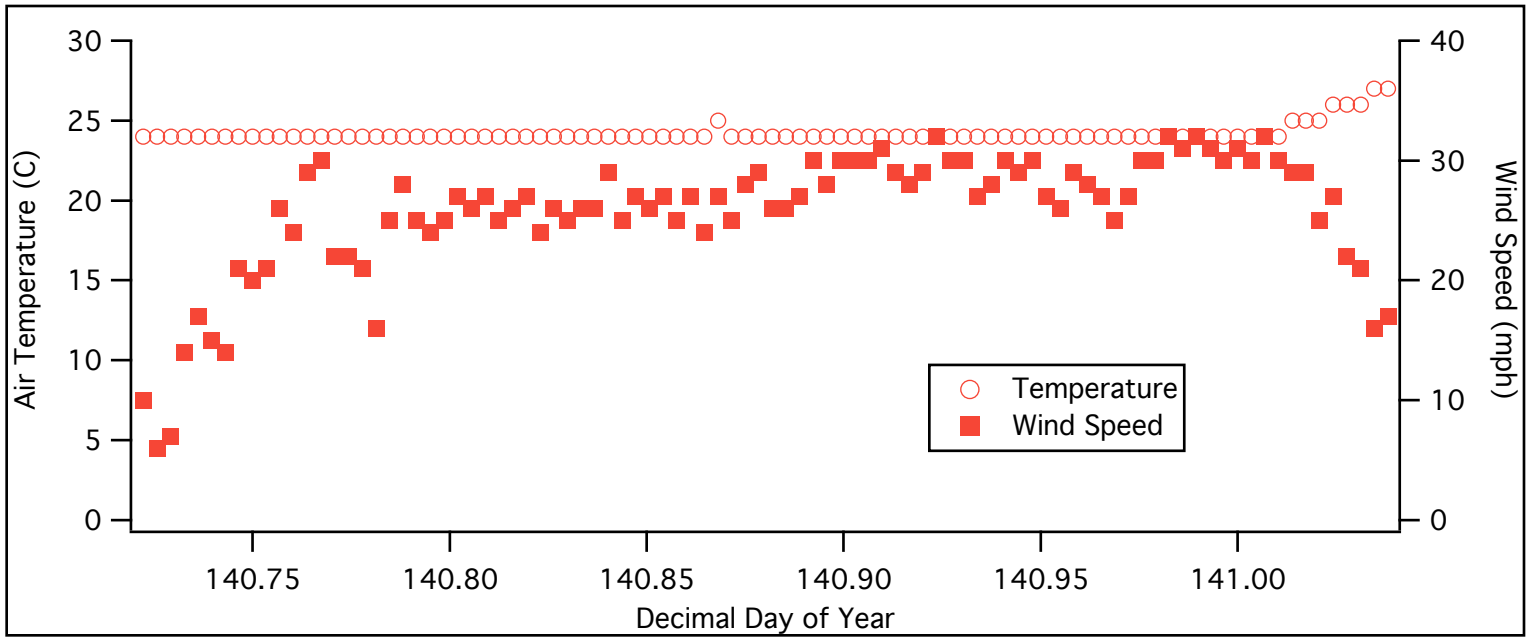
Air Temperature (C)
Wind Speed (mph)
Temperature
Wind Speed
Decimal Day of Year
140.75
140.80
140.85
140.90
140.95
141.00

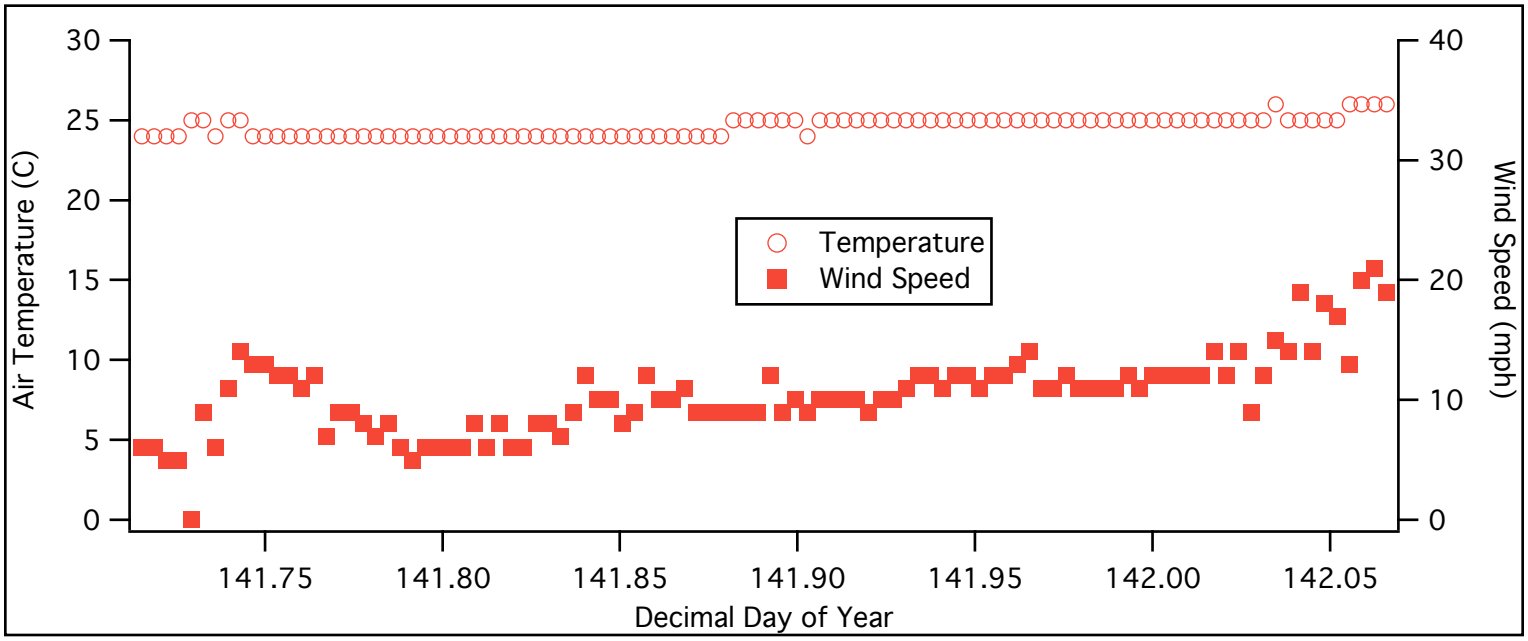
Air Temperature (C)
Wind Speed (mph)
Temperature
Wind Speed
Decimal Day of Year
141.75
141.80
141.85
141.90
141.95
142.00
142.05

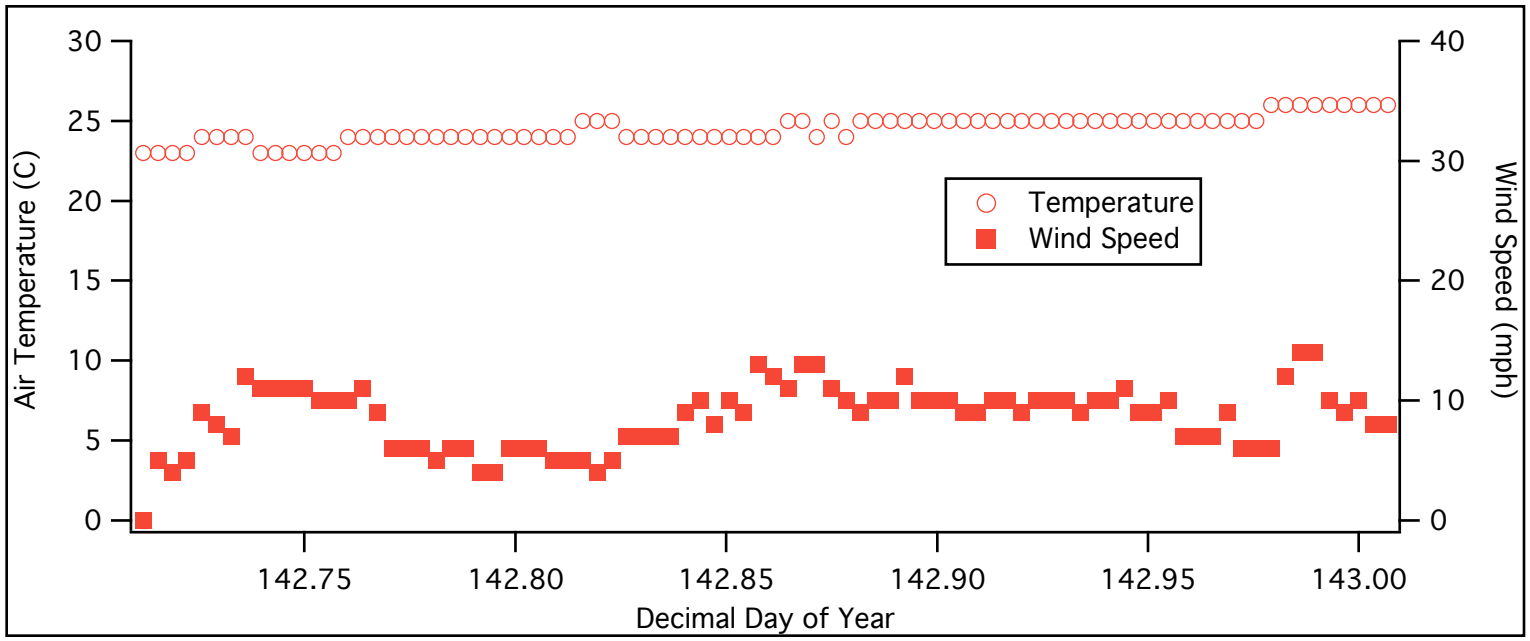
Air Temperature (C)
Wind Speed (mph)
Temperature
Wind Speed
Decimal Day of Year
142.75
142.80
142.85
142.90
142.95
143.00

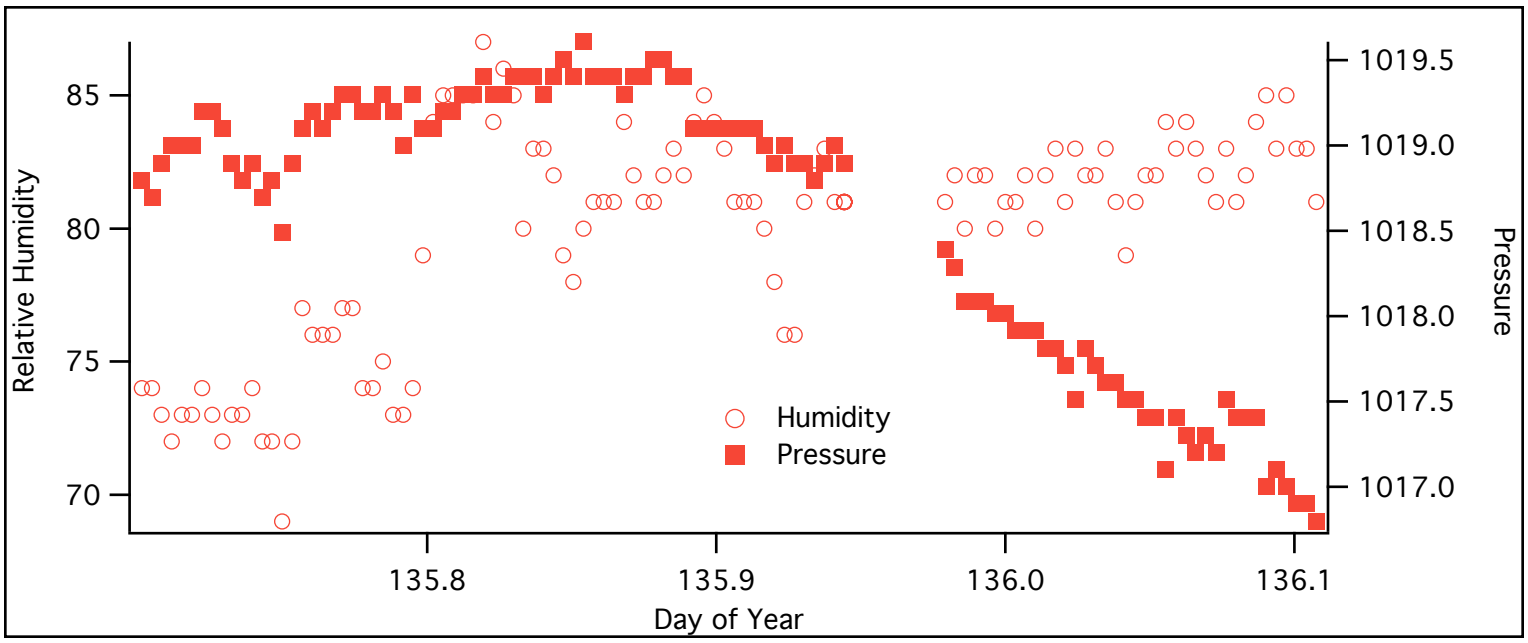
Relative Humidity
85
80
75
70
1019.5
1019.0
1018.5
1018.0
1017.5
1017.0
Pressure
Humidity
Pressure
135.8
135.9
136.0
136.1
Day of Year

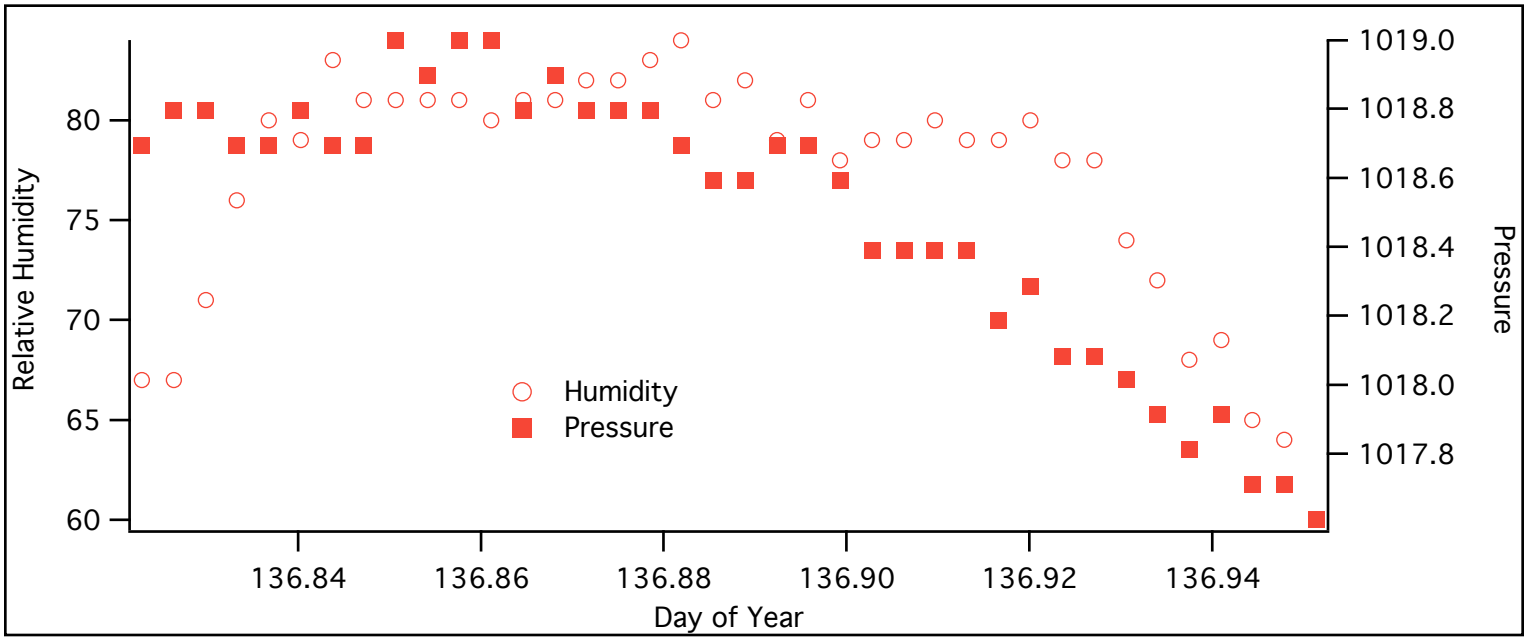
Relative Humidity
80
75
70
65
60
1019.0
1018.8
1018.6
1018.4
1018.2
1018.0
1017.8
Pressure
Humidity
Pressure
136.84
136.86
136.88
136.90
136.92
136.94
Day of Year

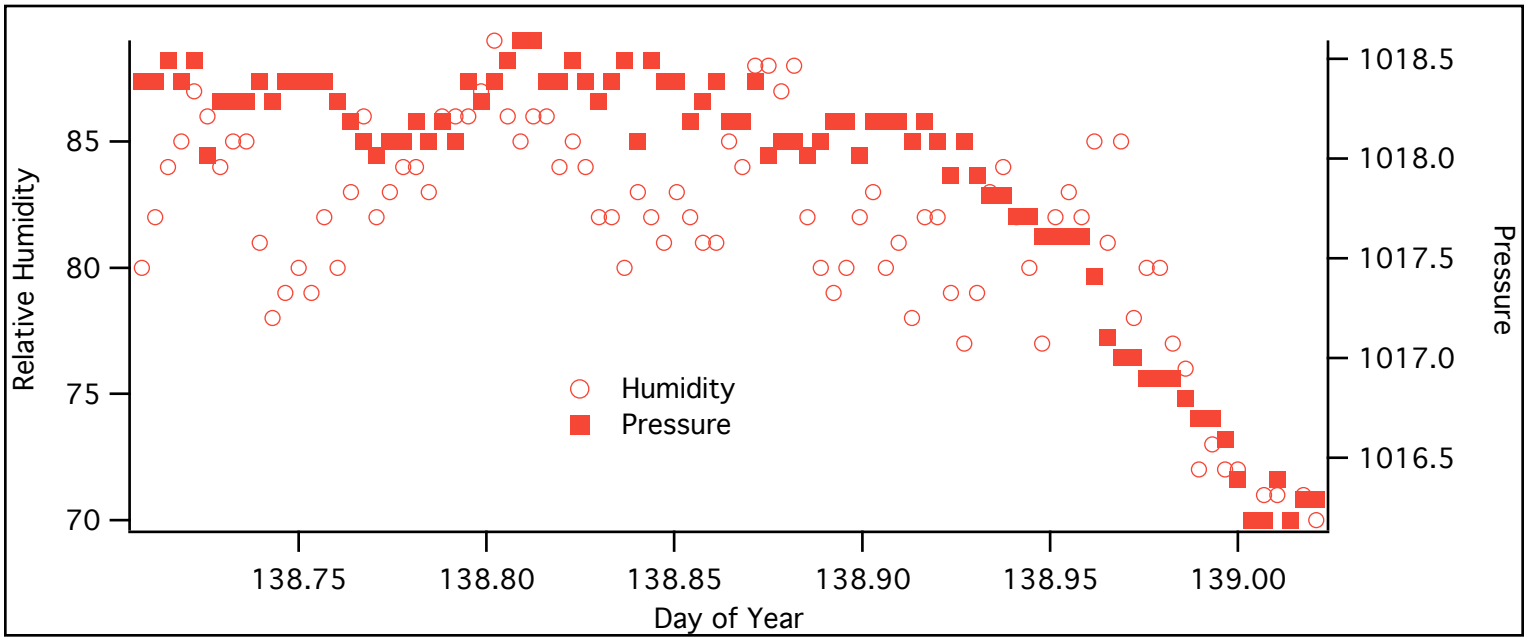
Relative Humidity
85
80
75
70
1018.5
1018.0
1017.5
1017.0
1016.5
Pressure
Humidity
Pressure
138.75
138.80
138.85
138.90
138.95
139.00
Day of Year

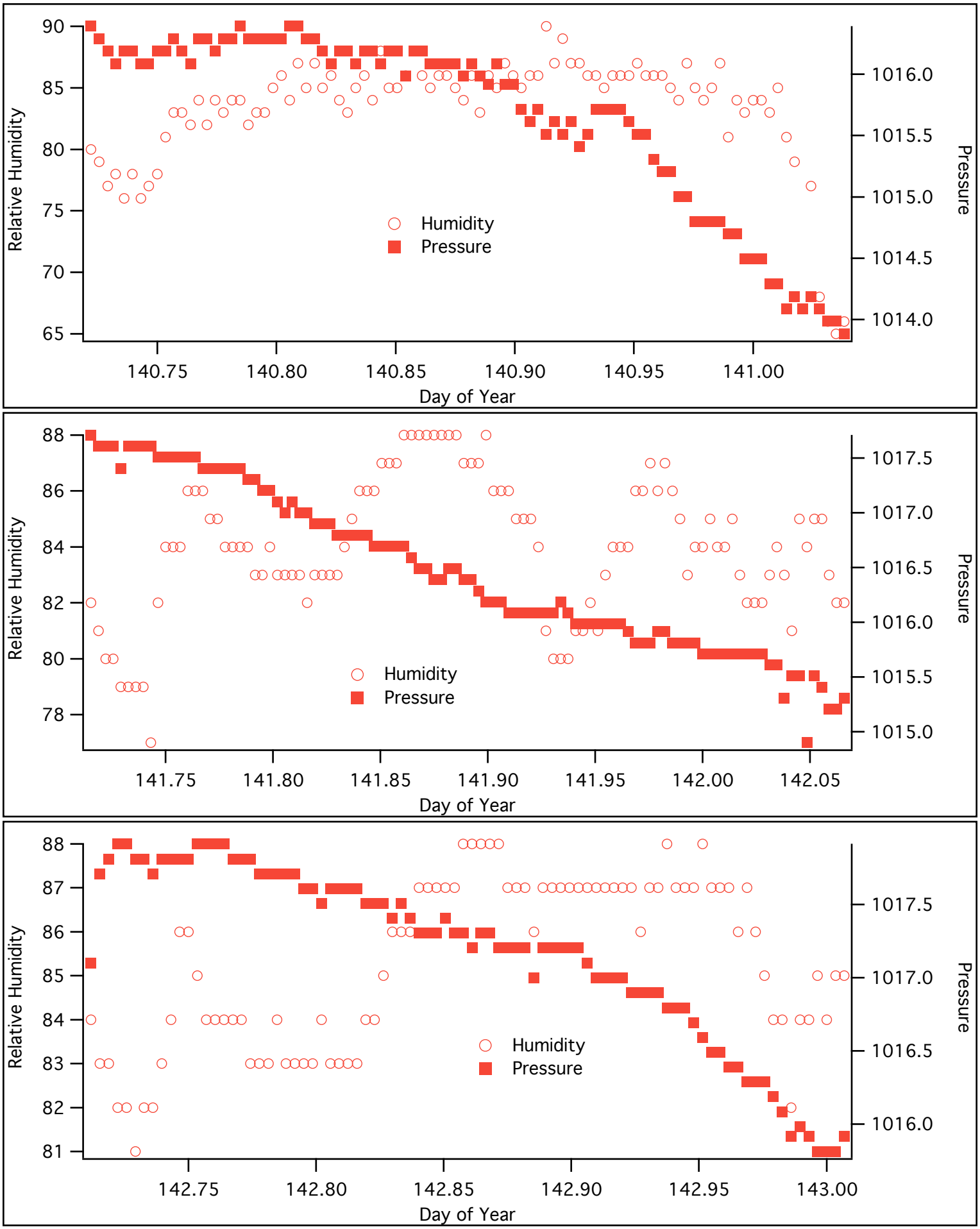
Relative Humidity
Pressure
Humidity
Pressure
Day of Year
90
85
80
75
70
65
1016.0
1015.5
1015.0
1014.5
1014.0
140.75
140.80
140.85
140.90
140.95
141.00
88
86
84
82
80
78
1017.5
1017.0
1016.5
1016.0
1015.5
1015.0
141.75
141.80
141.85
141.90
141.95
142.00
142.05
88
87
86
85
84
83
82
81
1017.5
1017.0
1016.5
1016.0
142.75
142.80
142.85
142.90
142.95
143.00